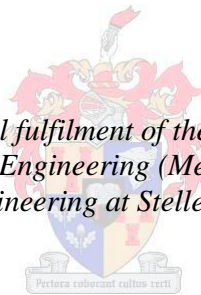


# The use of CFD for Heliostat Wind Load Analysis

by  
Adhikar Vishaykanth Hariram

*Thesis presented in partial fulfilment of the requirements for the degree  
of Master of Engineering (Mechanical) in the  
Faculty of Engineering at Stellenbosch University*



Supervisor: Prof. Thomas M. Harms  
Co-Supervisor: Mr Paul Gauché

March 2015

## Declaration

By submitting this thesis electronically, I declare that the entirety of the work contained therein is my own, original work, that I am the sole author thereof (save to the extent explicitly otherwise stated), that reproduction and publication thereof by Stellenbosch University will not infringe any third party rights and that I have not previously in its entirety or in part submitted it for obtaining any qualification.

Date:.....

## Abstract

The capability of computational fluid dynamics (CFD), in particular the FLUENT™ commercial software suite, to predict wind loadings on heliostats has been investigated. If CFD proves useful in this area then the overall development costs of heliostats and concentrating solar thermal power plants could be reduced. Due to the largest loading on the heliostat originating from wind loads, by using CFD to determine these loads it could be possible to ensure heliostats are not overdesigned. This thesis contains a first study within the Solar Thermal Energy Research Group (STERG) at Stellenbosch University into the use of CFD for determining heliostat wind loads.

The relevant theoretical background concerning the turbulence models used in this study, namely, the RNG k- $\epsilon$ , Realisable k- $\epsilon$  and SST k- $\omega$  turbulence models is reiterated. The ‘standard’ k- $\epsilon$  model and the large eddy simulation (LES) approach, due to their relevance to bluff body flows, are also revisited. Some analysis is also provided around each model to gain insight as to the role of respective modelling sensitivities and their advantages.

Previous work done in the area of heliostat wind studies is reviewed. The geometric considerations when dealing with heliostats leads onto the discussion concerning the requirement of modelling boundary layer profiles. Hence some background is provided on boundary layer modelling techniques. Further insight is drawn from more general previous bluff body CFD reported in the literature, from which observations and recommendations regarding the use of variations of the k- $\epsilon$  turbulence model can be inferred. The simulation procedure from geometry creation to results obtained for the flow over a vertical flat plate is reported. This investigation led to the conclusion that the Realisable k- $\epsilon$  should be used for the heliostat simulations on account of its accurate drag prediction under steady state flow conditions. It was also found that for transient simulations for heliostat like geometries, the SST k- $\omega$  model appears most suitable. The Realisable k- $\epsilon$  model is then used to model the flow about a heliostat using the same procedures as for the flat plate; both with flat and boundary layer inlet profiles.

The overall conclusions drawn from this work are that the Realisable k- $\epsilon$  would not be suitable for predicting wind loads used in the final design of heliostats although it may be used with flat velocity and turbulence profiles to compare differences between early heliostat designs. The conclusion that the Realisable k- $\epsilon$  model should not be used to predict the flow field in the vicinity of a heliostat is also reached.

It is recommended that further work should be carried out by using more advanced modelling techniques, such as the LES, to determine wind loads on heliostats. Furthermore, additional studies focused on accurately reproducing the velocity and turbulence profiles should be done. Lastly a larger set of data containing the orientations mentioned in literature should be generated using the methods contained within this study.

## Opsomming

Die vermoë van Numeriese Vloei Meganika (NVM), spesifiek die van die FLUENT™ kommersiële sagtewarepakket, om die windlaste op heliostate te voorspel was ondersoek. As daar gevind word dat NVM wel betekinsvolle resultate kan lewer, kan dit die totale ontwikkelingskoste van heliostate en gekonsentreerde sonkragstasies verlaag. Wind plaas die grootste las op heliostate, dus deur gebruik te maak van NVM om die windlaste op heliostate te voorspel, kan dit gebruik word om te verseker dat heliostate nie oorontwerp word nie. Hierdie tesis bevat 'n eerste studie binne die Sontermiese Energie Navorsings Groep aan die Universiteit van Stellenbosch, wat die gebruik van NVM om windlaste op heliostate te voorspel ondersoek.

Alle relevante teoretiese agtergrond wat turbulensiemodelle aanbetref, naamlik die RNG  $k-\epsilon$ , Realiseerbare  $k-\epsilon$  en SST  $k-\omega$  turbulensiemodelle, word bespreek. Hulle relevansie tot stompligaamvloei toegestaan, word die „standaard“  $k-\epsilon$  model en die groot werwel simulatie (GWS) benaderings ook bespreek. Elke model word bespreek om die leser insig te gee in dié model se sensitiwiteite en voordele. Vorige studies wat betrekking het tot die studie van heliostate en wind word bespreek. Die geometrie van heliostate lei tot 'n bespreking oor die noodsaaklikheid vir 'n model vir die grenslaagprofiel, dus word grenslaagmodelleringstegnieke bespreek. Verdere insig word verkry van vorige NVM studies uit die literatuur met meer algemene stomp liggame, wat waarnemings en voorstelle vir die gebruik van die  $k-\epsilon$  turbulensiemodel en variante verskaf.

Die simulasiëproses, vanaf geometrieskepping tot die resultate vir die vloei oor 'n vertikale vlak, word bespreek. Hierdie ondersoek het tot die gevolgtrekking gelei dat die realiseerbare  $k-\epsilon$  model gebruik moet word vir die heliostaat simulaties, as gevolg van die akkurate sleurvoorspellings onder bestendigetoestande. Daar was ook gevind dat vir heliostaatagtige liggame onder oorgangskondisies, die SST  $k-\omega$  model mees geskik sal wees. Die Realiseerbare  $k-\epsilon$  model word dan gebruik om die vloei om 'n heliostaat te modelleer deur gebruik te maak van dieselfde proses wat gebruik word om vloei oor 'n plat plaat te analiseer: albei met plat en grenslaaginlaatprofiële.

Die gevolgtrekkings van hierdie studie is dat die Realiseerbare  $k-\epsilon$  model nie gebruik kan word tydens die finale ontwerpfasie om die windlaste op 'n heliostaat te voorspel nie. Dit kan wel gebruik word met plat snelheids- en turbulensieprofiële om die verskille tussen vroeë heliostaatkonsepte te vergelyk. Daar was ook bepaal dat die Realiseerbare  $k-\epsilon$  model nie gebruik moet word om die vloeiveld om 'n heliostaat te voorspel nie. Daar word voorgestel dat verdere studies in hierdie vakgebied met meer gevorderde modelleringstegnieke aangepak word. Dit word aanbeveel dat verdere werk uitgevoer moet word deur die gebruik van meer gevorderde modellering tegnieke, soos GWS, om die wind kragte op heliostats te bepaal. Verder, studies wat akkurate snelheid en turbulensieprofiële produseer sal nog bygelas moet word. Laastens 'n groter stel data

met oriëntasies soos wat in die literatuur beskryf word, moet deur middel van die metodes van dié studie gegeneer word.

## Acknowledgments

I would like to thank Prof. T. Harms for the guidance and encouragement he has provided me throughout the completion of this thesis. I would not have been able to undertake the task of this work without the enthusiastic support of Prof. Harms.

I also like to thank Mr. P. Gauché, my co supervisor and head of the Solar Thermal Energy Research Group (STERG) who helped me learn so many new things about solar thermal energy and understand the need for this research.

To the researchers involved in STERG, I also extend my thanks to you for helping me adapt to a new home in Stellenbosch and exposing me to the world of thermal energy.

For the funding received, without which I would have never received this opportunity, I would like to thank ESKOM.

In conducting and helping with the experimental work in this thesis I would like to thank Miss. D. Bezuidenhout and Mr. D. Roux, without whom there may have not been any experimental results for this work.

Lastly, I would like to thank my parents and close friends who have provided consistent support and encouragement throughout the duration of my studies.

## Table of Contents

Declaration.....	i
Abstract.....	ii
Opsomming.....	iii
Acknowledgments.....	v
List of Figures.....	ix
List of Tables.....	xiii
List of Symbols.....	xiv
1. Introduction.....	1
2. Turbulence Modelling.....	2
2.1 Turbulence modelling background.....	2
2.2 Standard k- $\epsilon$ turbulence model.....	3
2.3 Renormalisation group k- $\epsilon$ turbulence model.....	4
2.4 Realisable k- $\epsilon$ turbulence model.....	6
2.5 Shear stress transport k- $\omega$ turbulence model.....	8
2.6 Large eddy simulation (LES).....	13
2.7 Conclusions.....	14
3. Literature Review.....	15
3.1 Geometry considerations.....	15
3.2 ABL modelling.....	15
3.3 Receiver wind load studies.....	16
3.4 Numerical wind load studies.....	21
3.5 Other bluff body CFD.....	22
3.6 Conclusions.....	26
4. Flat Plate Simulations.....	27
4.1 Simulation geometry.....	27
4.2 Meshing method.....	28

4.3	Simulation settings .....	30
4.3.1	General settings.....	30
4.3.2	Models and wall treatment.....	32
4.3.3	Boundary conditions .....	32
4.3.4	Reference values .....	33
4.3.5	Solution methods .....	33
4.3.6	Solution monitoring .....	34
4.3.7	Initialisation .....	34
4.4	Simulation and literature results comparison .....	34
4.4.1	Mesh independence.....	35
4.4.2	Drag coefficients.....	36
4.4.3	Velocity fluctuations.....	37
4.4.4	Qualitative results .....	39
4.5	Model selection .....	42
4.6	Conclusion.....	43
5.	Heliostat Simulations .....	44
5.1	Simulation and literature geometries.....	44
5.2	Meshing methods .....	46
5.3	Simulation settings .....	51
5.4	CFD and literature results comparison.....	52
5.4.1	Flat inlet profile.....	53
5.4.2	Boundary layer inlet profile .....	56
5.5	Discussion and conclusion .....	59
6.	Particle Image Velocimetry (PIV) .....	60
6.1	Simulation conditions.....	60
6.2	Brief PIV description .....	62
6.3	Experimental setup and procedure .....	63

6.4	Experimental and simulation results .....	65
6.4.1	Velocity profiles.....	65
6.4.2	Streamlines.....	67
6.5	Discussion and conclusion .....	68
7.	Summary and Conclusions .....	78
8.	Possible Future Work.....	80
	References.....	81
	Appendix A: Domain Width and Height .....	84
	Appendix B: Iso-surfaces at Different Time Steps .....	89
	Appendix C: Mesh Independency Study for Heliostats.....	92
	Appendix D: PIV Safety Report .....	93
	Appendix E: Photographs of Experimental Setup .....	98
	Appendix F: Dimensioned Geometry .....	101
	Appendix G: Details of Velocity Profile Locations.....	104

## List of Figures

Figure 1-1: Schematic of parabolic trough system (left) and central receiver system (right) (Environment, 2010).....	1
Figure 3-1: Geometric description of load coefficients (Cermak and Peterka, 1979).....	17
Figure 3-2: Geometry used in vortex shedding study (Matty, 1979).....	19
Figure 3-3: Chord to height above ground ratio (Matty, 1979).....	19
Figure 3-4: Strain rate tensor distribution (Murakami, Comparison of various turbulence models applied to a bluff body, 1993).....	23
Figure 4-1: Flat plate geometry with 1/4 gap to chord ratio (left) and ground mounted (right).....	27
Figure 4-2: Flat plate within domain geometry side view (top) and front view (bottom).....	28
Figure 4-3: Cell types: hexahedral (left) and tetrahedral (right).....	29
Figure 4-4: Cell type: prism.....	29
Figure 4-5: Transition from small to large cells using prism cells.....	30
Figure 4-6: Coarse (top) and fine (bottom) meshes generated.....	31
Figure 4-7: Inlet named selection.....	31
Figure 4-8: Finest mesh used in simulation with detailed view (bottom).....	35
Figure 4-9: Comparison of Q-criterion level 0.0025 for Realisable (top left), SST (bottom left) and RNG (right) models for a ground mounted flat plate, coloured by velocity magnitude.....	39
Figure 4-10: Streamlines in the wake of a ground mounted flat plate for the Realisable (top left), SST (bottom left) and RNG (right) models from the bottom view.....	41

Figure 4-11: Comparison of Q-criterion level 0.0025 for Realisable (top left), SST (bottom left) and RNG (right) models for a flat plate with a ground gap, coloured by velocity magnitude .....	42
Figure 5-1: Geometry used in simulation (left) compared to model geometry (right), (Cermak and Peterka, 1979).....	44
Figure 5-2: Detail of two-dimensional stair-step mesh.....	45
Figure 5-3: Perpendicular (left) and 45° tilted (right) orientations used in simulations .....	45
Figure 5-4: Location of heliostat within domain .....	46
Figure 5-5: Coarse (top), fine (middle) and finest (bottom) meshes generated.....	47
Figure 5-6: Split domain to allow different meshing procedures .....	48
Figure 5-7: Coarse (top), medium (second from top), fine (second from bottom), finest (bottom) meshes generated .....	49
Figure 5-8: Polyhedral mesh example (Symscape, 2013) .....	50
Figure 5-9: Converted polyhedral mesh .....	50
Figure 5-10: Application of matching type interface (FLUENT™, 2013).....	52
Figure 5-11: Comparison of flat velocity and turbulence profiles.....	55
Figure 5-12: Comparison of boundary layer velocity and turbulence profiles .....	57
Figure 6-1: Wind tunnel (left) and simulation (right) geometry .....	60
Figure 6-2: Side view (top) and front view (bottom) of heliostat within domain.....	61
Figure 6-3: Finest mesh for perpendicular (top) and tilted (bottom) heliostats .....	62
Figure 6-4: Schematic of PIV process (AIM², 2014).....	63
Figure 6-5: Known problems with PIV photograph capture (shading and glare).....	64
Figure 6-6: PIV calibration plate example (National Instruments, 2013) .....	65

Figure 6-7: Example of good (black line) and bad (enclosed) sampling areas.....66

Figure 6-8: Perpendicular heliostat streamwise ( $u$ ) velocity profiles in offset plane.....70

Figure 6-9: Perpendicular heliostat vertical ( $v$ ) velocity profiles in offset plane .....71

Figure 6-10: Tilted heliostat streamwise ( $u$ ) velocity profiles in mid vertical plane .....72

Figure 6-11: Tilted heliostat vertical ( $v$ ) velocity profiles in mid vertical plane .....73

Figure 6-12: Tilted heliostat streamwise ( $u$ ) velocity profiles in offset vertical plane .....74

Figure 6-13: Tilted heliostat vertical ( $v$ ) velocity profiles in offset vertical plane.....75

Figure 6-14: Streamlines for perpendicular heliostat in offset plane for simulation  
(top) and PIV (bottom).....76

Figure 6-15: Streamlines for tilted heliostat in mid plane simulation (top) and PIV  
(bottom).....76

Figure 6-16: Streamlines for tilted heliostat in offset plane simulation (top) and PIV  
(bottom).....77

Figure A-1: Streamlines for flat plate simulation in vertical (top) and horizontal  
(bottom) planes .....84

Figure A-2: Picture of heliostat from Cermak and Peterka (1979) within wind tunnel .....85

Figure A-3: Streamlines for perpendicularly orientated heliostat in vertical (top) and  
horizontal (bottom) planes .....86

Figure A-4: Streamlines for tilted heliostat in vertical (top) and horizontal (bottom)  
planes .....87

Figure A-5: Pressure contour along the side, top and rear domain walls perpendicular  
heliostat .....88

Figure A-6: Pressure contour along the side, top and rear domain walls tilted  
heliostat .....88

Figure B-1: Iso-surface of q-criterion for various time steps with the RNG k- $\epsilon$ model .....	90
Figure B-2: Iso-surface of q-criterion for various time steps with the SST k- $\omega$ model.....	91
Figure C-1: Sketch of test orientation .....	94
Figure E-1: Location of components for horizontal plane testing for Bezuidenhout (2014).....	98
Figure E-2: Location of components for vertical plane used in thesis .....	99
Figure E-3: Picture of tilted heliostat within wind tunnel.....	100
Figure G-1: Reference points for perpendicular heliostat in offset plane.....	104
Figure G-2: Reference points for tilted heliostat in mid and offset plane .....	105

## List of Tables

Table 4-1: Drag coefficients .....	37
Table 4-2: Simulated and experimental velocity fluctuation frequencies .....	37
Table 5-1: Load coefficients for flat inlet profiles .....	56
Table 5-2: Load coefficients for boundary layer profiles .....	58
Table C-1: Cell count and load coefficient for different mesh densities .....	92
Table D-1: Personnel risks .....	94
Table D-2: Equipment risks .....	95
Table G-1: Location of lines relative to heliostat .....	105

## List of Symbols

$a$	Speed of sound
$A_0$	Model constant (4.04)
$A_{ref}$	Reference area of heliostat
$A_s$	Mean strain rate dependant term
$a_s$	Swirl constant (0.07)
$C_1$	Source term variable
$C_{1\varepsilon}$	Model constant (model dependant)
$C_2$	Model constant (1.9)
$C_{2\varepsilon}$	Model constant (model dependant)
$C_{3\varepsilon}$	Model constant (value not irrelevant to study, also model dependant)
$C_{M(i)}$	Moment coefficient about the x or y axis at the base of the heliostat
$C_{M(y)}$	Moment coefficient about y axis
$C_{M(z)}$	Moment coefficient about the z axis
$C_{MH(i)}$	Hinge moment coefficient about the x or y axis
$C_{f(i)}$	Force coefficient in the (i) direction
$C_v$	Model constant ( $\simeq 100$ )
$C_\mu$	Model constant (model dependant)
$D_\omega$	$\omega$ cross diffusion term
$D_\omega^+$	Positive part of cross diffusion term
$F_{(i)}$	Force in the (i) direction
$F_1$	Blending function 1
$F_2$	Blending function 2
$G_b$	TKE generation due to buoyancy

$G_k$	TKE generation due to mean velocity gradients
$G_\omega$	Generation of $\omega$
$g_h$	Function of ratio of chord length to height above ground
$\tilde{G}_k$	TKE production term in k- $\omega$ class of model
$H$	Chord length of heliostat
$HCL$	Height of hinge
$h$	Height above ground plane
$I$	Turbulence intensity
$k$	Turbulence kinetic energy (TKE)
$L$	Chord length of flat plate
$L_{ref}$	Reference length of heliostat
$L_t$	Turbulence length scale
$M_{(i)}$	Moment about the x or y axis at the base of the heliostat
$M_{(z)}$	Moment about the z axis
$M_{t_0}$	Constant reference value for $M_t$ (0.25)
$M_{H(i)}$	Hinge moment about the x or y axis
$M_t$	Variable related to speed of sound and compressibility effects on $\omega$
$P$	Pressure
$R$	Gas constant
$Re$	Reynolds number
$R_k$	Constant related to turbulence viscosity (6) (Critical ratio related to turbulence viscosity)
$R_\beta$	Constant related to $\beta^*$ and $\beta_i^*$ (8) (Critical ratio relating to $\beta^*$ and $\beta_i^*$ )
$R_\varepsilon$	Additional term in $\varepsilon$ equation for the RNG model

$R_\omega$	Variable related to generation of $\omega$ (Critical ratio related to generation of $\omega$ )
$Re_t$	Scaled ratio of $k$ to $\omega$ related to turbulence viscosity
$\vec{r}$	Displacement vector
$S$	Modulus of mean strain-rate tensor
$St$	Strouhal number
$S_\infty$	Function of $Re$
$S_{ij}$	Strain rate tensor
$S_k$	TKE source term
$S_\varepsilon$	TKE dissipation rate source term
$S_\omega$	$\omega$ source term
$\tilde{S}$	Mean strain rate dependant term
$T$	Absolute temperature
$t$	Time
$t'$	Dummy time step variable
$U$	Fluid velocity
$U^*$	Rotation dependant term
$u_*$	Friction velocity
$u_i$	Velocity tensor
$\bar{u}$	Time-averaged velocity component
$u'$	Fluctuating velocity component
$W$	Mean strain rate dependant term
$x$	Spatial variable
$x_i$	Direction tensor
$x'$	Dummy spatial variable

$y$	Distance to next surface
$Y_M$	Effect of compressibility on TKE in k- $\epsilon$ class of model
$Y_k$	Effect of compressibility on TKE in k- $\omega$ class of model
$Y_\omega$	Effect of compressibility on $\omega$
$z_0$	Surface roughness length
$\alpha$	Under-relaxation factor
$\alpha^*$	Variable related to turbulence viscosity
$\alpha_0$	Model constant (1.0)
$\alpha_0^*$	Constant related to turbulence viscosity (0.024)
$\alpha_1$	Constant related to turbulence viscosity (0.31)
$\alpha_{\infty,1}$	Variable related to $\alpha_\infty$ formulation
$\alpha_{\infty,2}$	Variable related to $\alpha_\infty$ formulation
$\alpha_\infty$	Variable related to generation of $\omega$
$\alpha_\infty^*$	Constant related to turbulence viscosity (1.0)
$\alpha_k$	Turbulent Prandtl number
$\alpha_\epsilon$	Turbulent Prandtl number
$\beta$	Model constant (0.012)
$\beta^*$	Variable related to generation of $\omega$ and compressibility effects on TKE
$\beta_\infty^*$	Constant related to $\beta^*$ and $\beta_i^*$ (0.09)
$\beta_i^*$	Variable related to compressibility effects on $\omega$ , same numerical value as $\beta^*$
$\beta_{i,1}$	Variable related to $\alpha_{\infty,1}$ and $\beta_i$ formulation
$\beta_{i,2}$	Variable related to $\alpha_{\infty,2}$ and $\beta_i$ formulation
$\beta_i$	Constant related to turbulent viscosity and compressibility effects (0.072)

$\gamma$	Ratio of specific heats
$\Gamma_k$	TKE diffusivity
$\Gamma_\omega$	$\omega$ diffusivity
$\Delta$	Grid step size
$\Delta\phi$	Change in variable $\phi$
$\delta_{ij}$	Kronecker delta
$\varepsilon$	Turbulence kinetic energy dissipation rate
$\zeta^*$	Constant related to $\beta$ (0.25)
$\eta$	Term dependant on strain, TKE and $\varepsilon$ for the RNG model
$\eta_0$	Model constant (4.38)
$\kappa$	Von Karman's constant ( $\simeq 0.4$ )
$\mu$	Dynamic viscosity
$\mu_{eff}$	Effective turbulence viscosity
$\mu_{mol}$	Molecular viscosity
$\mu_t$	Turbulent dynamic viscosity
$\mu_{t0}$	Turbulence viscosity calculated without swirl modification
$\nu$	Kinematic viscosity
$\hat{\nu}$	Ratio of effective viscosity to dynamic viscosity
$\nu_t$	Turbulent kinematic viscosity
$\xi$	Any variable
$\rho$	Fluid density
$\sigma_{(k,\omega),1}$	Model constants related to turbulent Prandtl numbers for k and $\omega$
$\sigma_{(k,\omega),2}$	Model constants related to turbulent Prandtl numbers for k and $\omega$
$\sigma_{(k,\omega)}$	Turbulent Prandtl numbers for TKE and $\omega$

$\sigma_k$	Model constant (model dependant)
$\sigma_\varepsilon$	Model constant (model dependant)
$\Phi_1$	Blending function 1 criterion
$\Phi_2$	Blending function 2 criterion
$\phi$	Mean strain rate dependant term
$\phi'$	Any unfiltered and modelled variable
$\phi_{f,SOU}$	A value on the face of a cell of a variable calculated using second order upwind differencing
$\phi_{old}$	Value of variable at precious iteration
$\phi_{u,c}$	A value of a variable at an upwind cell centre
$\tilde{\phi}$	Any filtered variable
$\Omega$	Characteristic swirl number
$\Omega_{ij}$	Rate of rotation tensor
$\tilde{\Omega}_{ij}$	rotation rate dependant term
$\overline{\Omega}_{ij}$	Mean rotation rate
$\omega$	TKE specific dissipation rate
$\omega_k$	Angular velocity
$\nabla$	The mathematical operator del representing the gradient of some function

## 1. Introduction

In South Africa currently, the largest source of electricity comes from the burning of coal to produce power. This source of energy is, however, bound to be depleted in the foreseeable future. Pressures on the power industry may also increase as concerns over CO<sub>2</sub> emissions begin to increase and as such, renewable energy provides an attractive alternative in the future. Amongst the sources of renewable energies, the following well known types are included: photovoltaic technologies, wind power and concentrated solar power (CSP). From these, CSP is the most attractive moving forwards due in large to its ability to incorporate thermal storage into the power plant, thus allowing for possible 24 hour operation.

Amongst CSP, the two most popular types of plant are the central receiver type system and the parabolic trough system. Within parabolic trough type power plants, the Sun's rays are concentrated onto receiver tubes via parabolic mirrors out in the collector field. Within a central receiver type plant, the Sun's energy is concentrated onto a central receiver via a large field of heliostats. A general schematic of these two types of plan can be seen in Figure 1-1.

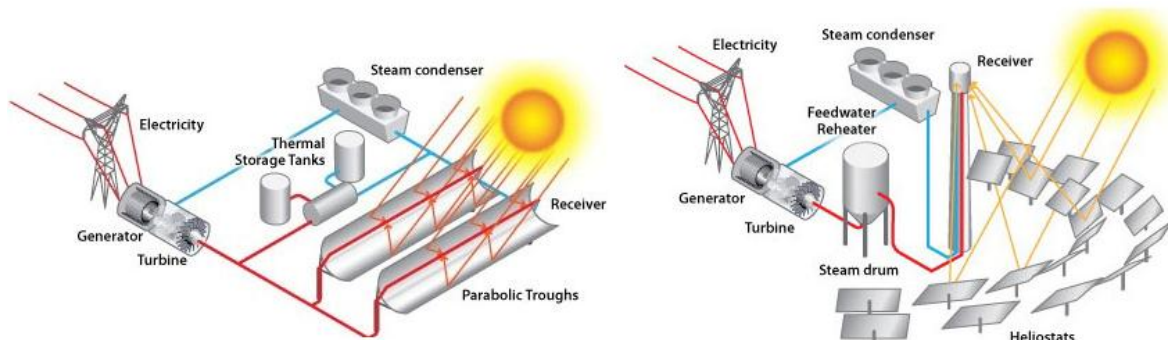


Figure 1-1: Schematic of parabolic trough system (left) and central receiver system (right)  
(Environment, 2010)

Within the central receiver plant, up to 40 % of the plant's cost is made up from the heliostat field (IRENA, 2012). This makes the design of these heliostats a fundamental factor in cost savings of the plant. Thus, by investigating the wind loading on such heliostats, their design can be optimised to be strong yet affordable. The investigation of these wind loadings has been undertaken using computational fluid dynamics (CFD) using the software package FLUENT™ version 14.5, released in 2013 on a system containing an Intel core-i7 3970X 6 core processor with 64 GB of RAM.

The investigation undertaken first evaluates various turbulence models on their performance for the flow around a vertical flat plate as such geometry is highly similar to that of a heliostat. From their onwards the most suitable turbulence model can be chosen for heliostat simulations. Experimental work has also been conducted in order to determine how well CFD can predict the flow field in the vicinity of a heliostat. The main objectives of this study were to determine the performance of certain two equation RANS turbulence models for the modelling of heliostat wind loads.

## 2. Turbulence Modelling

It should be noted that most of the information contained within this chapter is obtained from FLUENT™ (2013) unless otherwise specifically referenced. This is done in order to provide a basic analysis of the turbulence models that are used within, and are relevant to, this thesis. Equations are also primarily obtained from FLUENT™ (2013) in order to gain some insight into what may be occurring within the FLUENT™ solver during the solution process as the CFD software used in this thesis is FLUENT™. The original formation of some of the models analysed here can be found in other literature, such as the RNG k-ε model which was founded by Yakhot *et al.*, (1992). Such a formulation may, however, not be used in its original form within FLUENT™ and hence exploration of the FLUENT™ (2013) literature is appropriate. The purpose of this chapter is to provide some insight into selected turbulence models used in this thesis as well as cited in other CFD studies.

### 2.1 Turbulence modelling background

The basis of all turbulence models used in this thesis is the Reynolds-averaged-Navier-Stokes (RANS) equations which essentially describe all fluid motion. These equations are derived by recognising that a turbulent velocity can be broken into a time-averaged and fluctuating component:

$$u = \bar{u} + u' \quad (2-1)$$

Substituting this into the Navier-Stokes equations results in the averaged continuity equation:

$$\frac{\partial \rho}{\partial t} + \frac{\partial}{\partial x_i} (\rho u_i) = 0 \quad (2-2)$$

and momentum transport equation:

$$\begin{aligned} \frac{\partial}{\partial t} (\rho u_i) + \frac{\partial}{\partial x_j} (\rho u_i u_j) \\ = -\frac{\partial P}{\partial x_i} + \frac{\partial}{\partial x_j} \left[ \mu \left( \frac{\partial u_i}{\partial x_j} + \frac{\partial u_j}{\partial x_i} \right) - \frac{2}{3} \delta_{ij} \frac{\partial u_l}{\partial x_l} \right] + \frac{\partial}{\partial x_j} (-\rho \overline{u'_i u'_j}) \end{aligned} \quad (2-3)$$

where each quantity for velocity is the time-averaged value and the over bar has been dropped for convenience. When the Navier-Stokes equations are time-averaged, giving the RANS equations, an additional term is introduced,  $-\rho \overline{u'_i u'_j}$ , which is known as the Reynolds stress tensor (Re stress). The introduction of this term to the RANS equations leads to the closure problem which refers to the manner in which the Reynolds stresses are resolved. A common approach to closing the RANS equations is the Boussinesq hypothesis which models the Reynolds stresses by means of a turbulence viscosity,  $\mu_t$ , related to mean velocity gradients. This is given as:

$$-\overline{\rho u'_i u'_j} = \mu_t \left( \frac{\partial u_i}{\partial x_j} + \frac{\partial u_j}{\partial x_i} \right) - \frac{2}{3} \left( \rho k + \mu_t \frac{\partial u_k}{\partial x_k} \right) \delta_{ij} \quad (2-4)$$

and is used in the Spalart-Allmaras, k- $\epsilon$  and k- $\omega$  class of models. A key factor in turbulence modelling is the formulation of the turbulent viscosity  $\mu_t$  which varies between turbulence models. The models pertinent to this thesis are the renormalisation group k- $\epsilon$  (RNG k- $\epsilon$ ), Realisable k- $\epsilon$  and shear stress transport k- $\omega$  (SST k- $\omega$ ) models, hence only their formulations will be presented here.

Common to all three models is the transport of turbulence kinetic energy (TKE), which is the 'k' in each model. The transport of TKE is derived directly from the RANS equations by multiplying through by the averaged velocity  $u_i$  and using the definition:

$$k = \frac{1}{2} \overline{(u'_i u'_i)} \quad (2-5)$$

## 2.2 Standard k- $\epsilon$ turbulence model

For completeness, the standard k- $\epsilon$  turbulence model equations will be presented as this forms the basis for the equations presented further on. The transport equations for the k- $\epsilon$  turbulence model are, starting with TKE:

$$\frac{\partial}{\partial t}(\rho k) + \frac{\partial}{\partial x_i}(\rho k u_i) = \frac{\partial}{\partial x_j} \left[ \left( \mu + \frac{\mu_t}{\sigma_k} \right) \frac{\partial k}{\partial x_j} \right] + G_k + G_b - \rho \epsilon - Y_M + S_k \quad (2-6)$$

Note that the terms  $G_b$  and  $Y_M$  are the production, and contribution, due to buoyancy and compressibility respectively. Due to the irrelevance of these effects to the current study these effects will not be described. Going from left to right the terms in the equation, excluding buoyancy and compressibility terms, each represent: the rate of change of, the transport by convection, the diffusivity, the rate of production, the rate of destruction and finally a source term, all for TKE. Now the TKE dissipation equation:

$$\frac{\partial}{\partial t}(\rho \epsilon) + \frac{\partial}{\partial x_i}(\rho \epsilon u_i) = \frac{\partial}{\partial x_j} \left[ \left( \mu + \frac{\mu_t}{\sigma_\epsilon} \right) \frac{\partial \epsilon}{\partial x_j} \right] + C_{1\epsilon} \frac{\epsilon}{k} (G_k + C_{3\epsilon} G_b) - C_{2\epsilon} \rho \frac{\epsilon^2}{k} + S_\epsilon \quad (2-7)$$

which is similar in form to the equation for TKE and also has the terms from left to right representing the same processes except for TKE dissipation rate. Note that within these equations the term  $G_k$  is common to both the RNG k- $\epsilon$  and Realisable k- $\epsilon$ , and is described by:

$$G_k = 2\mu_t S_{ij} S_{ij} \quad (2-8)$$

where  $S_{ij}$  is the mean strain rate tensor defined by:

$$S_{ij} = \frac{1}{2} \left( \frac{\partial u_i}{\partial x_j} + \frac{\partial u_j}{\partial x_i} \right) \quad (2-9)$$

Finally, the description of the k- $\varepsilon$  turbulence model is complete with the description of the formulation of  $\mu_t$  and the equation constants which are given by:

$$\mu_t = \rho C_\mu \frac{k^2}{\varepsilon} \quad (2-10)$$

with constants:

$$C_{1\varepsilon} = 1.44, C_{2\varepsilon} = 1.92, C_\mu = 0.09, \sigma_k = 1.0, \sigma_\varepsilon = 1.3 \quad (2-11)$$

### 2.3 Renormalisation group k- $\varepsilon$ turbulence model

Following the description of the k- $\varepsilon$  model, a description of the RNG k- $\varepsilon$  is provided as it is pertinent to the study conducted. The RNG k- $\varepsilon$  model is derived by having a cut off wavenumber in the turbulence energy spectrum, outside of which the effects of turbulence are approximated by random forces. In order to account for smaller scales of turbulence, a modified turbulence viscosity has been formulated, the equations of which will follow later in this section. This new viscosity also allows the model to operate in low Re regions, meaning that the equations can be integrated right down to the wall. Additionally to the formulation of a modified turbulence viscosity, this model has an additional term in the TKE dissipation equation which results in greater accuracy for rapidly strained flows as well as the inclusion of a swirl modification to the turbulence viscosity allowing for the effects of swirl on turbulence to be accounted for. The formulation of this model also results in different constants to the standard k- $\varepsilon$  model.

The transport equations for TKE and TKE dissipation, referred to as dissipation henceforth for brevity, in the RNG k- $\varepsilon$  model are given as follows:

TKE:

$$\frac{\partial}{\partial t}(\rho k) + \frac{\partial}{\partial x_i}(\rho k u_i) = \frac{\partial}{\partial x_j} \left( \alpha_k \mu_{eff} \frac{\partial k}{\partial x_j} \right) + G_k + G_b - \rho \varepsilon - Y_M + S_k \quad (2-12)$$

and dissipation:

$$\begin{aligned} \frac{\partial}{\partial t}(\rho \varepsilon) + \frac{\partial}{\partial x_i}(\rho \varepsilon u_i) \\ = \frac{\partial}{\partial x_j} \left( \alpha_\varepsilon \mu_{eff} \frac{\partial \varepsilon}{\partial x_j} \right) + C_{1\varepsilon} \frac{\varepsilon}{k} (G_k + C_{3\varepsilon} G_b) - C_{2\varepsilon} \rho \frac{\varepsilon^2}{k} - R_\varepsilon + S_\varepsilon \end{aligned} \quad (2-13)$$

It can be seen that the additional term in the dissipation equations is  $R_\varepsilon$  which is given by:

$$R_\varepsilon = \frac{C_\mu \rho \eta^3 (1 - \eta/\eta_0) \varepsilon^2}{1 + \beta \eta^3} \frac{\varepsilon^2}{k} \quad (2-14)$$

where:

$$\eta \equiv \frac{Sk}{\varepsilon} \quad (2-15)$$

and:

$$\eta_0 = 4.38 \text{ and } \beta = 0.012 \quad (2-16)$$

where  $S$  is the modulus of the mean strain-rate tensor, that is:

$$S \equiv \sqrt{2S_{ij}S_{ij}} \quad (2-17)$$

By looking at the formulation of the  $R_\varepsilon$  term, it can be seen that in regions of high strain, the value of  $\eta$  will increase and for values of  $\eta$  greater than  $\eta_0$ , the contribution of  $R_\varepsilon$  becomes negative. This helps combat the issue of overproduction of turbulence (which is a known issue with the standard k- $\varepsilon$  model) in rapidly strained flows by increasing the dissipation in rapidly strained areas.

Now, as mentioned, the cut off wavenumber results in a modified turbulence viscosity having to be formulated to account for the cut off scales of turbulence. This formulation is given by:

$$d\left(\frac{\rho^2 k}{\sqrt{\varepsilon\mu}}\right) = 1.72 \frac{\hat{v}}{\sqrt{\hat{v}^3 - 1 + C_v}} d\hat{v} \quad (2-18)$$

where:

$$\hat{v} = \frac{\mu_{eff}}{\mu} \quad (2-19)$$

and

$$C_v \approx 100 \quad (2-20)$$

With this formulation of turbulent viscosity, a notable feature is that in the high Re limit,  $\mu_t$  is calculated in the same way as for the standard k- $\varepsilon$ , however, with the changed constant for  $C_\mu$  being 0.0845 for the RNG k- $\varepsilon$ . This value had been derived using RNG theory as opposed to being tuned as with the original value of 0.09.

In addition, for highly swirling flows,  $\mu_t$  is also altered according to:

$$\mu_t = \mu_{t0} f\left(a_s, \Omega, \frac{k}{\varepsilon}\right) \quad (2-21)$$

in which  $\mu_{t0}$  is the turbulence viscosity calculated before any modification and  $a_s$  is a swirl constant which takes on a value of 0.07 for mildly swirling flows and can be assigned a higher value for stronger swirling flows. The third variable,  $\Omega$ , is a characteristic swirl number specific to ANSYS FLUENT™. Details of the function itself are, unfortunately, not given within FLUENT™ (2013) to protect intellectual property. It is possible though that

this function performs a similar function to the curvature modification for  $C_\mu$  shown in Yin *et al.*, (1996).

The last component of the RNG k- $\varepsilon$  model, apart from the constants, is the inverse turbulent Prandtl numbers,  $\alpha_k$  and  $\alpha_\varepsilon$ . These are solved for using the following formula, derived from RNG theory:

$$\left| \frac{\alpha - 1.3929}{\alpha_0 - 1.3929} \right|^{0.6321} \left| \frac{\alpha - 2.3929}{\alpha_0 - 2.3929} \right|^{0.3679} = \frac{\mu_{mol}}{\mu_{eff}} \quad (2-22)$$

with:

$$\alpha_0 = 1.0 \quad (2-23)$$

and in the high Re limit, they take on a value of approximately 1.393 which is fairly similar to the inverse turbulent Prandtl numbers from the standard k- $\varepsilon$  model. To complete this model, the last two constants are given as:

$$C_{1\varepsilon} = 1.42, C_{2\varepsilon} = 1.68 \quad (2-24)$$

which are also fairly similar to their equivalents in the standard k- $\varepsilon$  model.

## 2.4 Realisable k- $\varepsilon$ turbulence model

The Realisable k- $\varepsilon$  model is the next model which will be described due to its usage in this thesis. This model has a variable  $C_\mu$  which is based on mean strain and rotation rates. It also has a reformulated equation for dissipation based on the exact transport equation for mean square of the vorticity fluctuation. Lastly, one of the important factors about this model is the fact that it is ‘realisable’, which implies that the mathematics of the equations more closely satisfies the physics of the flow in that the normal Re stress is always positive. This is important as neither the standard nor the RNG k- $\varepsilon$  models are realisable.

A clearer understanding of what makes the model realisable can be obtained by investigating the normal Re stress in a strained flow, formulated by using the Boussinesq hypothesis and applying the definition of turbulence viscosity within the k- $\varepsilon$  class of models. This process results in a normal Re stress being given as:

$$\overline{u'^2} = \frac{2}{3} k - 2\nu_t \frac{\partial u}{\partial x} \quad (2-25)$$

where:

$$\nu_t = \frac{\mu_t}{\rho} = C_\mu \frac{k^2}{\varepsilon} \quad (2-26)$$

Now considering the normal Re stress  $\overline{u'^2}$ ,  $\overline{v'^2}$  and  $\overline{w'^2}$  (which are assumed to be isotropic) is a square quantity, it should always be positive, however, by equation (2-25) it can be seen that  $\overline{u'^2}$  can go negative when:

$$\frac{k}{\varepsilon} \frac{\partial u}{\partial x} > \frac{1}{3C_\mu} \quad (2-27)$$

In order to overcome this problem, the formulation of  $C_\mu$  was made variable and dependent on the mean strain rates and rotation rates in order to ensure the realisability of the model. The definition of  $C_\mu$  will be given further on with the set of equations describing the Realisable k- $\varepsilon$  model, starting with the transport equations for TKE:

$$\frac{\partial}{\partial t}(\rho k) + \frac{\partial}{\partial x_j}(\rho k u_j) = \frac{\partial}{\partial x_j} \left[ \left( \mu + \frac{\mu_t}{\sigma_k} \right) \frac{\partial k}{\partial x_j} \right] + G_k - \rho \varepsilon + S_k + G_b - Y_M \quad (2-28)$$

and dissipation:

$$\begin{aligned} \frac{\partial}{\partial t}(\rho \varepsilon) + \frac{\partial}{\partial x_i}(\rho \varepsilon u_i) \\ = \frac{\partial}{\partial x_j} \left[ \left( \mu + \frac{\mu_t}{\sigma_\varepsilon} \right) \frac{\partial \varepsilon}{\partial x_j} \right] + \rho C_1 S_\varepsilon - \rho C_2 \frac{\varepsilon^2}{k + \sqrt{\nu \varepsilon}} + S_\varepsilon + C_{1\varepsilon} \frac{\varepsilon}{k} C_{3\varepsilon} G_b \end{aligned} \quad (2-29)$$

where, the terms on the right hand side of the equations are, in order: the diffusivity, the production term, destruction term and a source term. Other terms after these three are not of concern as they are the production terms due to buoyancy and, in the  $k$  equation, the compressibility effects. Noticeable with the presented transport equations is that the  $k$  equation is the same as the previous models, however, the  $\varepsilon$  equation is quite different. This is seen in the production term, which does not contain  $k$  and in the destruction term which does not have a singularity. The exclusion of the  $k$  term is believed to better represent the spectral energy transfer, which is, the transfer of energy between the various eddy wavelengths and frequencies. In the production term for  $\varepsilon$ ,  $C_1$  is given by:

$$C_1 = \max \left[ 0.43, \frac{\eta}{\eta + 5} \right] \quad (2-30)$$

where the definition of  $\eta$  is the same as for the RNG k- $\varepsilon$  model.

Now, as discussed earlier, the formulation of the turbulence viscosity is the most prominent difference between the Realisable k- $\varepsilon$  model and the previous two models. This is achieved through a variable  $C_\mu$  given by:

$$C_\mu = \frac{1}{A_0 + A_s \frac{kU^*}{\varepsilon}} \quad (2-31)$$

where:

$$U^* \equiv \sqrt{S_{ij}S_{ij} + \tilde{\Omega}_{ij}\tilde{\Omega}_{ij}} \quad (2-32)$$

and:

$$\tilde{\Omega}_{ij} = \Omega_{ij} - 2\varepsilon_{ijk}\omega_k \quad (2-33)$$

with:

$$\Omega_{ij} = \overline{\Omega_{ij}} - \varepsilon_{ijk}\omega_k \quad (2-34)$$

where  $\overline{\Omega_{ij}}$  represents the mean rate of rotation tensor as viewed in a moving reference frame and  $\omega_k$  is the angular velocity. Returning to the equation for  $C_\mu$ ,  $A_s$  is given by:

$$A_s = \sqrt{6} \cos(\phi) \quad (2-35)$$

where:

$$\phi = \frac{1}{3} \cos^{-1}(\sqrt{6} W) \quad (2-36)$$

and:

$$W = \frac{S_{ij}S_{jk}S_{ki}}{\tilde{S}^3} \quad (2-37)$$

with:

$$\tilde{S} = \sqrt{S_{ij}S_{ij}} \quad (2-38)$$

and  $S_{ij}$  is the same as previously defined. To close off the model, the constants involved in this model are as follows:

$$A_0 = 4.04, C_{1\varepsilon} = 1.44, C_2 = 1.9, \sigma_k = 1.0, \sigma_\varepsilon = 1.2 \quad (2-39)$$

## 2.5 Shear stress transport k- $\omega$ turbulence model

The final turbulence model used in the study is the SST k- $\omega$  model which can be described as a blend of the standard k- $\omega$  model and the k- $\varepsilon$  model, which is converted to a k- $\omega$  type model, whilst also accounting for the transport of turbulent shear stress. This blending of the two turbulence models allows the SST k- $\omega$  model to achieve the near-wall accuracy of the k- $\omega$  model whilst keeping the free stream turbulence independence of the k- $\varepsilon$  model. Of high importance to this model are the blending functions which will be discussed further on. In describing this model, as previously done, the transport equations for TKE and specific dissipation are:

$$\frac{\partial}{\partial t}(\rho k) + \frac{\partial}{\partial x_i}(\rho k u_i) = \frac{\partial}{\partial x_j} \left( \Gamma_k \frac{\partial k}{\partial x_j} \right) + \tilde{G}_k - Y_k + S_k \quad (2-40)$$

$$\frac{\partial}{\partial t}(\rho \omega) + \frac{\partial}{\partial x_i}(\rho \omega u_i) = \frac{\partial}{\partial x_j} \left( \Gamma_\omega \frac{\partial \omega}{\partial x_j} \right) + G_\omega - Y_\omega + S_\omega + D_\omega \quad (2-41)$$

where, as with the previous models, the terms from left to right represent: the rate of change, transport by convection, diffusivity, production, dissipation and a source term. The major difference between the k- $\epsilon$  and k- $\omega$  class of turbulence models is the use of  $\omega$ , which is the specific dissipation of TKE, and in the standard k- $\omega$  model is related to the dissipation rate as (Wilcox, 1994):

$$\omega \sim \frac{k}{\epsilon} \quad (2-42)$$

In the dissipation transport equation, the extra  $D_\omega$  term is a cross diffusion which will be presented further on. The term  $\Gamma_{(k,\omega)}$  represents the diffusivity of  $k$  and  $\omega$  and is given as:

$$\Gamma_{(k,\omega)} = \mu + \frac{\mu_t}{\sigma_{(k,\omega)}} \quad (2-43)$$

where  $\sigma_{(k,\omega)}$  are the turbulent Prandtl numbers for  $k$  and  $\omega$ . As mentioned, the SST k- $\omega$  model is a blend of two other turbulence models, hence the formulation of  $\sigma_{(k,\omega)}$  is calculated using a blending function as follows:

$$\sigma_{(k,\omega)} = \frac{1}{F_1/\sigma_{(k,\omega),1} + (1 - F_1)/\sigma_{(k,\omega),2}} \quad (2-44)$$

where  $F_1$  is a blending function. The equation for  $F_1$  is given as:

$$F_1 = \tanh(\Phi_1^4) \quad (2-45)$$

where:

$$\Phi_1 = \min \left[ \max \left( \frac{\sqrt{k}}{0.09 \omega y}, \frac{500 \mu}{\rho y^2 \omega} \right), \frac{4 \rho k}{\sigma_{\omega,2} D_\omega^+ y^2} \right] \quad (2-46)$$

and  $y$  is the distance to the next surface and  $D_\omega^+$  is the positive part of the cross diffusion term,  $D_\omega$  which will be shown further on. Regarding the blending function  $F_1$ ; its design is such that it goes from 1 at the object surface to 0 at the edge of the boundary layer. This ensures the switching from the k- $\omega$  to the k- $\epsilon$  model in the most appropriate regions.

When investigating the criterion  $\Phi_1$ , the first term considered in fact contains the turbulence length scale. This is seen by considering the relationship between  $\epsilon$  and  $\omega$  and noting that the turbulence length scale is defined as:

$$L_t = \frac{k^{\frac{3}{2}}}{\epsilon} \quad (2-47)$$

In the formulation by Menter (1992) the first term in the equation for  $\Phi_1$  ranges from 2.5 in the log region of the boundary layer, to 0 at the boundary layer edge. The second term in the equation is similar to that formulated in Menter (1992) with the difference being the constant is 500 as opposed to 400. Regardless, this term serves the same purpose which is to ensure that the blending function does not go to 0 in the viscous sub layer. When considering the third term, first the definition of  $D_\omega^+$  must be investigated, and is defined as the positive part of  $D_\omega$  which is described by:

$$D_\omega = 2(1 - F_1)\rho \frac{1}{\omega\sigma_{\omega,2}} \frac{\partial k}{\partial x_j} \frac{\partial \omega}{\partial x_j} \quad (2-48)$$

In the formulation by Menter (1992) the third term of  $\Phi_1$  was different to that used by FLUENT™ (2013) and served the purpose of being a safeguard against bad solutions for low free stream values of  $\omega$ . In this formulation it serves much the same purpose, as, considering the first term goes to 0 at the boundary layer edge, the free stream values for  $\Phi_1$  would come from a comparison between the second and third terms.

In the free stream, low values of  $\omega$  exist which in turn makes the second term large, however, low values of  $\omega$  result in larger values of  $D_\omega^+$ . This combined with the smaller values of  $k$  in the free stream will likely result in the third term of  $\Phi_1$  being the smaller term, causing  $\Phi_1$  to take on a small value and ensuring  $F_1$  goes to 0 thus enabling the k- $\epsilon$  model.

Another feature of the blending function  $F_1$  is to ensure that the k- $\epsilon$  model is enabled in free shear layers due to its ability to better predict the spreading of these shear layers compared to the k- $\omega$  model. By again looking at the second and third terms of  $\Phi_1$ , the large gradients of  $k$  and  $\omega$  will cause the third term to become small, thus dropping  $F_1$  to 0 and enabling the k- $\epsilon$  model.

Now to complete the description of  $\Gamma_{(k,\omega)}$ ; the definition for  $\mu_t$  is defined within FLUENT™ (2013) as:

$$\mu_t = \frac{\rho k}{\omega} \left[ \max \left( \alpha^*, \frac{\alpha_1 \omega}{S F_2} \right) \right] \quad (2-49)$$

where  $\alpha^*$  is:

$$\alpha^* = \alpha_\infty^* \left( \frac{\alpha_0^* + Re_t/R_k}{1 + Re_t/R_k} \right) \quad (2-50)$$

and:

$$Re_t = \frac{\rho k}{\mu \omega} \text{ and } \alpha_0^* = \frac{\beta_i}{3} \quad (2-51)$$

The second blending function,  $F_2$ , is also introduced in the description of turbulence viscosity, and it is described by:

$$F_2 = \tanh(\Phi_2^2) \quad (2-52)$$

where:

$$\Phi_2^2 = \max \left[ \frac{2\sqrt{k}}{0.09 \omega y}, \frac{500\mu}{\rho y^2 \omega} \right] \quad (2-53)$$

which is the mostly the same as the formulation by Menter (1992) with the exception of the constant in the second term being 500 instead of 400. This blending function is designed to again be 1 at the wall, however, is designed to extend slightly further into the boundary layer than  $F_1$ , according to Menter (1992), due to the modification to the turbulence viscosity having the greatest effect in the wake region of the boundary layer. The modification to the turbulence viscosity has also been designed by Menter (1992) to account for adverse pressure gradients. It can also be seen that the model implemented in FLUENT™ (2013) does take into account the effect of strain rate on the turbulence viscosity. This most likely applies in regions where  $F_2$  is small, corresponding to outside the boundary layer in regions where  $F_1$  is also small or 0. In this region the k- $\epsilon$  model applies and is known for its overproduction of turbulence in rapidly strained flows, hence the modification implemented in the SST k- $\omega$  has the effect of countering this overproduction. In order to close the description of the diffusivity terms for the transport equations; the constants involved in the applicable equations are:

$$\sigma_{k,1} = 1.176, \sigma_{k,2} = 1.0, \sigma_{\omega,1} = 2.0, \sigma_{\omega,2} = 1.168, \alpha_1 = 0.31, R_k = 6, \beta_i = 0.072, \alpha_{\infty}^* = 1.0 \quad (2-54)$$

Considering the TKE equation, the next term of concern is the generation term  $\tilde{G}_k$  which is given by:

$$\tilde{G}_k = \min(G_k, 10\rho\beta^*\omega) \quad (2-55)$$

where  $G_k$  holds the same definition as for the k- $\epsilon$  models previously described. The term  $\beta^*$  is given as:

$$\beta^* = \beta_i^* = \beta_{\infty}^* \left[ \frac{4/15 + (Re_t/R_{\beta})^4}{1 + (Re_t/R_{\beta})^4} \right] \quad (2-56)$$

The generation term for the dissipation equation is given by:

$$G_{\omega} = \frac{\rho\alpha}{\mu_t} \tilde{G}_k \quad (2-57)$$

with:

$$\alpha = \frac{\alpha_{\infty}}{\alpha^*} \left( \frac{\alpha_0 + Re_t/R_{\omega}}{1 + Re_t/R_{\omega}} \right) \text{ and } R_{\omega} = 2.95 \alpha^* \quad (2-58)$$

where:

$$\alpha_{\infty} = F_1 \alpha_{\infty,1} + (1 - F_1) \alpha_{\infty,2} \quad (2-59)$$

where the variables  $\alpha_{\infty,(1,2)}$  is calculated by:

$$\alpha_{\infty,(1,2)} = \frac{\beta_{i,(1,2)}}{\beta_{\infty}^*} - \frac{\kappa^2}{\sigma_{\omega,(1,2)} \sqrt{\beta_{\infty}^*}} \quad (2-60)$$

All the constants involved in the equations involving the production terms are:

$$\beta_{\infty}^* = 0.09, R_{\beta} = 8, \beta_{i,1} = 0.075, \beta_{i,2} = 0.0828, \kappa = 0.41 \quad (2-61)$$

The last terms to be considered for this model are the destruction terms for TKE and dissipation. They are as follows:

$$Y_k = \rho \beta^* k \omega \quad (2-62)$$

and:

$$Y_{\omega} = \rho \beta \omega^2 \quad (2-63)$$

where:

$$\beta = \beta_i \left[ 1 - \frac{\beta_i^*}{\beta_i} \zeta^* F(M_t) \right] \quad (2-64)$$

and:

$$\beta_i = F_1 \beta_{i,1} + (1 - F_1) \beta_{i,2} \quad (2-65)$$

also:

$$F(M_t) = \begin{cases} 0 & \text{if } M_t < M_{t_0} \\ M_t^2 - M_{t_0}^2 & \text{if } M_t > M_{t_0} \end{cases} \quad (2-66)$$

which is a term to account for compressibility effects as the definition of  $M_t$  is:

$$M_t = \frac{2k}{a^2} \text{ and } a = \sqrt{\gamma RT} \quad (2-67)$$

which shows a dependency on the speed of sound,  $a$ . The last set of constants to complete this model contains:

$$M_{t_0} = 0.25, \zeta^* = 1.5 \quad (2-68)$$

## 2.6 Large eddy simulation (LES)

Considering the widely recommended use of LES for bluff body aerodynamics, a brief overview of this method will be provided here. Note that the equations are cited from Sagaut (2004) and only apply to incompressible flows. Considering it has not been used in this thesis, an in depth description of LES is unwarranted.

The process of LES involves filtering the Navier-Stokes equations using a filter function which is designed to separate the large and small scales of turbulence. The filter applied to any quantity in the domain takes on the form:

$$\tilde{\phi}(\mathbf{x}, t) = \int_{-\infty}^{\infty} \int_{-\infty}^{\infty} \xi(\mathbf{x}', t') G(\mathbf{x} - \mathbf{x}', t - t') dt' d^3 \mathbf{x}' \quad (2-69)$$

where the most common filtering function is the top hat filter:

$$G(\mathbf{x} - \mathbf{x}') \begin{cases} \frac{1}{\Delta} & \text{if } |\mathbf{x} - \mathbf{x}'| \leq \frac{\Delta}{2} \\ 0 & \text{otherwise} \end{cases} \quad (2-70)$$

which decomposes the quantity concerned into:

$$\xi = \tilde{\xi} + \xi' \quad (2-71)$$

which looks similar to the decomposition from the time-averaging process to get to the RANS equations, however, has significantly different meaning. This decomposition represents a variable consisting of its resolved, large scale part denoted by the tilde and the modelled, small scale part denoted by the prime.

The large scales of turbulence are responsible for transport of majority of momentum, mass and energy whilst the smaller scales are more isotropic and universal. Applying the filtered equations to the continuity and Navier-Stokes equations, the new equations become:

$$\frac{\partial \tilde{u}_i}{\partial t} + \frac{\partial}{\partial x_j} (\tilde{u}_i \tilde{u}_j) = -\frac{\partial \tilde{p}}{\partial x_i} + \nu \frac{\partial}{\partial x_j} \left( \frac{\partial \tilde{u}_i}{\partial x_j} + \frac{\partial \tilde{u}_j}{\partial x_i} \right) - \frac{\partial \tau_{ij}}{\partial x_j} \quad (2-72)$$

where the term  $\tau_{ij}$  is known as the sub-grid-scale (SGS) stress and is the only term that requires modelling in LES and is done using one of a variety of models. Combining the definition of the filtering function and the filtered Navier-Stokes equations it can be seen that only the SGS stresses are solved in areas where the displacement between nodes is less than the cut-off width. Any further description of LES would be beyond the scope of this thesis, especially considering LES has not been used in this study.

## 2.7 Conclusions

From the various turbulence models analysed, it can be said that iterations to the standard  $k-\varepsilon$  model warrant investigation in obtaining accurate simulation results for flow over a heliostat. Considering the Realisable  $k-\varepsilon$  is bound by its equations to ensure always positive normal Re stress (a square quantity), making it closer to reality than the other two equation models explored, it would appear to possibly be useful in modelling the complex flow expected around a heliostat. The RNG  $k-\varepsilon$  model is also attractive in analysing flow over a heliostat. This due to the additional terms included in its formulation which allow it to compensate for the overproduction of turbulence associated with the standard  $k-\varepsilon$  turbulence model in rapidly strained areas, as could be expected in the wake of the heliostat. Lastly, the SST  $k-\omega$  is of interest due to it being a blend between the  $k-\varepsilon$  and  $k-\omega$  models which results in near-wall accuracy as well as low sensitivity to turbulence in the free stream. The performance of this model, due to these properties, in simulations of flow over a heliostat would thus be expected to give overall good results. Thus, based on the various recommendations presented here and the usage of the above three models in bluff body flows, discussed in the following section, these three models were chosen for analysis.

### 3. Literature Review

In order to find an appropriate starting point for simulations of flow over a heliostat, it was essential that a literature review be conducted on all available, relevant documentation. This would introduce a good background into previous work done in the field of receiver wind studies as well as other pertinent CFD, such as for bluff bodies. By studying this literature a more directed approach to simulating the flow over a heliostat could be attained.

#### 3.1 Geometry considerations

The development of heliostat geometries in the mid 1970 period to around 1980 had been driven by an attempt to reduce the cost of producing these heliostats (Kolb *et al.*, 2007). This process led to heliostats increasing in area from around 60 m<sup>2</sup> to around 100 m<sup>2</sup> which resulted in a 20 % cost reduction as realised by the McDonnell-Douglas aerospace corporation. Further size increases up to around 150 m<sup>2</sup> was the next step with a 148 m<sup>2</sup> heliostat having been in operation at the National Solar Thermal Test Facility in Albuquerque (Kolb *et al.*, 2007). With the aspect ratios of these heliostats being in the region of 1, these structures can be fairly tall.

Due to the height of such heliostats, scaled wind tunnel tests and CFD simulations have to be conducted using an atmospheric boundary layer (ABL) profile of velocity and turbulence as opposed to flat, aerodynamic profiles. Increases in various heliostat load coefficients, at various orientations, of around 20 % were found due to an ABL profile compared to an aerodynamic, flat profile (Cermak and Peterka, 1979). This shows the importance of correctly reproducing the ABL in simulations and experimentation. Details regarding the reproduction of the ABL are discussed further on.

#### 3.2 ABL modelling

As mentioned, the reproduction of the ABL in simulations and scaled testing is important in obtaining more realistic results due to the often significant height of the heliostat at full scale. Whilst the complete simulation and theory of the various ABL profiles to complete heights is beyond the scope of this thesis, reproducing the appropriate velocity and turbulence profiles to the height extent of the modelled domain is a concern.

The simplest method of producing an ABL velocity profile is using a power law based on a reference velocity, at a reference height, and an exponent based on surface roughness and stability of the ABL (Irwin, 1967). The power law is given by:

$$\frac{U}{U_{ref}} = \left( \frac{Z}{Z_{ref}} \right)^p \quad (3-1)$$

In the context of CFD, such a profile is specified at the inlet along with turbulence quantities thus describing the approaching flow within the domain. The issue then is that when using

this simple velocity profile there is no accompanying description of the turbulence properties to be prescribed apart from direct profile inputs from experimental measurements. In order to allow computational models of wind engineering problems to be solved, Richards and Hoxey (1993) developed boundary conditions for use with the k-ε turbulence model, amongst which the velocity and turbulence profiles at the inlet are prescribed. The equations given by Richards and Hoxey (1993) describing the inlet conditions are:

$$U = \frac{u_*}{\kappa} \ln \left( \frac{Z + z_0}{z_0} \right) \quad (3-2)$$

$$k = \frac{u_*^2}{\sqrt{C_\mu}} \quad (3-3)$$

$$\varepsilon = \frac{u_*^3}{\kappa(z + z_0)} \quad (3-4)$$

and  $u_*$  is calculated from equation (3-2) using a reference velocity at a reference height and the prescribed surface roughness length.

Other equations are included by Richards and Hoxey (1993) describing various other boundary conditions, such as the shear stress requirement at the top boundary of the domain. These additional conditions are, however, beyond the scope of this thesis as they are required only for the full modelling and sustain of the ABL throughout the flow domain. In studying the flow around a heliostat all that is required is that the correct turbulence and velocity profiles are realised at the heliostat location. Thus any further studies discussed which make use of velocity and turbulence profiles will be referred to as boundary layer flow as this signifies the use of just a very small part of the ABL.

### 3.3 Receiver wind load studies

Much of the work done on quantifying wind loads on heliostats has been done in the past by means of wind tunnel testing of scaled models of heliostats. One of the largest bodies of work produced in this manner is that of Peterka and associates from around 1979 to around 1992 (Cermak and Peterka, (1979), Peterka *et al.*, (1986), Peterka *et al.*, (1987), Peterka *et al.*, (1988), Peterka and Derickson, (1992)).

An important work was released by Cermak and Peterka (1979) in which a scale heliostat model was tested in both aerodynamic and meteorological wind tunnels. The meteorological wind tunnel was required in order to simulate the boundary layer to capture real world loads and to investigate the effects of shear and turbulence on the wind loads. The Reynolds number (Re) values used in the wind tunnel tests were of the order of  $10^5$ - $10^6$ , which are two orders of magnitude less than the full scale flow, however, for Re greater than about  $2 \times 10^4$  there is no significant change in loading coefficients for sharp edged bodies (Pfahl and Uhlemann, 2011). This allowed for acceptable flow similarity and results, when compared to the full scale, to be obtained.

The results of concern within the work of Peterka were the various loading coefficients which describe the forces on the heliostat, moments about the base of the heliostat and moments about the hinge of the reflector surface. These were determined in the x, y, and z axes in order to obtain the load data required for the drive mechanisms and structural stability. Also note that the coefficients reported in the works of Peterka were the time-averaged coefficients which would indicate that they were capable of transient measurements, however, they do not report on them. The mathematical description of these load coefficients follows, as well as a geometric description in Figure 3-1. Note that the angles  $\alpha$  and  $\beta$  are referred to as the inclination and azimuth angles respectively.

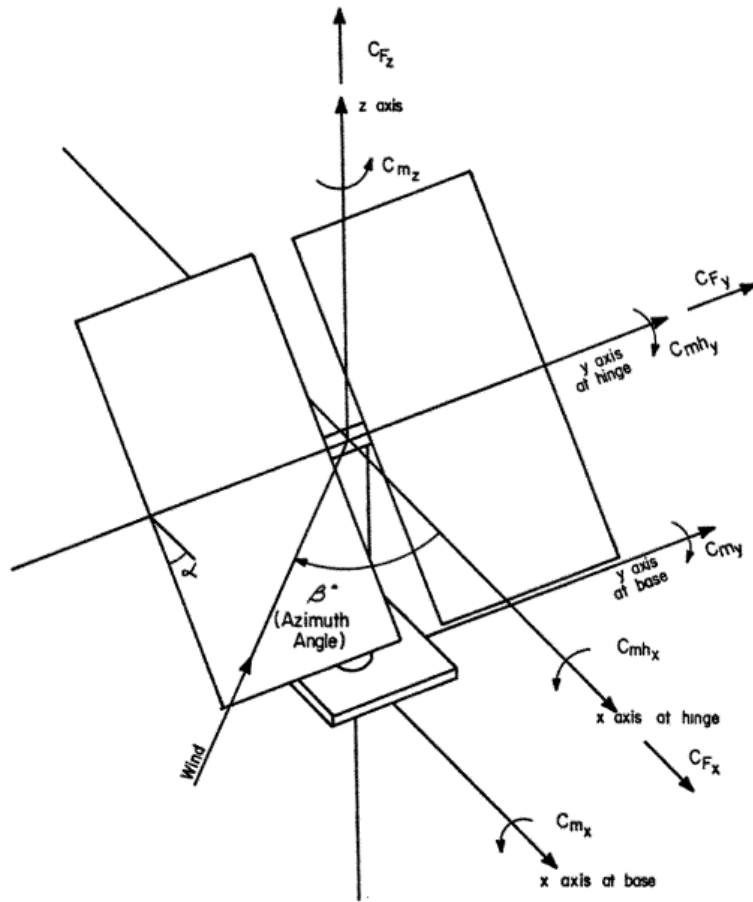


Figure 3-1: Geometric description of load coefficients (Cermak and Peterka, 1979)

The mathematical description of the force coefficients,  $C_{f(i)}$ , are as follows (Peterka *et al.*, 1988):

$$C_{f(i)} = \frac{F_{(i)}}{(0.5\rho A_{ref} U^2)} \quad (3-5)$$

When defining the moment coefficients, the moments about the base and the hinge are of concern. The moments about the hinge are defined as (Peterka *et al.*, 1988):

$$C_{MH(i)} = \frac{M_{H(i)}}{(0.5\rho L_{ref} A_{ref} U^2)} \quad (3-6)$$

and the base moments are defined as:

$$C_{M(i)} = \frac{M_{(i)}}{(0.5\rho(HCL)A_{ref}U^2)} \quad (3-7)$$

Note that the moment coefficient about the z axis is calculated in a slightly different manner to the previously defined moments. The moment about the z axis is given by Peterka *et al.* (1988) to be:

$$C_{M(z)} = \frac{M_z}{(0.5\rho L_{ref} A_{ref} U^2)} \quad (3-8)$$

Along with these definitions; Peterka *et al.* (1988) had also related the overturning moment,  $C_{M(y)}$ , to the hinge moment about the y axis. The resultant equation is:

$$C_{M(y)} = \frac{C_{MH(y)}H}{HCL} + C_{F(x)} \quad (3-9)$$

In evaluating these loading coefficients, Cermak and Peterka (1979) recognised that when the inclination is  $90^\circ$  and the azimuth is  $0^\circ$ , the drag coefficient on the heliostat was similar to that of a flat plate in the same orientation. This was, however, found only in uniform flow whilst the boundary layer flow produced different values for drag at this orientation. The difference in loadings between the uniform and boundary layer flow was found to occur for majority of the orientations tested by Cermak and Peterka (1979). This illustrates the importance of correctly reproducing the boundary layer velocity and turbulence profiles in simulations or scaled tests as it does have a significant impact on the loadings encountered on a heliostat.

Another finding by Cermak and Peterka (1979) was the fact that no marked periodicity was found in the unsteadiness of the flow. This is an unexpected outcome as vortex shedding is commonly found behind inclined flat plates, for which the geometry is very similar to that of a heliostat. A study done regarding vortex shedding behind flat plates near the ground plane, by Matty (1979), utilised a geometry that is extremely similar to a heliostat. This was done in order to allow the flat plate to change its inclination angle by attaching it to a hinge on an upright support rod which kept it in close proximity to the ground plane. The geometry used for a large part of the study by Matty (1979) can be seen in Figure 3-2.

The work done by Matty (1979) involved wind tunnel testing of both 4" (10.16 cm) and 8" (20.32 cm) square flat plates as well as a slotted 4" plate. The 8" square plate was tested only perpendicular to the flow, and mounted on the ground, whilst the 4" plate was tested at various inclination angles and distances from the floor. One important finding for the case of vertical, ground mounted plates was that the Strouhal number (St), which describes vortex shedding, was independent of the size of plate and was a weak function of Re. It was also

found that the difference in  $St$  between the slotted and solid plate was only about 6 % at higher  $Re$  of the order  $10^5$ .

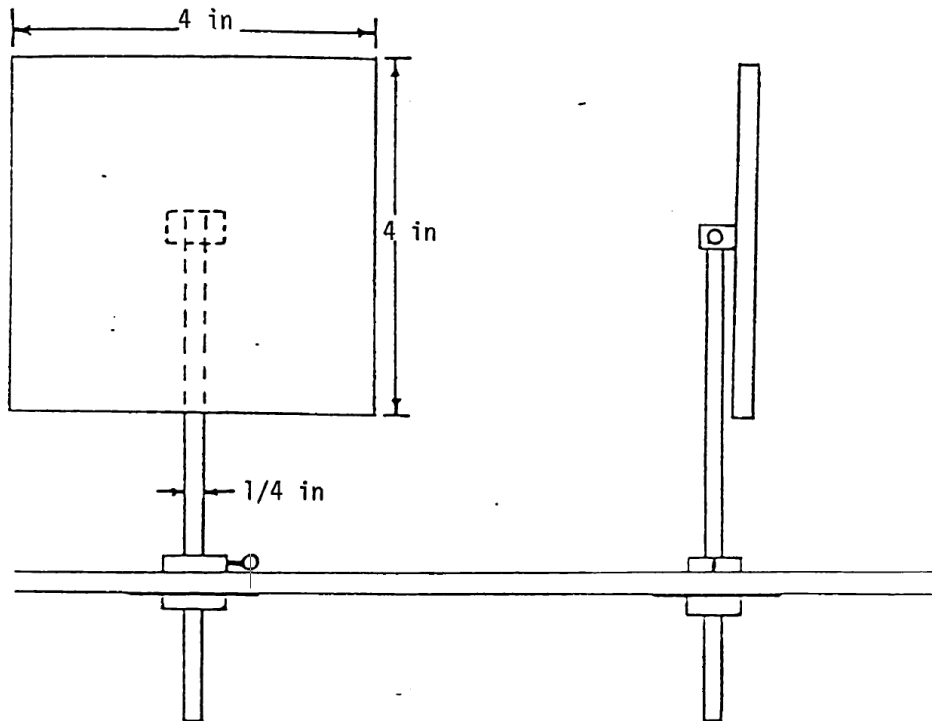


Figure 3-2: Geometry used in vortex shedding study (Matty, 1979)

One of the main outcomes of the work done by Matty (1979) is the functions relating  $St$  to  $Re$  of the flow, as well as to the ratio of plate chord length to distance above ground ( $L/h$ ), shown in Figure 3-3.

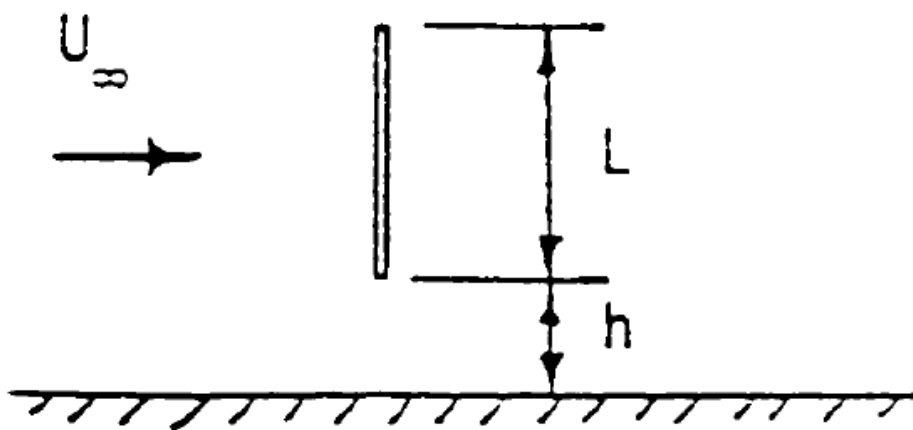


Figure 3-3: Chord to height above ground ratio (Matty, 1979)

The equations relating  $L/h$ ,  $Re$  and  $St$  were found to be accurate to within 5 % at the higher  $Re$  tested. This has the possibility of thus providing info regarding possible time step

selection on simulations aimed at capturing transient flow features such as vortex shedding. The equations formulated by Matty (1979) are provided below. It should be noted that these equations only apply to flat velocity and turbulence profiles.

$$St = g_h \left( \frac{h}{L} \right) S_\infty(Re) \quad (3-10)$$

$$g_h = 1 + 0.518 e^{-4.6(h/L)} \sin[18^\circ \left( 20 \frac{h}{L} - 1 \right)] \quad (3-11)$$

$$S_\infty = 0.121 + \frac{407}{Re} \quad (3-12)$$

One of the issues regarding the studies discussed thus far is the use of flat velocity and turbulence profiles, along with very low levels of turbulence intensity, around 1 % or less. It has, however, been mentioned that the study by Cermak and Peterka (1979) used both uniform and boundary layer profiles which resulted in drag and lift coefficients varying due to the varying profiles. Due to the greater relevance of the boundary layer flow results, all subsequent studies on solar collectors conducted by Peterka and associates only used the boundary layer flow.

The study by Peterka *et al.* (1986) had used a different geometry to Cermak and Peterka (1979), and focused more on mean wind load reduction on heliostats. In this study a few fluctuating force measurements were taken which indicated future experimentation towards directly measuring peak loads as compared to using gust factors on mean loads. Whilst investigating the load reduction within a field of heliostats, Peterka *et al.* (1986) also introduced the concept of general blockage area (GBA) which is the ratio of upwind solid blockage area to the ground area occupied by the upwind blockage element. By describing this quantity Peterka *et al.* (1986) was able to find the relation between load reduction (as a ratio of in-field to isolated load coefficient) and GBA for a few orientations.

In 1987 Peterka *et al.* (1987) then investigated mean and peak wind load reduction for heliostats. This study again used a different geometry to all prior studies by Peterka and associates, and even considered porous edged and circular heliostat models. It also included an investigation into the sensitivity of the wind loads to the boundary layer turbulence intensity levels. This revealed a surprisingly high sensitivity for lift and drag to incoming turbulence levels when the heliostat was within about 45° of perpendicular to the wind. This was, however, only found by coincidence and was only confirmed by further experimental work by Peterka *et al.* (1988). In the study of Peterka *et al.* (1988) the primary focus was on wind loads on parabolic dish collectors, however, special attention was also paid to confirming the turbulence intensity sensitivity of heliostat wind loads. The body of work by Peterka and associates has been summarised by Peterka and Derickson (1992) in a design method for ground based heliostats and parabolic dish collectors.

### 3.4 Numerical wind load studies

In studying flow phenomenon CFD has a few advantages over traditional scale model testing such as: reduced turnover time and costs, simulation of systems that are experimentally difficult or impossible to setup, simulation of hazardous systems and extremely comprehensive information about the solution given at each mesh node (Versteeg and Malasekera, 2007). With the advancement of computing power since the 1990's, CFD provides an attractive option in analysis of a wide range of flow phenomenon.

An example of CFD work that has been conducted in the area of solar collectors is that of Naeeni and Yaghoubi (2007) who conducted a two-dimensional analysis of a parabolic trough. In their study the RNG k- $\epsilon$  model was used along with an open terrain boundary layer to evaluate the wind flow patterns around the collector and forces on the collector. This was also done at a range of Re from  $4.5 \times 10^5$  to  $2.7 \times 10^6$  and at various collector orientations ranging from  $0^\circ$  to  $+90^\circ$  in  $+30^\circ$  increments.

CFD studies by Wu and Wang (2008) were conducted on a full scale heliostat model with some simplifications, namely, excluding the gap between facets and excluding the back support structure. Simulations were conducted using a modelled boundary layer and the standard k- $\epsilon$  and SST k- $\omega$  models for the heliostat in two orientations. The domain was meshed using tetrahedral cells, and a mesh independence study showed no change in solution above 180 000 cells. The data obtained from CFD simulations were compared to experimental data, however, the only information given for the experimental study is the scale at which it was conducted, namely, 1:10.

Results of Wu and Wang (2008) showed inaccuracies of the CFD around 35 % for  $F_{(x)}$  with the heliostat perpendicular to the flow. In this orientation the lift, however, showed inaccuracies of around 94 % and 99 % for the SST k- $\omega$  and k- $\epsilon$  model respectively. The overturning moment,  $M_{(y)}$ , showed over prediction of around 45 % when using either turbulence model. At an orientation of  $\alpha$  at  $10^\circ$  and  $\beta$  at  $45^\circ$ , all results are grossly inaccurate as predicted by CFD. Wu and Wang (2008) reached the conclusion that errors had existed in the experimental investigation conducted, and that CFD would in fact prove useful for heliostat design.

The effect of the gap between heliostat facets has on the overall load on a heliostat has been investigated by Wu *et al.* (2010). The results obtained using the standard k- $\omega$  turbulence model showed good agreement with the experimental data, with the study revealing that the gap between facets actually increases the wind load on the heliostat. This is a result of the flow through the gap resembling a jet flow, consequently decreasing the pressure on the leeward side of the heliostat, thus increasing the load due to the pressure difference between the windward and leeward side of the heliostat. The authors did, however, conclude that this effect is insignificant when compared to the overall load on the structure.

Other work done using CFD for collector analysis is that of Sment and Ho (2012) who investigated the velocity profiles above a full scale, single heliostat. Their study involved

taking field measurements of both the boundary layer encountered at the location, as well as the velocity profiles above a heliostat located at the edge of the field. These measurements were then used to provide the boundary layer conditions for the CFD analysis as well as to provide a means to validate the CFD analysis. Results obtained from this study showed the CFD to be accurate within a range of 0-23 % across the points of measurement and the corresponding points in the CFD analysis.

### 3.5 Other bluff body CFD

Before a discussion of bluff body CFD investigations can be given, a brief description of algebraic stress (ASM) and Reynolds stress (RSM) turbulence models will be given. This is due to their appearance in the following section, however, a full description of such models is beyond the scope of this thesis. The ASM approximates the convection and diffusion terms of the exact transport equation of the Reynolds stress using an algebraic equation (Murakami, 1993). This is different to the complete RSM in which these terms are fully modelled.

Bluff body flows can be described as flows in which boundary layer separation is inevitable and the main source of drag on a bluff body originates from pressure rather than viscous drag. Examples of such flows include flow around a circular cylinder, a cube, an inclined flat plate and so on. With regards to flat plates, bluff body flow can be seen for plates inclined by  $12^\circ$  to  $90^\circ$  in which periodic velocity fluctuations are observed downstream of the plate (Fage and Johansen, 1927). This is indicative of vortex shedding associated with bluff body flow.

In terms of numerical studies on bluff body flows; the range of studies that have been conducted is too vast to be entirely described here. In the context of this thesis all that is required is a description of a few bluff body CFD studies in which the appropriateness and accuracy of the various turbulence models is explored.

Amongst the earliest works concerned with bluff body CFD was done by Murakami (1993) in which the flow field around a two dimensional, square rib was resolved using the standard  $k-\epsilon$  model, ASM and LES. Murakami (1993) found that each turbulence model accurately predicts the mean velocity vector field, however, there were various accuracy issues concerning turbulence values. A large part of this is due to the production term in the turbulence models and the part the strain rate tensor has in the production of TKE combined with the complex distribution of the strain rate tensor around a bluff body. The various velocity gradients making up the strain rate,  $\partial u_i / \partial x_j$ , is shown in Figure 3-4. The sharp gradients and high anisotropy of the strain rate field leads to inaccuracies for prediction of the TKE using the  $k-\epsilon$  model and issues with the production term for the ASM method. The details regarding the shortcomings ASM and LES are not discussed as this thesis is solely concerned with the two equation RANS turbulence models.

When Murakami (1993) closer looked at the cause of excess TKE using the  $k-\epsilon$  model it was found to be the overly large, diagonal production term in the impinging zone, near the frontal corner. This is caused due to the Re stress terms being added together when using the eddy-viscosity modelling approach, under the assumption that these stresses are isotropic, as

opposed to the subtraction between these terms when resolving them from the exact equations. The error incurred by diagonal elements of the strain rate tensor will in fact apply to all eddy viscosity models. A further issue is that eddy viscosity models cannot resolve the anisotropic components of the Re stress as it assumes isotropy of these stresses in formulating the turbulence viscosity. This only works well for simpler and more aerodynamic flows.

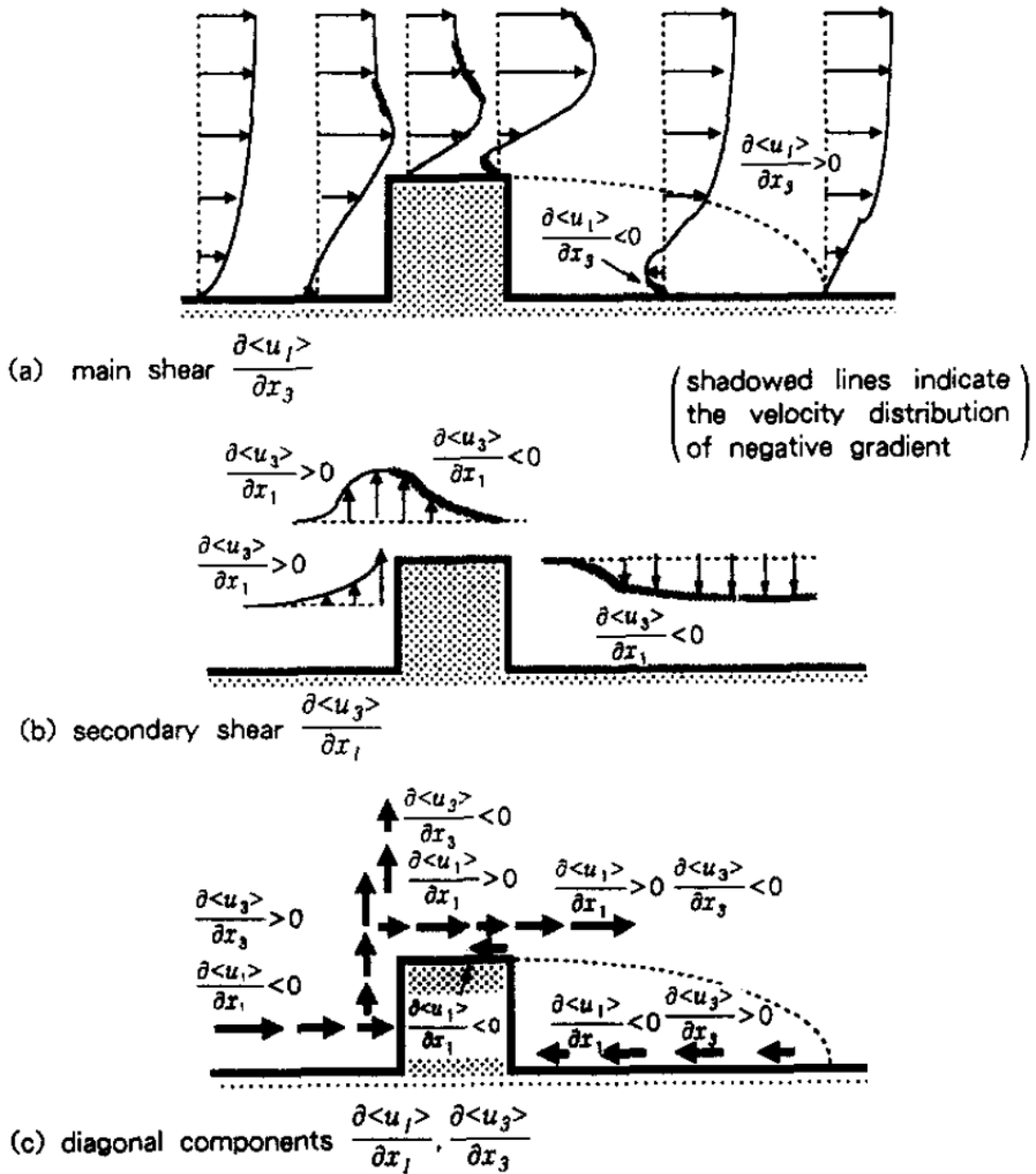


Figure 3-4: Strain rate tensor distribution (Murakami, Comparison of various turbulence models applied to a bluff body, 1993)

A study by Rodi and Lakehal (1997) utilised the standard k-ε in its original form, as well as with the modification of Launder and Kato (LK), in order to investigate the flow around a three-dimensional surface mounted cube. The LK modification alters the production term in the ε equation from  $C_\mu S_{ij} S_{ij}$  to  $C_\mu S_{ij} \Omega_{ij}$  where:

$$\Omega_{ij} = \sqrt{\frac{1}{2} \left( \frac{\partial u_i}{\partial x_j} - \frac{\partial u_j}{\partial x_i} \right)^2} \quad (3-13)$$

They also used standard wall functions and a two-layer approach in which the viscous sub layer is solved with a one equation model. They found that separation over the roof was too small with the standard k- $\epsilon$  model, with unrealistic reattachment of the flow on the roof. The LK model showed to improve this separation prediction and reduced the overproduction of turbulence kinetic energy found with the standard k- $\epsilon$  model.

Lee (1997) investigated flow around a two-dimensional surface mounted cube, as viewed from above, better described as an infinitely long square. The simulations included the standard, RNG and low-Re k- $\epsilon$  models as well as comparative LES and experimental results. Results revealed a poor performance of the standard k- $\epsilon$  model, with largely under-predicted drag and lift results. The RNG and low-Re k- $\epsilon$  models revealed greatly improved results over the standard k- $\epsilon$  model, both in predicting drag and lift forces, as well as greater accuracy of the Strouhal number. The RNG k- $\epsilon$  model, however, does over predict the size of the separation bubble at the back whilst the standard k- $\epsilon$  under predicts its size. The fairly accurate prediction of drag and lift forces, however, does show some promise in the use of the RNG k- $\epsilon$  model.

Murakami (1998) provided an overview of the turbulence modelling capabilities in CFD applied to wind engineering. In the study he commented on the requirement for a fine mesh at the wall surface in order to accurately use no-slip wall conditions. The suggestion made is for the first cell to contain a  $y^+$  value of less than 1. Loosely related to meshing; Murakami (1998) pointed out that a sharp corner in the bluff body geometry acts as a ‘singular’ point which creates ‘wiggles’ in the solution which are spread upwind. This can be overcome by using lower order discretisation schemes which are more diffusive.

With regards to the turbulence modelling, the standard k- $\epsilon$  model is again shown to be insufficient for bluff body flows. When looking at the LK k- $\epsilon$  an issue that arises is that in regions where  $\Omega_{ij} > S_{ij}$  TKE is over-predicted more so than with the standard k- $\epsilon$  model. It is also shown that the production term in the  $k$  equation, as well as the  $k$  equation itself, appear different from the standard k- $\epsilon$   $k$  equation which is in fact derived exactly. This shows that the LK k- $\epsilon$  formulation is more mathematically inconsistent with the physics of the flow. The drawbacks of the LK modification are addressed in the Murakami-Mochida-Kondo (MMK) modification. This alters the formulation of the turbulence viscosity as opposed to production of TKE whilst accounting for both vorticity and strain. Murakami (1998) does also address RSM, however, this does not fall into the class of two equation RANS turbulence models and hence will not be addressed here.

Rodi and Bosch (1998) looked at the vortex shedding past a two-dimensional square cylinder using the same turbulence models and methods of wall treatments as in Rodi and Lakehal (1997). This study revealed, again, the weak performance of the standard k- $\epsilon$  model with regards to bluff body aerodynamics. This was found by comparing the drag coefficients from

simulation and experimentation, and with both wall treatments the standard  $k$ - $\epsilon$  model was found to perform poorly.

The work of Kim and Boysan (1999) investigated the issues of meshing and turbulence modelling for CFD applied to environmental flows such as flows over an urban terrain. They also point out some of the issues regarding CFD for wind applications to buildings or structures. Applicable issues to modelling the flow about heliostats would include the correct modelling of the boundary layer as well as a complex flow field containing elements which fluid mechanics has not yet successfully resolved. Such features include a highly three-dimensional flow field accompanied by strong streamline curvature, separation and vortices. The large variety of temporal and spatial scales of turbulence also poses a challenge if they were to all be resolved through simulation.

In terms of meshing, Kim and Boysan (1999) suggest the use of unstructured meshes for meshing the associated geometry. This is due to the complexity of the associated geometry when multiple structures are involved, as well as the resultant high mesh resolution in areas it is not needed when employing a structured mesh. The use of unstructured meshes also allows for local mesh refinement which ensures that a fine mesh only exists where it is needed. Unstructured meshing also allows for 'solution adapted' meshes where the mesh can be refined in local areas based on some criterion obtained from the solution using the original mesh, such as refinement based on pressure gradient.

With regards to turbulence modelling, Kim and Boysan (1999) found that for a flow modelled over a curved hill the RSM produced the best results when compared to the standard, Realisable and RNG  $k$ - $\epsilon$  models. They also found that the RNG and Realisable  $k$ - $\epsilon$  did produce slightly improved results over the standard  $k$ - $\epsilon$  model in predicting pressure recovery in the wake region. Overall Kim and Boysan (1999) conclude that all eddy viscosity based  $k$ - $\epsilon$  models are prone to overproduction of turbulence due to the generation term in the TKE equation always being positive. This leads to the reduction and even suppression of flow separation for certain bluff bodies, however, the modification contained within the RNG and Realisable  $k$ - $\epsilon$  models have shown great improvements. This shows that the  $k$ - $\epsilon$  class of models may still have more to offer in CFD with regards to bluff bodies.

A report by Franke *et al.* (2004) contained guidelines with regards to CFD applied to wind engineering. In the context of this study, the information contained within Franke *et al.* (2004) on turbulence modelling is of great importance. The RANS turbulence models mentioned within the guidelines are the standard, Realisable, RNG, LK and MMK  $k$ - $\epsilon$  and the SST  $k$ - $\omega$ . As with the prior studies, the standard  $k$ - $\epsilon$  model is not encouraged for wind engineering, however, the authors do mention that the ad-hoc modifications with the LK and MMK models does provide much improved results. The authors also cite that the Realisable and RNG  $k$ - $\epsilon$  models attenuate the stagnation point issue whilst not leading to any worse results in the wake of the body. The SST  $k$ - $\omega$  is cited as also showing greatly improved results over the standard  $k$ - $\epsilon$  model for bluff body flows making it a viable model for investigation.

### 3.6 Conclusions

From the literature considered in this chapter, it can be concluded that in order to accurately obtain design loads for a heliostat, some form of boundary layer flow is essential for both simulation and wind tunnel testing. In this regard, there are guidelines in place for prescribing boundary conditions for boundary layer flow; however, the additional boundary conditions required to sustain such a boundary layer may point to the current turbulence models being inadequate in producing and sustaining the correct profiles if used just as they are.

In terms of work done in the area of receiver wind load studies there is definitely a comprehensive body of work already compiled in this area by Peterka and associates. This is, however, only in terms of wind loadings on heliostats and there is a need for data concerning the flow field around a heliostat or heliostat like geometry. With regards to numerical studies of flow over a heliostat, both load coefficient studies and velocity profile studies have been conducted but there is very little detail provided about the manner in which these studies were conducted. When compared to the database of experimental studies as numerical bluff body studies, it would appear as if this area has not been comprehensively investigated.

## 4. Flat Plate Simulations

Before undertaking simulation of complete heliostat geometries, an understanding of the turbulence models and various modelling parameters is required to ensure efficient and accurate simulations. This was achieved by conducting simulations on a simple flat plate oriented perpendicular to the flow. These simulations are detailed in this chapter with the purpose of selecting a single turbulence model to conduct the heliostat simulations with for reasons to be discussed in section 4.5.

### 4.1 Simulation geometry

The geometry used in the flat plate simulations is the same as that contained within Matty (1979) as this contains details of the frequency of the vortex shedding exhibited under various circumstances. The drag coefficient for a flat plate can also be obtained from Fail *et al.* (1959), thus resulting in the combination of the two studies providing a comprehensive data source to verify and understand the simulations conducted. The geometry, with dimensions, used in the study by Matty (1979) can be seen in Figure 3-2 and the geometry generated to be used in this study can be seen in Figure 4-1 which shows the plate with a chord to gap ratio of 1/4 as well as being ground mounted.

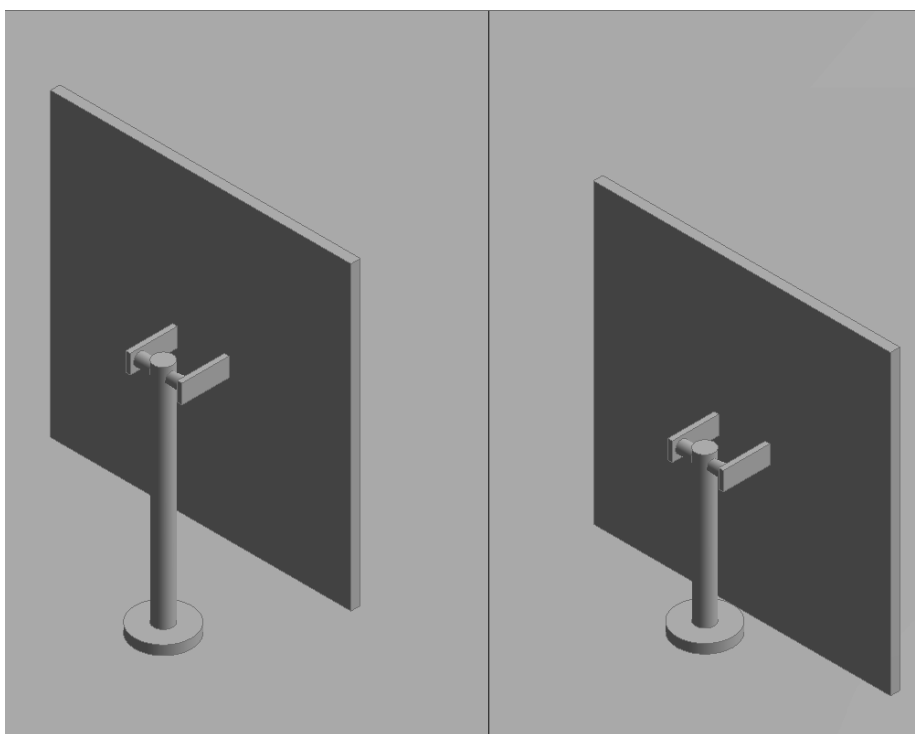


Figure 4-1: Flat plate geometry with 1/4 gap to chord ratio (left) and ground mounted (right)

The geometry was initially generated using Autodesk Inventor and exported as an .iges file in order to be imported to ANSYS Workbench. Once imported, the geometry was checked for errors such as hard edges and subsequently repaired. A solid box was then generated around

the flat plate geometry which would later make up the flow domain. The limits for this bounding box were kept the same for both orientations and can be seen Figure 4-2. The bounding box measured 0.8 m upstream of the heliostat and had a total length of 2.1 m along this direction. The total height of the bounding box was 0.6 m and the overall width was also 1.2 m. The width and height of the bounding box was found, when looking at the results, to be appropriate as there was no squeezing of streamlines close to the side or top walls as well as showing a constant pressure along the wall surfaces. This is demonstrated in Appendix A: Domain Width and Height.

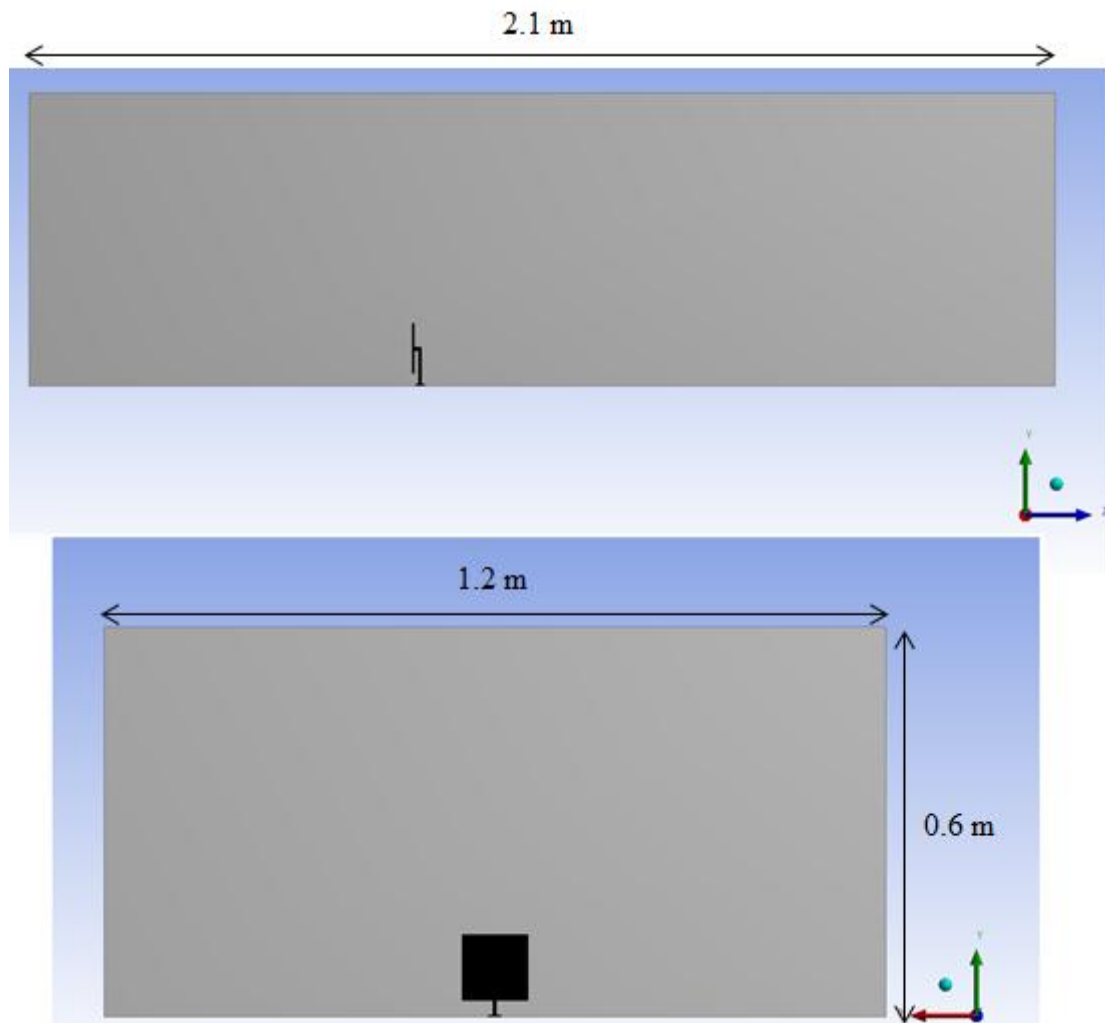


Figure 4-2: Flat plate within domain geometry side view (top) and front view (bottom)

The next step was to create the fluid volume which would be used in the simulation and this was done by subtracting the solid model of the flat plate from the bounding box. This leaves the fluid volume surrounding the heliostat which was then meshed.

#### 4.2 Meshing method

Once the fluid volume was created, the domain needed to be meshed which divides the domain into control volumes. This allows the discretised equations to be solved iteratively for

the entire domain. With regards to meshing, the two areas of concern are the shape of the cells and the way in which they are arranged. There are 3 major shapes of cells which are Cartesian, hexahedral and tetrahedral (prism cells are included further on although due their use in this study). Cartesian cells are similar to hexahedral cells with the difference being that they are exactly cubes in three-dimensions and are aligned with the Cartesian coordinate system (Mentor Graphics, 2010). These various cell shapes can be seen in Figure 4-3 with the Cartesian cell omitted as it is simply a cubic hexahedral cell. Pyramidal cells are also not shown as these are simply a tetrahedral cell with a four-sided base.

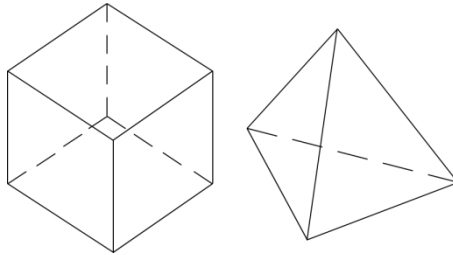


Figure 4-3: Cell types: hexahedral (left) and tetrahedral (right)

In terms of how the cells are arranged; it can be in a structured, unstructured or partially unstructured manner (Mentor Graphics, 2010). Considering the complex geometry of the plate assembly being modelled; a structured arrangement was not possible, meaning only an unstructured or partially unstructured meshing arrangement was viable. A fully unstructured mesh would have been the simplest and the quickest to generated, however, this arrangement is associated with tetrahedral cells which have some undesirable properties.

The most severe of these issues is the introduction of additional terms into the coefficients for the discretised equations which can tend to grow larger the further the cell is from being orthogonal (Mentor Graphics, 2010). These additional terms also create certain ‘cross-linkages’ which creates a dependence of the solution at one node on more remote values. This has implications of reduced accuracy and even solution instability, with the fix being creating a finer mesh (Mentor Graphics, 2010). This combined with the additional computation time associated with extra terms for each iteration, and the added storage requirements for these terms meant that an unstructured, tetrahedral mesh was not desired. The most attractive meshing options was thus to use a partially unstructured mesh.

By using cut-cells to generate the mesh, a Cartesian, partially unstructured mesh could be generated. This method of meshing also allows the use of inflation layers, which generate prismatic cells at wall surfaces to capture boundary layers at the wall. A prism cell can be seen in Figure 4-4, with the top or bottom making up the wall surface.

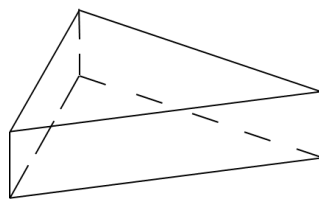


Figure 4-4: Cell type: prism

In a cut-cell mesh, prism cells also allows for the transitions between different sizes of Cartesian cells without the need to average values across the smaller faces when transitioning from small to large cells. An example of a zone in which this takes place can be seen in Figure 4-5. Note that the mesh is three-dimensional, however, due to the orientation of the view being along a Cartesian axis the cells appear as two-dimensional.

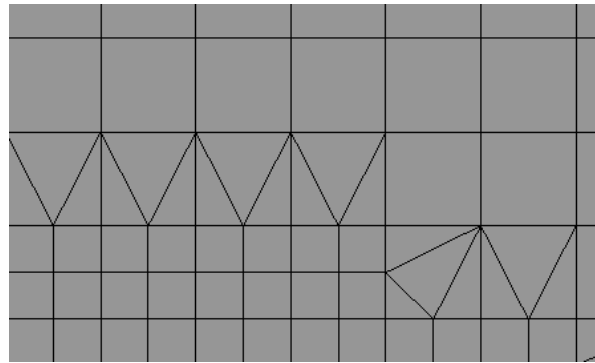


Figure 4-5: Transition from small to large cells using prism cells

All things considered, the Cartesian cut-cell mesh proved to be the most attractive option to mesh the domain. For the domain, two different meshes were created for each orientation with one mesh being finer than the other. This was done in order to check the effects of mesh density on the solution obtained. The side view of a cross section through the centre of the domain with these two meshes can be seen in Figure 4-6. Note only the ground mounted plate orientation is shown as the slight gap does not significantly affect the overall mesh. The number of cells contained within the coarse and fine meshes was approximately 650 000 and 1 600 000 respectively. Note that the method of mesh refinement was based on the change in load coefficients for each simulation and, where possible, the mesh was refined in the wake of the heliostat. This is the region in which large pressure and velocity gradients may appear and thus a solution based refinement approach may have proved more efficient.

It is also during the meshing stages that the ‘named selections’ are allocated. This entails naming the various surfaces within the domain in order to assign boundary conditions to the correct surfaces at a later stage. An example of a named selection would be naming the front surface upwind of the heliostat as ‘inlet’. This will ensure that this surface can be recognised within FLUENT™ as well as automatically being assigned as a velocity inlet. This can be seen in Figure 4-7.

### 4.3 Simulation settings

#### 4.3.1 General settings

Once within FLUENT™, the appropriate modelling parameters needed to be defined. With the FLUENT™ interface, the user works in a ‘top to bottom’ manner in which the desired parameters are assigned at each step. The first step was to select the general simulation conditions. At this stage, the simulation was set to a pressure-based solver. This was due to the effect of compressibility not being significant to the simulation as the wind speed (around

23 m/s based on Matty (1979)) was less than 10 % the speed of sound. The simulation was also initially set to steady state to achieve better initial conditions for the transient simulation. The velocity formulation was also set to absolute as there were no rotating components in the domain to which a relative velocity formulation would be necessary.

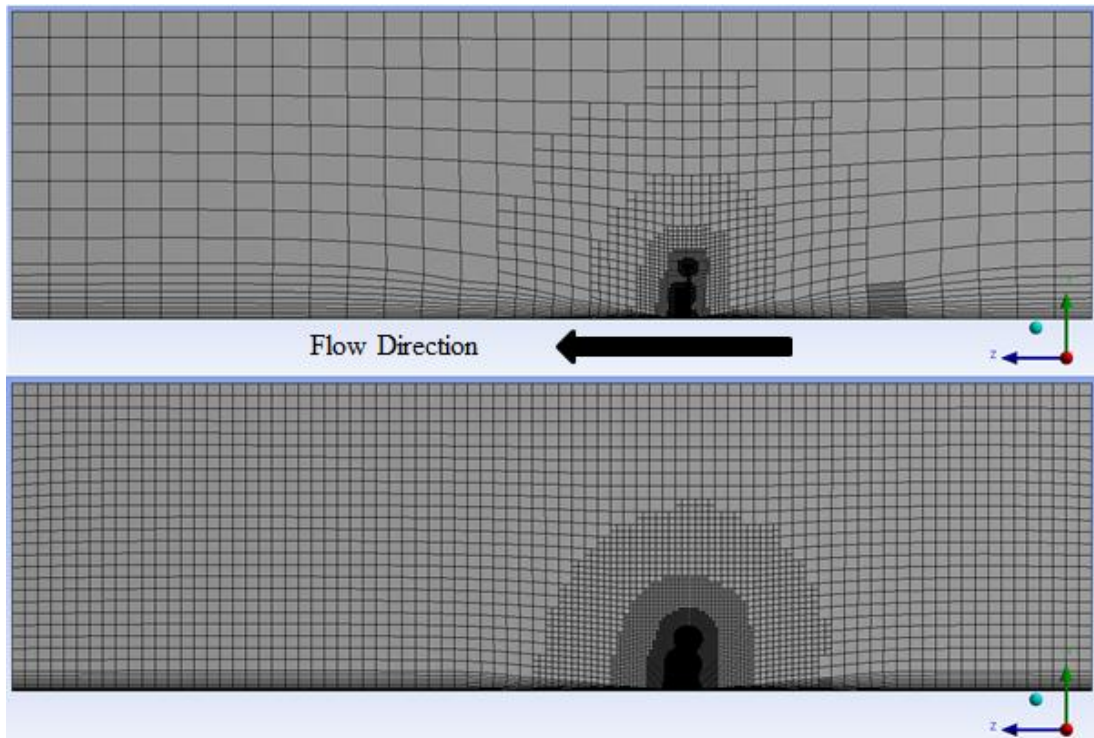


Figure 4-6: Coarse (top) and fine (bottom) meshes generated

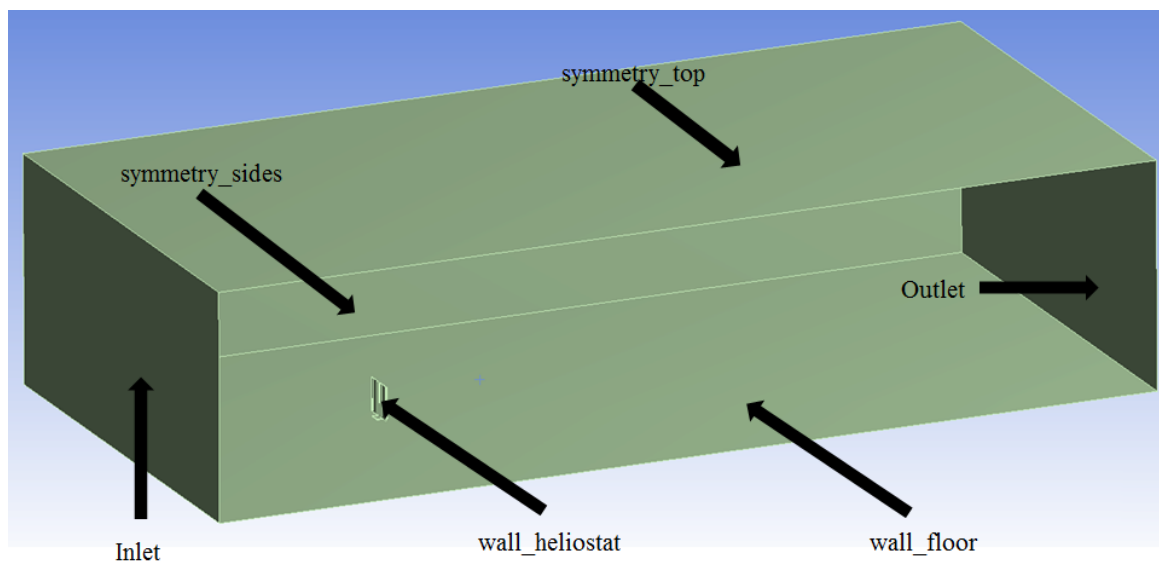


Figure 4-7: Inlet named selection

#### 4.3.2 *Models and wall treatment*

The next step was to choose the models employed in the simulation and it was at this step that the simulation was set as laminar or turbulent. Considering the large Reynolds number of around  $1.5 \times 10^5$ , a turbulent flow regime was selected. With regards to the turbulence models used in the simulation; three different variations were used over the course of the flat plate modelling, namely, the RNG k- $\epsilon$ , Realisable k- $\epsilon$  and SST k- $\omega$  models.

With regards to the k- $\omega$  class of models, the wall treatment is set by FLUENT™ as enhanced wall treatment (EWT). This method integrates the equations right down to wall, as this is possible for the  $\omega$  equation. Ideally EWT requires a  $y^+$  value of around one, however FLUENT™ (2013) uses a two layer model which ensures  $y^+$  independence. This is attained by blending the laminar sub layer with the log-law region within the boundary layer which means that even if  $y^+$  is much greater than 1, a solution can still be attained by applying the log-law.

For the k- $\epsilon$  class of models, however, the wall function approach was chosen, using the non-equilibrium wall functions. The non-equilibrium wall functions have an additional term to the regular law of the wall which allows it to deal with adverse pressure gradients as would be expected in the wake of the plate.

The wall function approach has been chosen for the k- $\epsilon$  class of models because the  $\epsilon$  equation cannot be integrated down to the wall and with EWT algebraic expressions are used in the near wall region instead (FLUENT™, 2013). Normally with the wall function approach the solution deteriorates under mesh refinement at the wall surface, however, FLUENT™ (2013) has taken steps in ensuring that mesh refinement is possible without deterioration. The main requirement thus becomes ensuring that there are enough nodes to fully resolve the boundary to obtain adequate near wall accuracy (FLUENT™, 2013). These meshing requirements allowed the same mesh to be used for all simulations without issue of incorrect wall treatments. Once the turbulence model and associated wall treatment was set the boundary conditions had to be specified.

#### 4.3.3 *Boundary conditions*

At the inlet of the domain a ‘velocity-inlet’ was specified in which the user has to specify the velocity and turbulence quantities as well as supersonic/gauge pressure, however, the pressure is only applicable to supersonic flows. This boundary condition is a Dirichlet type of boundary conditions in which the value of the quantity is specified and fixed, i.e., velocity. The outlet was specified as a ‘pressure-outlet’ which, similarly to the inlet condition, has a fixed pressure for sub-sonic flows at the boundary nodes. The floor surface was named separately as ‘wall\_floor’ as FLUENT™ would immediately recognise this as a ‘wall’ boundary. This applies a no-slip condition at the wall nodes thus creating a zero fluid velocity relative to the wall surface at the wall surface. This type of boundary was also applied to the entire flat plate geometry. The remaining surfaces were set to ‘symmetry’ boundary conditions which impose a zero normal gradient at the surface.

#### 4.3.4 Reference values

The next step was to set the reference values used in the calculation of variables such as the drag and lift coefficients for the flat plate. Of concern in this section were the area, length and density as these directly affect the calculation of lift and drag coefficients. The reference area and length was changed to the area and chord length of the plate respectively, whilst the density was left as its default value due to this value being the same as air.

#### 4.3.5 Solution methods

Solution methods and controls were the next options to be setup before proceeding. With regards to the solution methods; the solver scheme and spatial and temporal discretisation had to be set. For the solution method the SIMPLE algorithm, which is a segregated solver, was used. A segregated scheme was chosen as it has proven, in past experience, to converge more easily than the coupled scheme although at a slower rate. The SIMPLE scheme was also chosen over the SIMPLEC and PISO schemes as there are fewer requirements to ensure accurate and convergent solutions for complex flow with the only cost essentially being the time to convergence (FLUENT™, 2013).

The calculation of the gradient terms in space had to then be set and was left as the default ‘Least Squares Cell Based’. This scheme assumes the solution varies linearly in the domain and calculates the gradient of terms at the cell centre. This method is equivalent in accuracy to the ‘Green-Gauss Node Based’ method offered in FLUENT™, however, comes at a lower computational cost and is also superior to the ‘Green-Gauss Cell Based’ formulation that is offered (FLUENT™, 2013). The standard pressure discretisation was used as this is acceptable for most types of flows as well as initial convergence issues experienced with other discretisation schemes (FLUENT™, 2013).

For the remainder of the equations involved, i.e., the momentum, TKE and,  $\varepsilon$  or  $\omega$  equations, ‘Second Order Upwind’ discretisation was used. The upwind method calculates nodal values based on nodal values and coefficients of two upwind cells and one downstream cell where the coefficients for convection are based on cell size, fluid density, velocity and fluid viscosity (Versteeg and Malasekera, 2007). With the first-order accurate scheme, the cell centred value is assumed to hold throughout the cell and hence the cell faces and centre values are the same. The second order scheme improves accuracy on the cell faces by using a Taylor series expansion about the cell centre, using the gradient based on the upstream cell. This provides second order accuracy and FLUENT™ (2013) achieves this using the equation:

$$\phi_{f,sou} = \phi_{u,c} + \nabla\phi \cdot \vec{r} \quad (4-1)$$

which, for a perfectly Cartesian mesh, shows that face values will depend only on a single gradient component and displacement. Increased accuracy can be obtained with higher order schemes, such as QUICK or MUSCL, however, convergence is often harder to achieve with these schemes and the improvements in accuracy are generally not significant (FLUENT™, 2013).

The last term to be specified was temporal discretisation when the simulation was switched to transient. In this case ‘First Order Implicit’ discretisation was chosen as the implicit formulation is unconditionally stable with respect to time step size in comparison to the explicit formulation (FLUENT™, 2013). In the implicit formulation the variables are predicted at a future time step using values at the current time step (Versteeg and Malasekera, 2007).

In controlling the solution, the under-relaxation factors had to then be set, which applied to both steady and transient simulations. These are essentially a means to ensure that the solution change is limited enough to ensure convergence. This is illustrated by considering that between iterations, a variable is dependent on its value from the previous iteration and changes in the following way:

$$\phi = \phi_{old} + \alpha\Delta\phi \quad (4-2)$$

which shows that the under-relaxation factor,  $\alpha$ , can be made small to ensure that the solution does not cause too large a change between iterations. These values were reduced in the setup stage to ensure that the between iterations the solution would not be changed beyond a converged state. Alternatively for very simple flows this can even be increased to reduce solution times.

#### 4.3.6 Solution monitoring

The next step in the solution process was to create the appropriate monitors to judge convergence as well as for analysis post-simulation. The monitors created were a lift and drag monitor which reported, plotted and wrote to file every iteration for the steady state simulations and every time step for the transient simulations. The same was done for a vertical velocity monitor which was put in place at the location described by Matty (1979). This monitor allowed the measurement of fluctuating velocities in the wake of the plate thus providing an indication of the shedding frequencies obtained through simulation.

#### 4.3.7 Initialisation

The final steps in simulation setup included the solution initialisation and setting the program to automatically save at regular intervals in the event of a system crash. The solution was initialised using FLUENT™’s ‘Hybrid Initialization’ which essentially solves a simplified set of equations to produce an initial velocity and field which conforms to complex geometry domains and smoothly connects high and low pressure areas (FLUENT™, 2013). The solution was then initially run as steady state before switching to transient, with a time step chosen to split one oscillation in Matty (1979) into 72 parts such that a smooth velocity curve would be produced.

### 4.4 Simulation and literature results comparison

At the onset of the flat plate simulations the results that were sought after were the drag coefficients for the orientations simulated, as well as the frequency of any predicted vortex shedding. Through the simulation process additional results appeared which aided in

determining the appropriateness of each turbulence model. These results and possible causes and implications will be presented further in this section.

#### 4.4.1 Mesh independence

Before presenting and discussing the results obtained the mesh independency of these solutions needs to be shown. The mesh independency was checked within the limits of the computing power available in terms of turnover time and mesh size. Three meshes were used in testing the mesh independence of the problem, with the coarse and fine meshes already shown in Figure 4-6. All three meshes were, however, only used for a single turbulence model as will be discussed further. The third mesh generated consisted of approximately 4 450 000 cells and was created by enhancing the mesh in the wake region of the flat plate. The finest mesh used in checking grid independence can be seen in Figure 4-8, which includes a detailed view of the upstream section of the heliostat to provide an idea of the growth rate of the cells when using this meshing method.

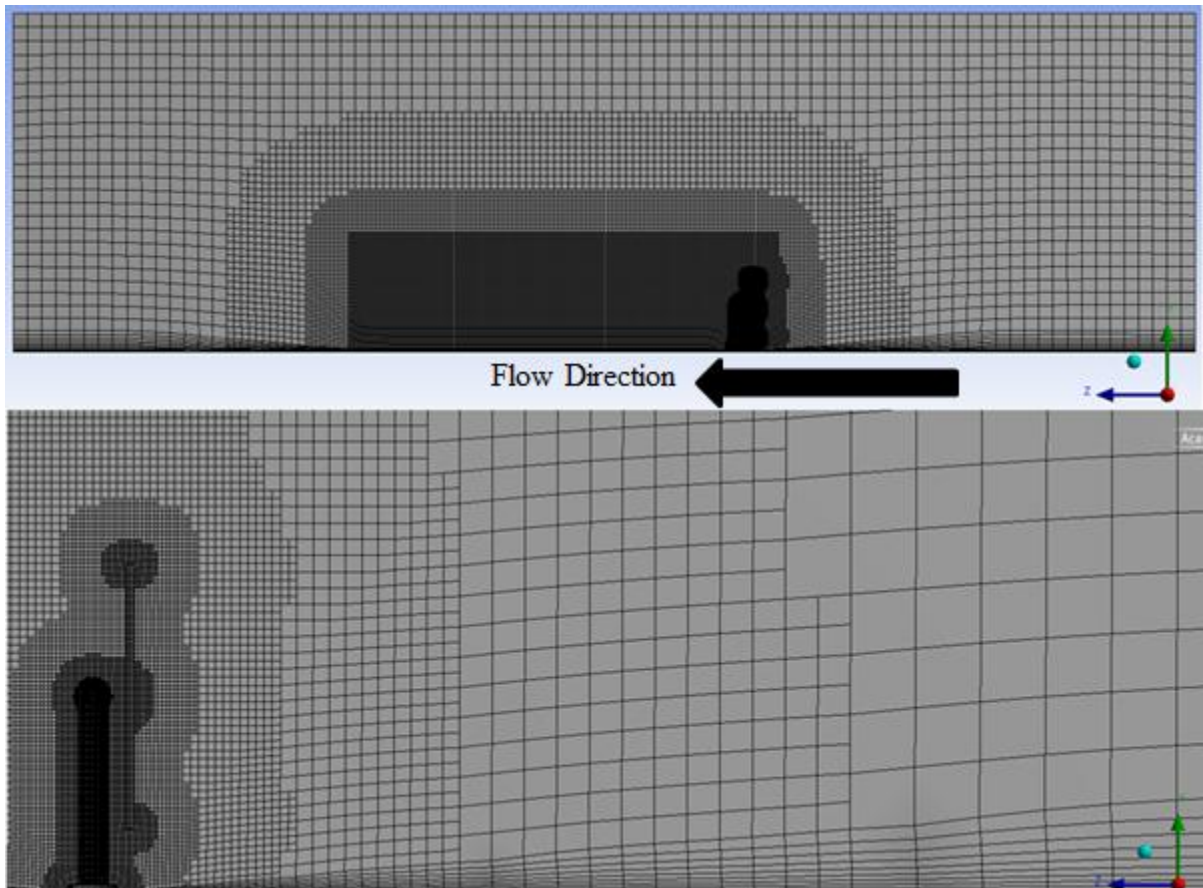


Figure 4-8: Finest mesh used in simulation with detailed view (bottom)

When simulations were run first with the coarse and the fine mesh, as shown in Figure 4-6, the only noticeable difference between results for the Realisable  $k-\epsilon$  model was the drag coefficient. Between the meshes, this turbulence model showed much the same velocity fluctuation behaviour, however, the SST  $k-\omega$  model showed significant changes in the monitored velocity alongside slight changes in the drag coefficient. The large differences can likely be attributed to the blending functions, which contain sensitivities to the distance a cell

is from the wall. By refining the mesh in the wake of the plate, the blending functions may change the transition point in the wake of the flow thus changing the nature of the velocity fluctuations created in the simulation. Due to the drag coefficient values found at the fine mesh for the Realisable k- $\epsilon$  model being quite accurate, as well as the lack of significant change in the velocity fluctuations measured between the meshes, this model was not tested on finer meshes. The manageable turnover time for the fine mesh also contributed to the decision to use this mesh for the simulations.

With regards to the RNG k- $\epsilon$  model, slight differences were found between the coarse and fine mesh both for the velocity fluctuations in the wake and drag coefficients predicted. This was, however, only found for the ground mounted plate whereas for the plate with a gap the only noticeable difference found between meshes was the drag coefficient predicted. This combined with the drag prediction error of less than 3 % for the fine mesh, with an improvement of around only 6 % from the coarse to the fine mesh, the fine mesh was deemed accurate enough for the CFD whilst maintaining reasonable simulation time.

Back to the SST k- $\omega$  model; due to the large differences in velocity fluctuations between the coarse and fine meshes, an even finer mesh had to be used to check how close the solution was to being mesh independent. When the finest mesh was used, shown in Figure 4-8, the velocity fluctuations were found to change yet again, with the magnitude of these fluctuations decreasing significantly for the ground mounted plate. Without information about the actual magnitude of these fluctuations given by Matty (1979) the frequency of these fluctuations determined the accuracy of the results. When comparing the results from the fine to the finest mesh, a decrease of around 10 Hz was predicted for the ground mounted flat plate which resulted in a frequency closer to that obtained by Matty (1979). For the case with a gap between the plate and floor, the frequency of fluctuation was found to increase by around 7 Hz, bringing the simulated value closer to that found by Matty (1979). In terms of the drag coefficient, however, an improvement of around only 0.88 % was realised with the finest mesh. Considering the only slight improvement for drag prediction and noting that the load coefficients are the main focus of this thesis, and not the flow field, the fine mesh has been chosen to represent the results. This is especially so due to the hugely increased simulation time incurred when using the finest mesh which was not a viable option for the improvement of the results. Note that for all models tested, the load coefficient was approaching a set value in a monotonic manner.

#### 4.4.2 Drag coefficients

Investigating the drag coefficients predicted by the simulations provided a quantitative means of evaluating the accuracy of the simulations conducted. The drag coefficient for a flat plate perpendicular to the flow obtained by Fail *et al.* (1959) has been used as the benchmark result for the simulations. The drag coefficients reported have been averaged over recorded values for the transient simulations in order to get a value comparable to that of Fail *et al.* (1959). The results of the simulations can be seen in Table 4-1.

Table 4-1: Drag coefficients

	Realisable k- $\epsilon$	RNG k- $\epsilon$	SST k- $\omega$
Simulation	1.13	1.11	1.17
Experimental*	1.14	1.14	1.14
Error	0.87 %	2.63 %	2.63 %

\*Fail *et al.* (1959)

The results obtained would indicate that the Realisable k- $\epsilon$  model provides the most accurate result for this flow type as the error between the simulated and experimental results are less than 1 %. The other turbulence models reveal slightly less accurate results with an error of 2.63 %, which in itself is still quite accurate. When investigating the literature of Fail *et al.* (1959) it was found that, based on comparison of measured and integrated drag coefficients, a difference of only 0.9 % (coefficients of 1.12 and 1.13) was found which would indicate highly accurate experimental data. This indicates the viability of CFD for this type of simulation considering how well the drag coefficients are predicted. This is encouraging as the geometry simulated involves many issues which turbulence modelling has not yet fully resolved, which have been mentioned in section 3.5. Such challenges include strongly separated flow, impingement and vortex shedding. Results concerning such transient features will be discussed further on.

Looking at the results obtained, it can be said that any of the three turbulence models tested would be sufficient in providing an estimate of the drag coefficient on the heliostat like geometry tested. This is, however, only true if the only result of concern is the loading coefficients and other information about the flow field is irrelevant. This will be illustrated later as the result of transient flow features is discussed. Regarding the load coefficients; from a design perspective the SST k- $\omega$  would be the most appropriate as it slightly over-predicts the drag compared to the other models which would result in the safest heliostat design.

#### 4.4.3 Velocity fluctuations

Considering the impressive performance of the three turbulence models in predicting the drag coefficient on the flat plate geometry; further data is required to determine the most appropriate of these models for simulation of such a case. This comes in the form of velocity fluctuations in the wake of the plate as the frequency of these fluctuations have been reported by Matty (1979), and thus allowed for further validation of the results. The frequencies predicted through simulation have been compared to that of Matty (1979) in Table 4-2.

Table 4-2: Simulated and experimental velocity fluctuation frequencies

	Realisable k- $\epsilon$	RNG k- $\epsilon$	SST k- $\omega$	Matty (1979)
Ground mounted	0 Hz	30.91 Hz	41.24 Hz	25 Hz
Plate with a gap to chord ratio of 1/4	0 Hz	0 Hz	17.85 Hz	31.44 Hz

The most notable result seen in Table 4-2 is the fact that the Realisable k- $\epsilon$  model does not predict any transient behaviour for the problem. Also of importance is that the RNG k- $\epsilon$  model only predicts velocity fluctuations for the ground mounted case. This shows that for the task of predicting the full transient behaviour of this problem, the SST k- $\omega$  would prove the best from the models tested. It is then, however, surprising that the RNG k- $\epsilon$  model results in the most accurate prediction of velocity fluctuations for the ground mounted flat plate. This could be the result of the RNG model having modifications which account for rapidly strained flows, thus providing better results in the ground mounted case, however, for the case with a gap between the floor and the plate there is a fourth edge at which separation occurs. This is associated with large strain rates which, in accordance with the Boussinesq hypothesis, create greater turbulence shear stresses which are transported into the wake. The increased turbulence increases the mixing of the flow and is known to reduce, and seemingly in this case, suppress transient features of the flow. The SST model, however, likely achieves more accurate prediction of the strain rates near the wall surface as it is designed to take into account the transport of turbulent shear stress.

The issue regarding no prediction of transient features with the Realisable model could result from this model only containing a variable turbulence viscosity coefficient,  $C_\mu$ , which ensures the realisability of the model. This simply ensures always positive normal Reynolds stresses but it could be the case that for such a bluff body flow, the value of  $C_\mu$  is still predicted as large, creating a more diffusive flow thus damping out velocity fluctuations and transient features.

It can thus be said that if an overall picture of the flow features is required along with a fairly accurate drag prediction, the SST k- $\omega$  model would prove the best for this type of problem. This is due to its ability to predict transient features for the flat plate geometry where the other tested models have failed. It also does predict the drag coefficient within 5 %. It should also be noted that whilst the frequency of the predictions were not particularly accurate, the finest mesh tested did improve on the reported results. This, however, came at the cost of unacceptable convergence times due to the limit of computational resources at this time and it is important to recognise that with greater computational power and finer meshes higher accuracy can be attained in prediction of transient flow quantities for a flow problem of this type. At this point in time, however, the reported results are at the limit of what can be achieved with the resources available for the flow over a flat plate.

Whilst the SST k- $\omega$  may prove best for full transient flow field analysis, the only data reported by Peterka and associates in their studies was the various loading coefficients on the heliostats. Considering the loading coefficients are the focus of this thesis, the Realisable k- $\epsilon$  model would in fact be the most suitable when analysing the actual heliostat geometry. This is due to its greater accuracy in predicting the drag coefficient for the flat plate geometry whilst not predicting the transient behaviour of the other models. This would mean simulations could be run in steady state thus greatly reducing the simulation time whilst ensuring accurate prediction of the load coefficients. Future work in this field could involve

generating experimental data for a heliostat geometry against which all these models can be compared, as well as possible LES simulations if the computational resources are available.

#### 4.4.4 Qualitative results

Considering the differences found between the turbulence models in the previous results, a look into the flow features predicted by these models would provide some further insight. A look at the iso-surface of Q-criterion has been checked for these models as this provides information about the vortex core regions predicted by each model. The Q-criterion is used to visualise two or three-dimensional turbulent fields and is defined as (Piomelli, 2006):

$$Q = -\frac{1}{2}(S_{ij}S_{ij} - \Omega_{ij}\Omega_{ij}) \quad (4-3)$$

If the Q-criterion is positive then it represents a region in which the rotation is dominant such as a vortex. In the case of comparing results for the flat plate flow studied, the value of  $Q$  was chosen such that the vortex cores in the wake of the plate could be visualised. To do this within ANSYS's post-processing application, the level of Q-criterion was set to 0.0025. This is essentially a percentage of the max  $Q$  in the domain and this percentage was kept constant across all models. Comparisons for the ground mounted plate can be seen in Figure 4-9, where the RNG model proved to be the most accurate. Note that this is just a frame in time as the simulations were transient with this affecting some features of the presented results, such as the shape of the iso-surface and position of vortices in the wake.

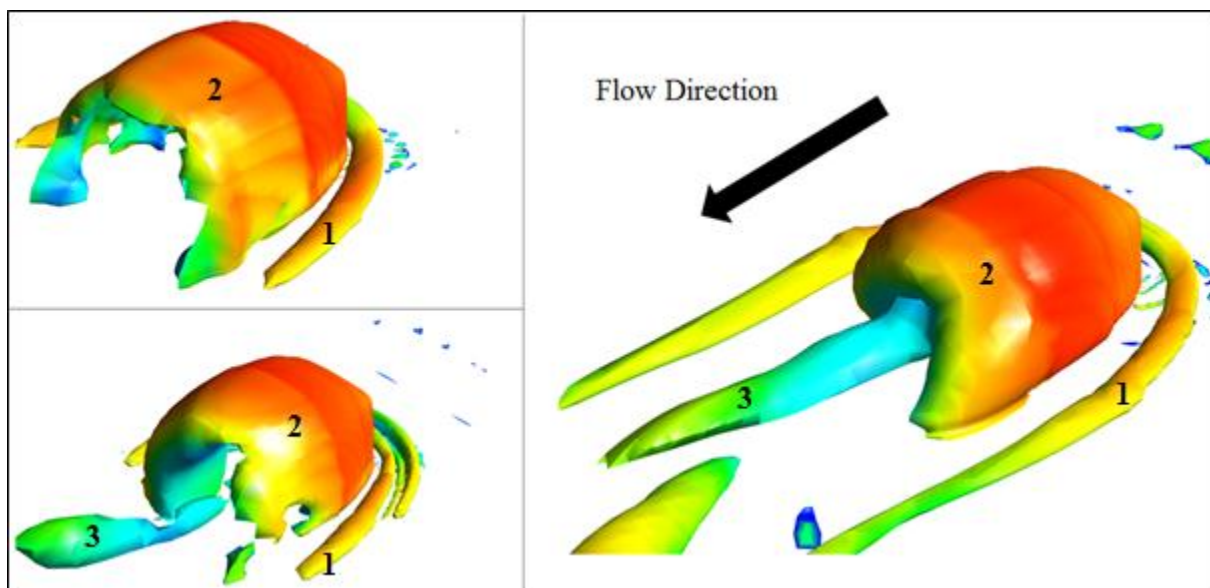


Figure 4-9: Comparison of Q-criterion level 0.0025 for Realisable (top left), SST (bottom left) and RNG (right) models for a ground mounted flat plate, coloured by velocity magnitude

Looking at Figure 4-9 one of the common features seen for all three models is the formation of a vortex at the lower, frontal edge of the heliostat which extends around both the left and right edges in the flow direction (feature 1 in the Figure 4-9). For the SST  $k-\omega$  model, however, a second frontal vortex, which does not extend as far back as feature 1, is also

formed. The RNG  $k-\epsilon$  model is also shown to predict feature 1 to extend much further back than either other model tested. A second common flow feature is a large horseshoe shaped vortex in the wake of the plate characterised by feature 2. For the Realisable  $k-\epsilon$  model this feature is symmetric compared to the other two models which predict this feature as asymmetric at some arbitrary point in time. This is representative of the transient nature of the problem as this asymmetry is constantly reversing in its shape as time progresses in the simulation. The iso-surface has been captured for a few different points in time in Appendix B: Iso-surfaces at Different Time Steps for the RNG and SST models to illustrate the transient nature of the problem. The symmetry produced by the Realisable  $k-\epsilon$  model is expected when considering the simulation does not predict transient results. This being due to the symmetry of the geometry about its mid plane and an unchanging simulated flow field, hence symmetrical unchanging flow features.

From Figure 4-9 the flow features predicted are more complex for the SST  $k-\omega$  and RNG  $k-\epsilon$  model as can be seen from feature 3. This trailing vortex alternates its position, much like feature 1, for both these models, however, with the RNG  $k-\epsilon$  model a detached vortex further downstream of feature 3 can be seen. This is evident of vortex shedding, which was predicted by Matty (1979) which is also expected as the RNG  $k-\epsilon$  did prove to be the most accurate in predicting the velocity fluctuations for the ground mounted plate. Clearer illustration of the complexity of the flow field in the wake of the plate can be seen from examination of the streamlines produced from the various models. These streamlines, shown from the bottom view, can be seen in Figure 4-10.

From Figure 4-10, the symmetrical flow predicted from the Realisable  $k-\epsilon$  model can be clearly seen, as well as part of the horseshoe vortex that appears in the wake. The SST  $k-\omega$  model shows a highly asymmetrical flow field, with a strong vortex to the left of the image at this point in time, which is expected as this feature would alternate from left to right due to the transient nature of the problem. The RNG  $k-\epsilon$  model also shows an asymmetric flow field in Figure 4-10, however, the presence of the vortex is not as clearly illustrated as with the SST  $k-\omega$  model. This simply shows that the streamlines need to be considered in conjunction with the iso-surfaces when analysing the flow features. For these particular simulations investigation of the streamlines proved most useful in comparing differences between the flow fields predicted by the various turbulence models.

An outcome of investigating such results is that the most complex flow field predicted by the turbulence models used is linked to the most accurate results for this type of flow. It can also be said that for a relatively simple geometry (a vertical flat plate) the associated flow features are highly complex. This is important to note as the limits of two equation RANS modelling in CFD may be reached by even studying such a simple geometry.

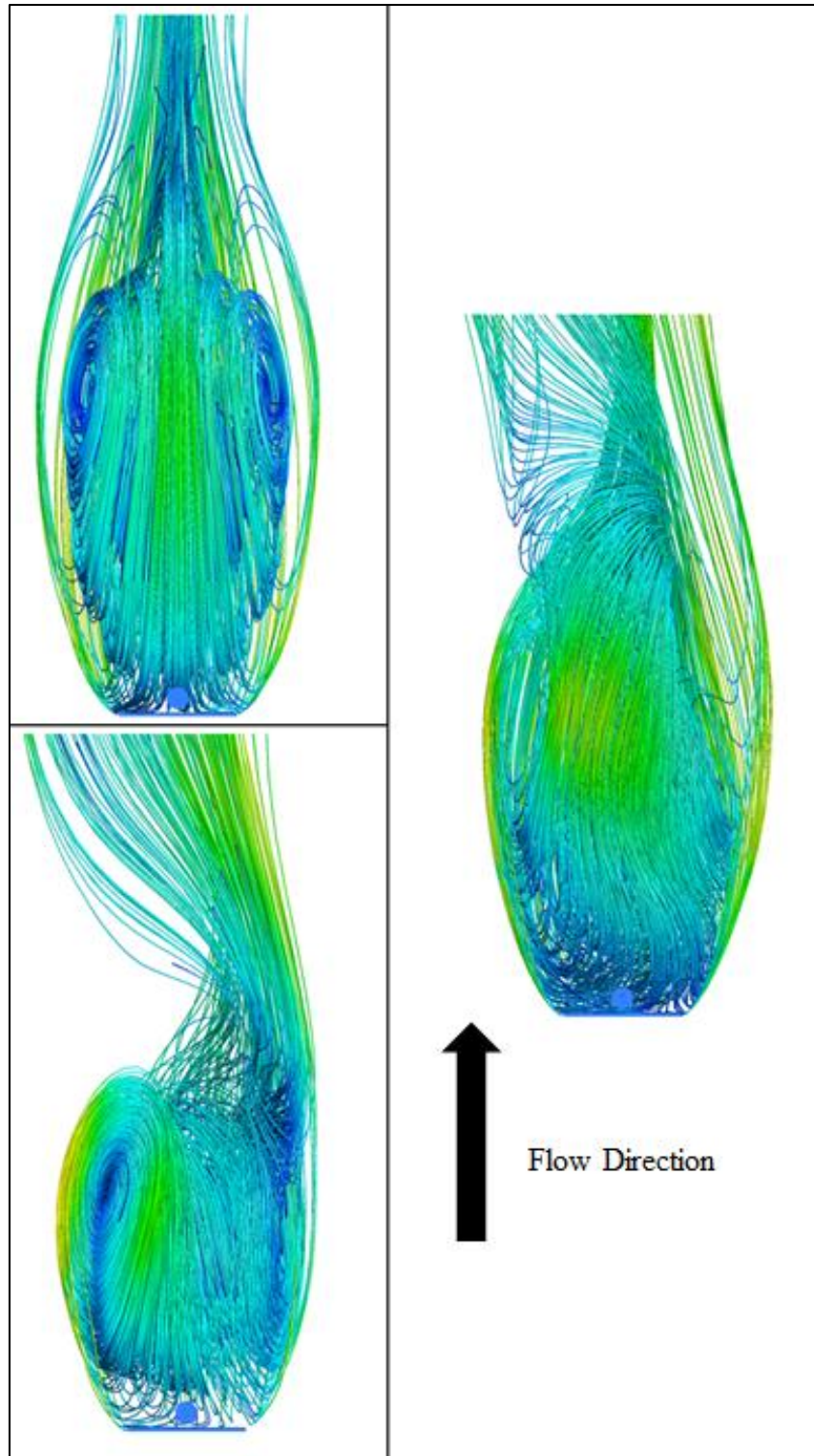


Figure 4-10: Streamlines in the wake of a ground mounted flat plate for the Realisable (top left), SST (bottom left) and RNG (right) models from the bottom view

Looking into the results for a plate with a ground gap, similarities can be found between the three turbulence models as well as similarities to the ground mounted plate results. Feature 1 in Figure 4-11 is similar to feature 1 in Figure 4-9, however, the iso-surface is thinner in comparison representing a weaker rotation of the vortex. For the ground gap plate feature 1

also extends into the wake from the bottom edge of the plate which shows that a greater degree of turbulence is entrained into the wake which is likely the cause for the weaker vortex. Further inspection of Figure 4-11 reveals that the SST  $k-\omega$  model predicts the most complex flow field, as shown by feature 2, representing a more complex vortex pattern in the wake of the plate. This prediction of a more complex flow field again shows, as with the ground mounted plate, a correlation with more accurate results as the SST  $k-\omega$  model did predict the most accurate transient results for this case.

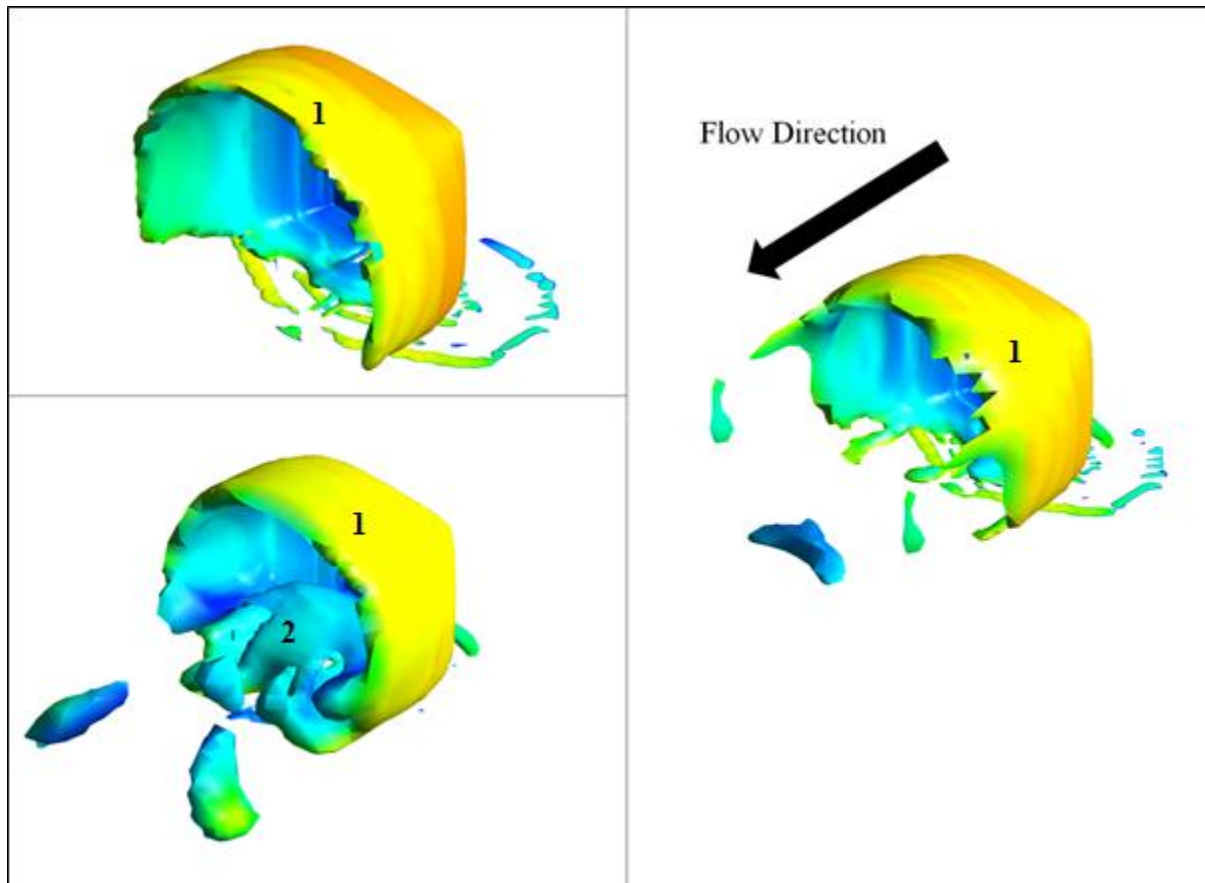


Figure 4-11: Comparison of Q-criterion level 0.0025 for Realisable (top left), SST (bottom left) and RNG (right) models for a flat plate with a ground gap, coloured by velocity magnitude

#### 4.5 Model selection

When moving forward onto the simulations for flow over heliostats, complete analysis including factors such as mesh independence studies and the strong possibility of transient simulations using all three turbulence models for a variety of heliostat designs was not viable in the time available due to computational limitations. It is also important to note that the available data used for validation from the various works of Peterka only contains average load and moment data. This meant that any transient heliostat simulations could not be properly validated thus making them unnecessary and the time required for such simulations would be largely wasted. These factors mean that whilst the SST  $k-\omega$  model may appear on

the surface as being the best model moving forward for heliostat simulations, the Realisable  $k$ - $\epsilon$  model was actually chosen due to the fact that this model tended to dampen out the transient features of the flow and essentially ran as steady state. This selection was also further supported by the fact that the Realisable  $k$ - $\epsilon$  model was the most accurate in predicting the drag on the flat plate from all the models tested. All these factors led to the selection of the Realisable  $k$ - $\epsilon$  model for all subsequent heliostat simulations.

#### 4.6 Conclusion

From the simulations done on a flat plate perpendicular to the flow in the two orientations tested it can be concluded that the Realisable  $k$ - $\epsilon$  model performs the best in terms of load prediction, however, fails to predict and transient flow features for this type of flow. It can also be concluded that the SST  $k$ - $\omega$  performs the best for transient simulations as it is able to predict transient features for both orientations unlike the RNG  $k$ - $\epsilon$  model which only produced transient results for the ground mounted flat plate. Considering the Realisable  $k$ - $\epsilon$  model and its performance in predicting an accurate drag coefficient whilst producing a steady state result leading ultimately to reduced computational effort for good load prediction, this model was, however, chosen when moving on to the heliostat simulations.

## 5. Heliostat Simulations

At the conclusion of using the Realisable k- $\epsilon$  turbulence model for all simulations beyond that of the flat plate; simulations could be conducted on actual heliostat geometry both for flat and boundary layer velocity and turbulence profiles. These simulations would determine the accuracy of the Realisable k- $\epsilon$  model in predicting loadings on heliostats and details of the simulations and results are contained in this chapter.

### 5.1 Simulation and literature geometries

For this first study on heliostat CFD, the geometry used by Cermak and Peterka (1979) was recreated using Autodesk Inventor for use in the simulations. This geometry was chosen as Cermak and Peterka (1979) have report load and moment coefficients for this particular heliostat geometry at various orientations. The geometry used in the simulations was simplified compared to the model geometry due to the complexity around the hinge area as well as the insignificance of the gap between facets on the heliostat face (Wu *et al.*, 2010). The geometry used in the simulation can be seen next to the model geometry in Figure 5-1 with the dimensioned model geometry been shown in Appendix F: Dimensioned Geometry.

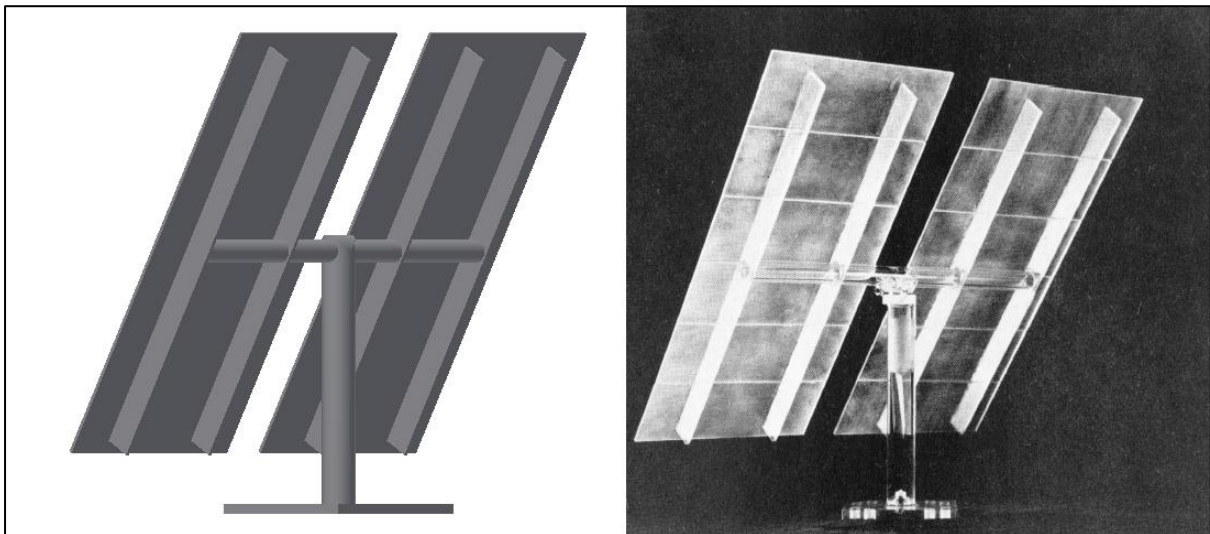


Figure 5-1: Geometry used in simulation (left) compared to model geometry (right), (Cermak and Peterka, 1979)

One of the major reasons the hinge section was simplified was due to this feature being small in comparison to the rest of the heliostat as well as causing issues with good quality meshes in the hinge region. The main issue was the creation of a stair-step mesh, which is essentially a ‘step’ from one layer of cells to the next, such as jumping from six to seven cells on the surface, with the gap being filled in with a triangular cell. For a two-dimensional geometry and example of a stair-step mesh can be seen in Figure 5-2. For the heliostat, the cause of the stair-step mesh was the close proximity of some components in the hinge. This creates the

inflation layers on the two surfaces close to each other and to avoid any overlap of the layers the stair-step mesh is created.

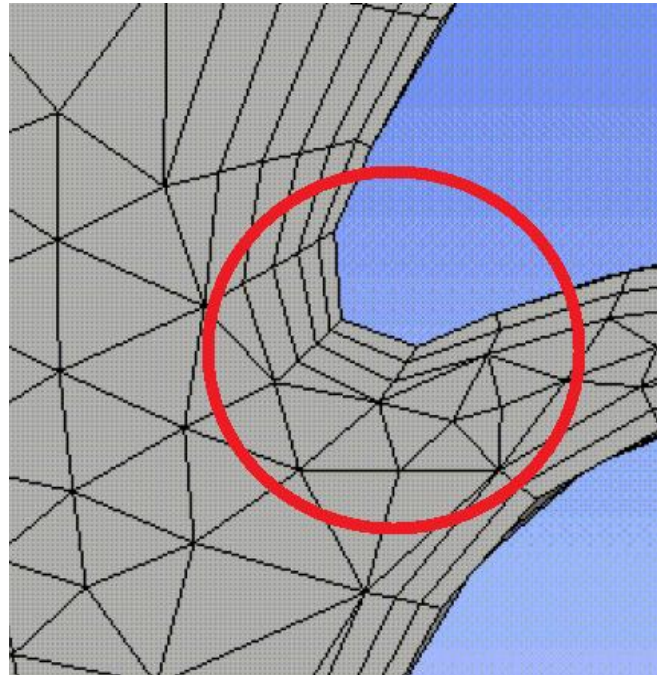


Figure 5-2: Detail of two-dimensional stair-step mesh

For the geometry used two orientations of the heliostat were of concern, namely, perpendicular to the flow and at an azimuthal and inclination angle of  $45^\circ$ , both of which are shown in Figure 5-3. The perpendicular case was chosen as this corresponds to the maximum drag load on the heliostat with the second orientation being chosen as it was expected to provide an interesting challenge to CFD considering the complex flow that would be expected from such an orientation for a bluff body.

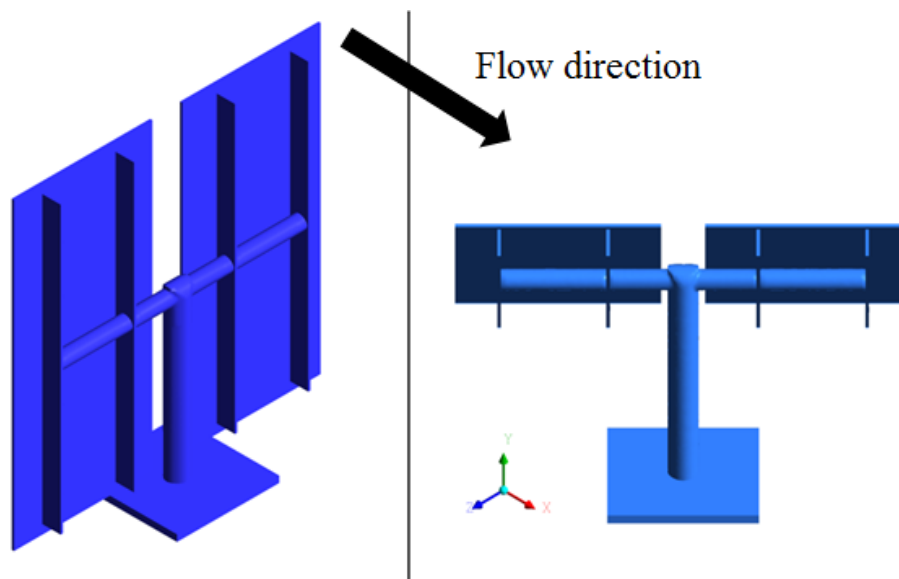


Figure 5-3: Perpendicular (left) and  $45^\circ$  tilted (right) orientations used in simulations

Once the heliostat geometry itself was created, the complete flow domain had to be defined similarly to flat plate simulations. This was done within the ANSYS workbench environment following the same procedure as that in section 4.1, with the domain extending approximately 2.3 m upstream of the heliostat with a total length of around 8.4 m. The total height of the domain was around 2 m and the width was 4 m. In this case the height and width of the domain was chosen based on a photograph of the experimental heliostat of Cermak and Peterka (1979) when in position in the test wind tunnel. This can be seen in Appendix A: Domain Width and Height, along with streamlines showing the validity of the chosen height and width. The location and size of the heliostat within the domain can be seen in Figure 5-4. Once the domain was created, it needed to be meshed and similar procedures as those used for the flat plate were followed in this regard.

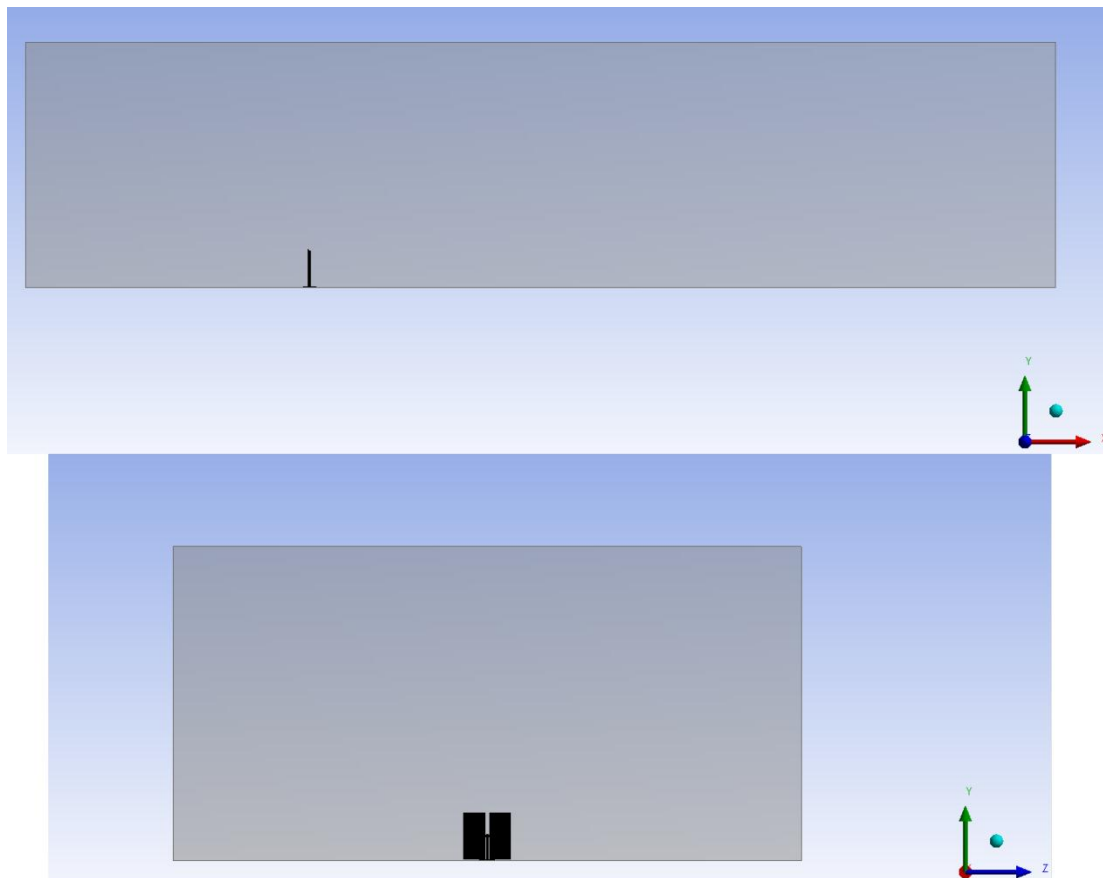


Figure 5-4: Location of heliostat within domain

## 5.2 Meshing methods

Considering the flat plate simulations were done in order to validate the models and parameters chosen for the heliostat simulations, the same meshing procedures were used wherever possible. As such, for the perpendicularly oriented heliostat a cutcell type mesh was used. Changes to the exact details of the mesh were made based on the change in dimensions and geometry from the flat plate to the heliostat and again, as with the flat plate, multiple meshes were generated in order to check the mesh independency of the solution. In this case,

three meshes of increasing density were generated with the cell count going from approximately 950 000 to 1 450 000 to 3 300 000. A comparison of these meshes can be seen in Figure 5-5.

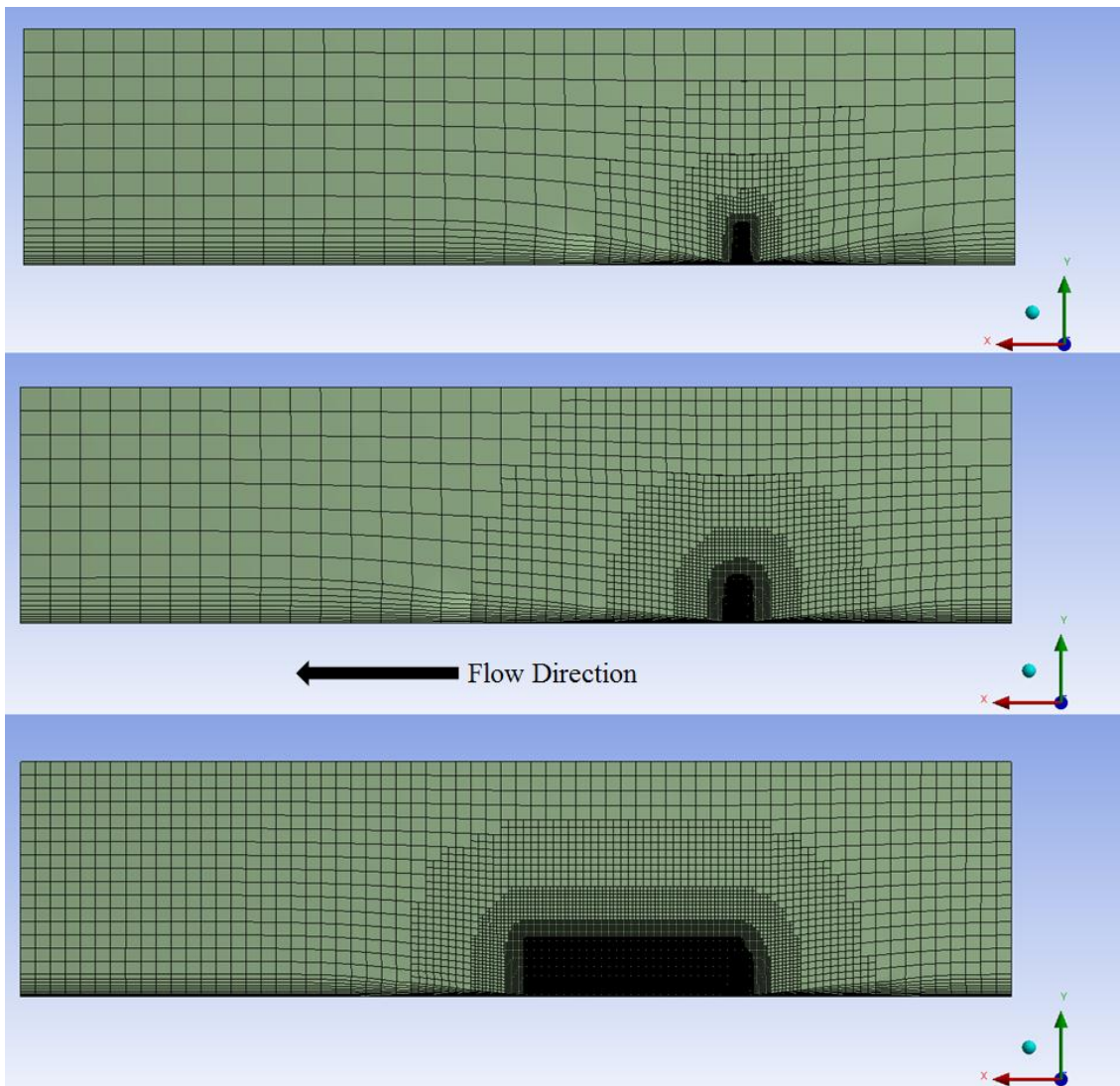


Figure 5-5: Coarse (top), fine (middle) and finest (bottom) meshes generated

For the second orientation with azimuthal and inclination angles of  $45^\circ$  the cutcell meshing had failed. This resulted due to the orientation of the heliostat surface cutting the cells at an awkward angle, creating bad quality cells resulting in a failed mesh. In order to work around this whilst keeping the cell count low yet provide a good quality mesh the domain was split into four zones which allowed different meshing procedures to be applied to each. The split domain can be seen in Figure 5-6.

Once the domain was split as shown, a tetrahedral mesh was applied to zone two which contains the heliostat. As mentioned in section 4.2 there are various disadvantages associated with a tetrahedral mesh with one of the ways to reduce their effects being using a finer mesh. Thus by splitting the domain a high density tetrahedral mesh could be applied in zone two which would ensure the integrity and accuracy of the solution in this zone.

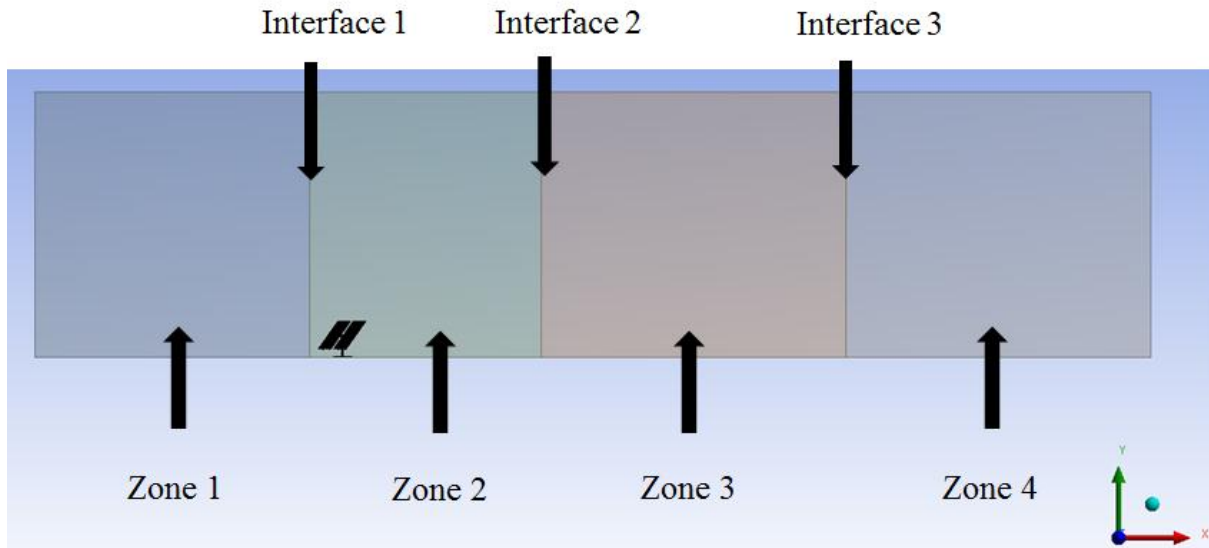


Figure 5-6: Split domain to allow different meshing procedures

Zones one and three were meshed by first creating a mapped face mesh at the interfaces one and two. This structured face mesh was then swept along the remainder of the zone resulting in a structured mesh within zones one and three which allowed the overall cell count to be kept low whilst ensuring an accurate solution. Another positive outcome of this method was that the mesh was kept conformal across interfaces one and two meaning that the cells at the interface share a common face and thus no averaging occurs across these interfaces.

Zone four was meshed slightly differently with it containing larger cells than that in zone three and was meshed entirely with hexahedral cells. This was done to, again, keep the overall cell count lower than if zone three extended to the end of the domain. When creating the mesh in zone four it was also ensured that interface three was created far enough downstream to ensure that the flow features would be less complex and smoother to reduce the effects of averaging across the non-conformal mesh interface.

Considering this was the first use of tetrahedral cells within this thesis, four separate meshes were generated to fully investigate the effects of mesh density on the solutions and to ensure a mesh independent result was achieved. The various density meshes used in this study can be seen in Figure 5-7. Note that a single project was used to generate the various meshes, which were then exported as .msh files as some issues were encountered within the ANSYS workflow. For this reason the meshes as seen in Figure 5-7 have been imported into ICEM CFD in order to be more easily viewed. The cell counts, in ascending order from coarse to finest mesh, were approximately 1 500 000, 2 000 000, 2 200 200 and 3 600 000 cells respectively.

As mentioned previously, in order to overcome the downfalls of tetrahedral meshes a high cell count had to be employed which was done in the region close to the heliostat, however, an alternative to this would be to use a polyhedral cell type mesh. These cells are made up of hexagonal faces and an example of a polyhedral mesh can be seen in Figure 5-8.

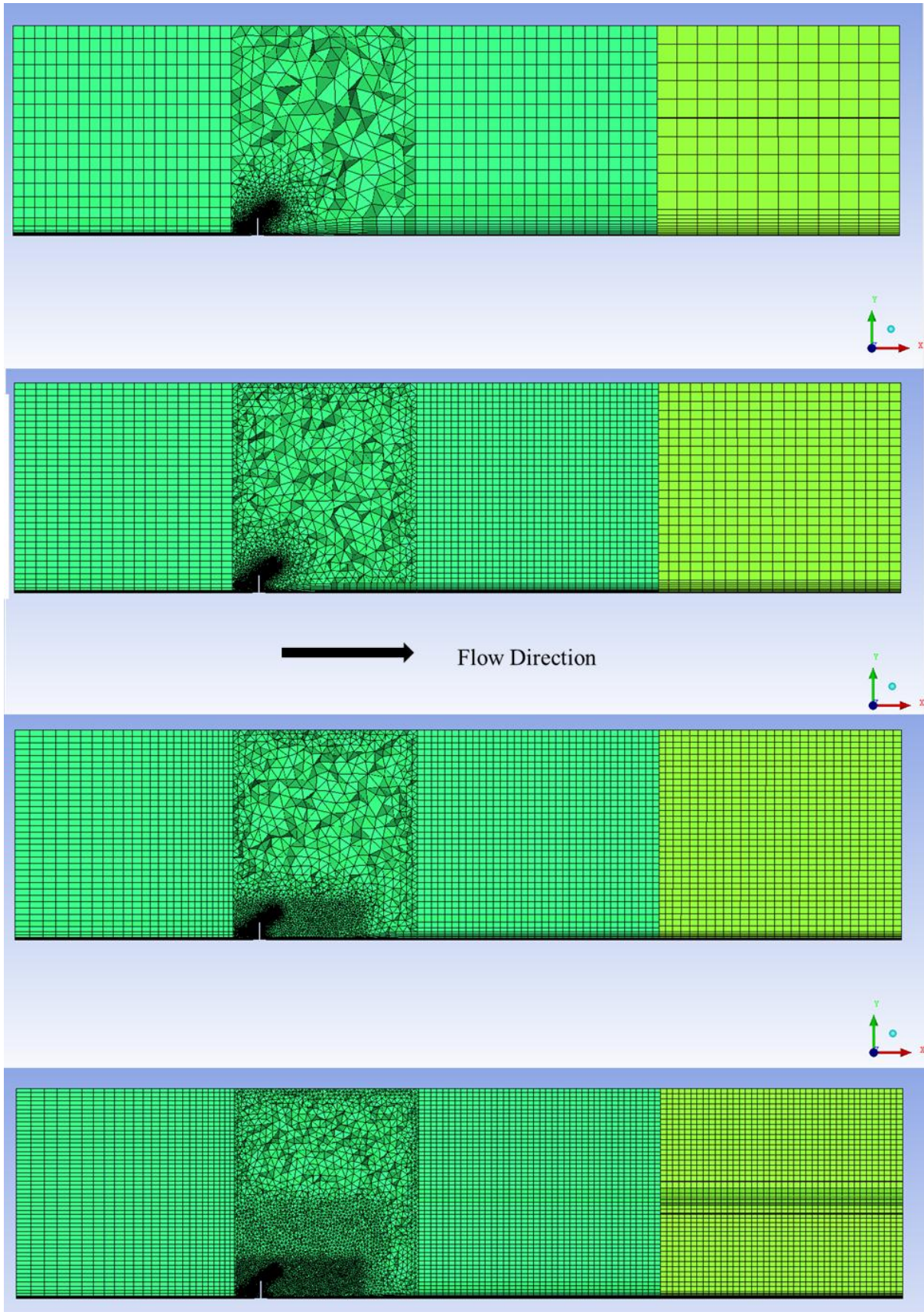


Figure 5-7: Coarse (top), medium (second from top), fine (second from bottom), finest (bottom) meshes generated

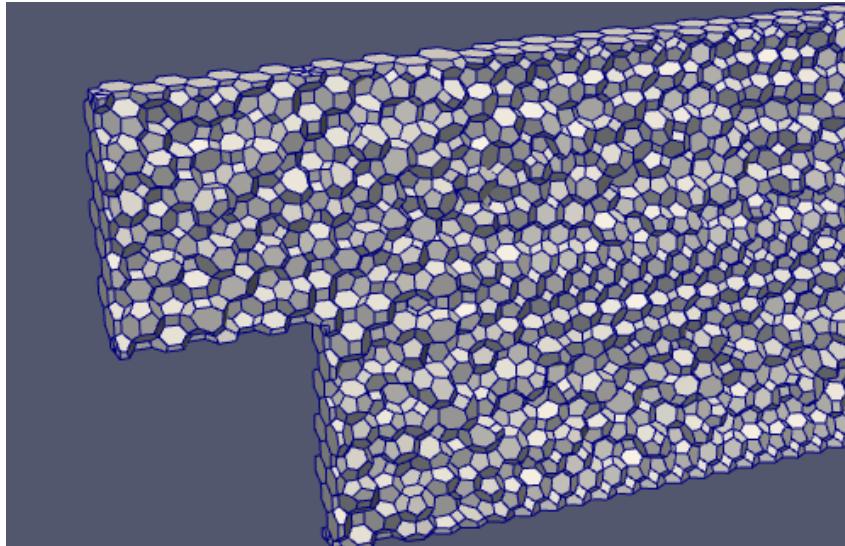


Figure 5-8: Polyhedral mesh example (Symscape, 2013)

Unfortunately this method of meshing is not inherently built into the ANSYS meshing application with the only way to obtain a polyhedral mesh being by converting an existing tetrahedral mesh within the FLUENT™ application. This had been done for the second orientation tested in order to investigate the effect of a polyhedral mesh on the solution, with the converted medium density tetrahedral mesh being shown in Figure 5-9. Note that the only method to view such a converted mesh is through FLUENT™ itself and unfortunately a clearer image of the mesh would have to be viewed within the program.

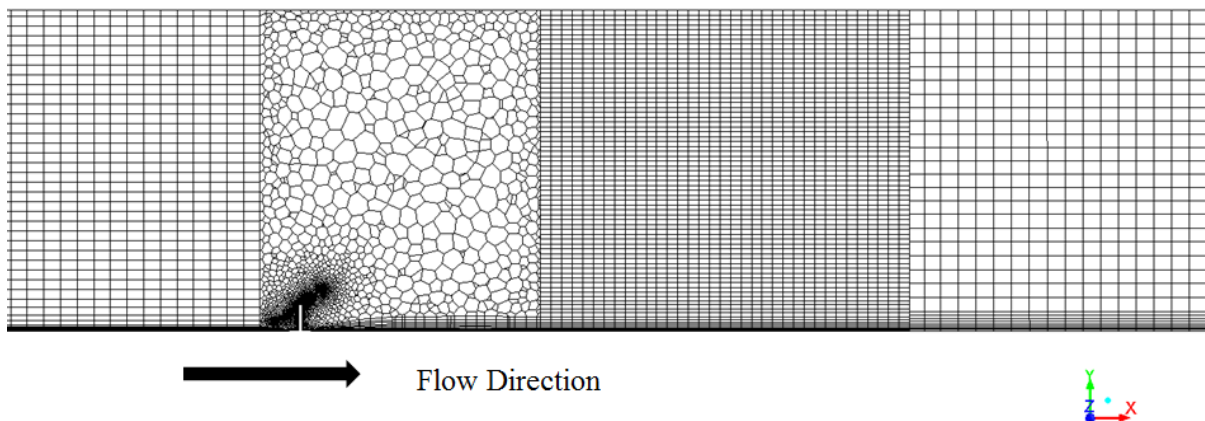


Figure 5-9: Converted polyhedral mesh

With regards to using polyhedral meshes within the ANSYS environment, one major issue that arises is the lack of direct control of the polyhedral mesh as it simply gets converted from a tetrahedral mesh. This resulted in the use of polyhedral meshes being undesirable for further simulations with such a complex geometry as a heliostat meaning that high density polyhedral meshes were used where applicable. Note that when investigating the effects of a polyhedral mesh, the medium and fine tetrahedral meshes were converted and used in the analysis. This was to provide a comparison to both the original tetrahedral mesh and a denser tetrahedral mesh. This investigation was also only conducted for flat velocity and turbulence

profiles due to the fact that the desired outcome was only a comparison to the results obtained using a tetrahedral mesh.

Before moving onto the setup, as before, the named selections were created within the ANSYS meshing utility with all of them being the same as for the flat plate in the case of the perpendicular heliostat. For the 45° tilted case, however, due to the meshing methods requiring the breakdown of the domain, an additional step was required. This involved first specifying that zones one to three were ‘one part’. This ensures that the mesh remains conformal across interfaces one and two and also allows FLUENT™ to know that flow is permitted through interfaces one and two. The two faces at ‘interface 3’, however, had to be given the name ‘interface-1’ and ‘interface-2’ in order to easily be defined as an interface within FLUENT™, which will be discussed further on. Beyond these additional steps, the next stage in the process was setting up the simulation.

### 5.3 Simulation settings

As mentioned, simulations were conducted using both flat and boundary layer velocity and turbulence profiles. For the simulations with flat profiles the upstream data was made to match that of Cermak and Peterka (1979) as this information had been reported by them. This was done by simply setting the velocity and turbulence intensity at the inlet to the same as the reported values.

Beyond changing the inlet conditions one other change that was made compared to the settings in section 4.3 was running the heliostat simulations as steady state instead of transient. This was done due to the criteria of selecting the Realisable model being that it produced a steady state result whilst reporting fairly accurate load coefficients for a heliostat like geometry.

As mentioned, interface 3 from Figure 5-6 had to be defined within FLUENT™ and this was done by creating a new interface and selecting the faces ‘interface-1’ and ‘interface-2’ to be the faces at which the interface would occur. The zone was then set to be a ‘matching’ interface as this was the most appropriate option for the interface type required. This option is used when both faces at the interface are aligned and allows fluid to pass through it. An example of where a matching interface would be used is shown in Figure 5-10.

When setting the flow conditions for the boundary layer simulations, only one change was made compared to that for the flat profile simulations. This involved creating TKE and velocity profile files which would be used at the inlet. The velocity profile was taken directly from Cermak and Peterka (1979) whilst the TKE had to be converted from their reported values of turbulence intensity. This was done using the relationship shown in equation (5-1).

$$k = \frac{2}{3}(UI)^2 \quad (5-1)$$

The TKE dissipation rate was, however, left as a constant flat profile at the inlet to ensure that the TKE profile would not dissipate into an undesired shape just upstream of the

heliostat. This resulted from initially experimenting with the dissipation rate prescribed within FLUENT™, given by  $\varepsilon = C_{\mu}^{\frac{3}{4}} \frac{k^{\frac{3}{2}}}{l}$ , and varying the turbulence length scale and noticing that the TKE would dissipate to highly inaccurate profiles just upstream of the heliostat. Complete modelling of the ABL would encompass an entire study on its own and hence this simple approach was taken to modelling the boundary profile from Cermak and Peterka (1979). These profiles were then made into a .prof type of file which could be directly read by FLUENT™ and applied at the inlet.

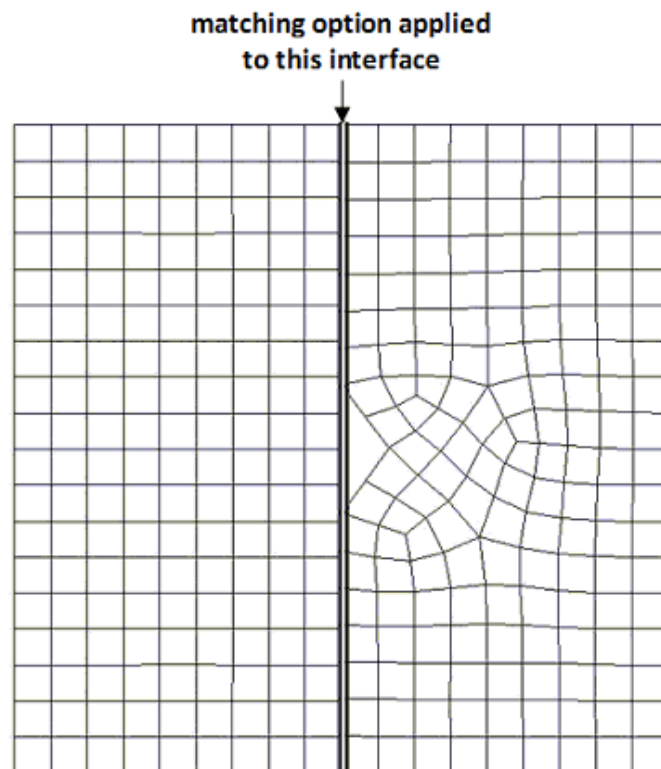


Figure 5-10: Application of matching type interface (FLUENT™, 2013)

Another change made during the setup process, for both the boundary layer and flat profile simulations, was to setup monitors for not only drag and lift coefficients, but also for moment coefficients to monitor moments mentioned in section 3.3. The velocity monitor downstream of the heliostat was also left in place in order to ensure that the selection of a steady state simulation was in fact correct by checking that the velocity did not fluctuate in the wake of the heliostat.

#### 5.4 CFD and literature results comparison

As with section 4.4, again, only results for the mesh independent case of each simulation will be reported, with an example of a mesh independency study for this case being presented in Appendix C: Mesh Independency Study for Heliostats. This had been judged, as previously,

based on either a zero change in results or a slight change for a large increase in mesh size and resources required. Note also that for all simulations conducted the results produced with the Realisable  $k-\epsilon$  were in fact steady state as expected, with this being established by monitoring no fluctuation for velocity at a point in the wake of the heliostat as well as no change in monitored load coefficients. From past experience, if a case were unsteady it would produce some fluctuations in such monitors even when run as steady state.

#### 5.4.1 Flat inlet profile

When looking at the results of the simulations, the first item of concern was how close the simulation conditions matched the conditions reported by Cermak and Peterka (1979). This was done by comparing the upstream velocity and turbulence profiles obtained from simulation (extracted 0.7 m upstream of the heliostat) to those given in Cermak and Peterka (1979). This was done for all orientations tested and for the different types of meshes, namely cutcell, tetrahedral and polyhedral meshes. The plots of the profiles found through CFD compared to experimental can be found in Figure 5-11.

From Figure 5-11 it can be seen that for the perpendicularly oriented heliostat, the velocity profile produced through CFD has a slight velocity deficit near the ground in comparison to the experimental profile produced by Cermak and Peterka (1979). For this particular orientation this would likely cause some error in the loading coefficients produced for this orientation through experimentation, which will be shown further on.

Looking at the profiles produced for the tilted heliostat, it can again be seen that there is still a slight velocity deficit near the ground. Again this could have an impact on the load coefficients produced through CFD for the heliostat. One last thing to notice when regarding the velocity profiles is that the polyhedral mesh and tetrahedral mesh produce near identical velocity profiles.

Next was to investigate the turbulence intensity profiles from CFD and compare them to the profile produced experimentally by Cermak and Peterka (1979). From Figure 5-11 it can be seen that the turbulence intensity profiles produced through CFD do in fact match up, on average, quite well with the profile from Cermak and Peterka (1979). Also, the profiles produced using a tetrahedral mesh and a polyhedral mesh are again found to be near identical.

Note that the profiles being compared were not normalised according to some height and velocity as the CFD was intended to reproduce the experimentally obtained results and conditions. Thus a direct comparison was conducted between CFD and experimentally obtained data reported in Cermak and Peterka (1979) and this was done for both the flat profiles and boundary layer profiles of the following section.

After comparing the profiles of Cermak and Peterka (1979) to those produced through CFD the load coefficients were investigated as these were the primary focus of this study. The comparison between load coefficients obtained through CFD and those reported in Cermak and Peterka (1979) can be found in Table 5-1.

It can be seen in Table 5-1 that certain load coefficients have been omitted and this was done due to the low magnitude of these coefficients for the orientations reported. This would mean that such coefficients would have been sensitive to any experimental issues and even measurement issues. The consequence of this would be that the results found through CFD for these coefficients could appear more inaccurate than they truly are and would give a false account of the usefulness of CFD in predicting loadings on heliostats. Also, considering the low magnitude of the omitted coefficients to those that were reported it can be said that for design purposes the reported coefficients would be of greater relevance.

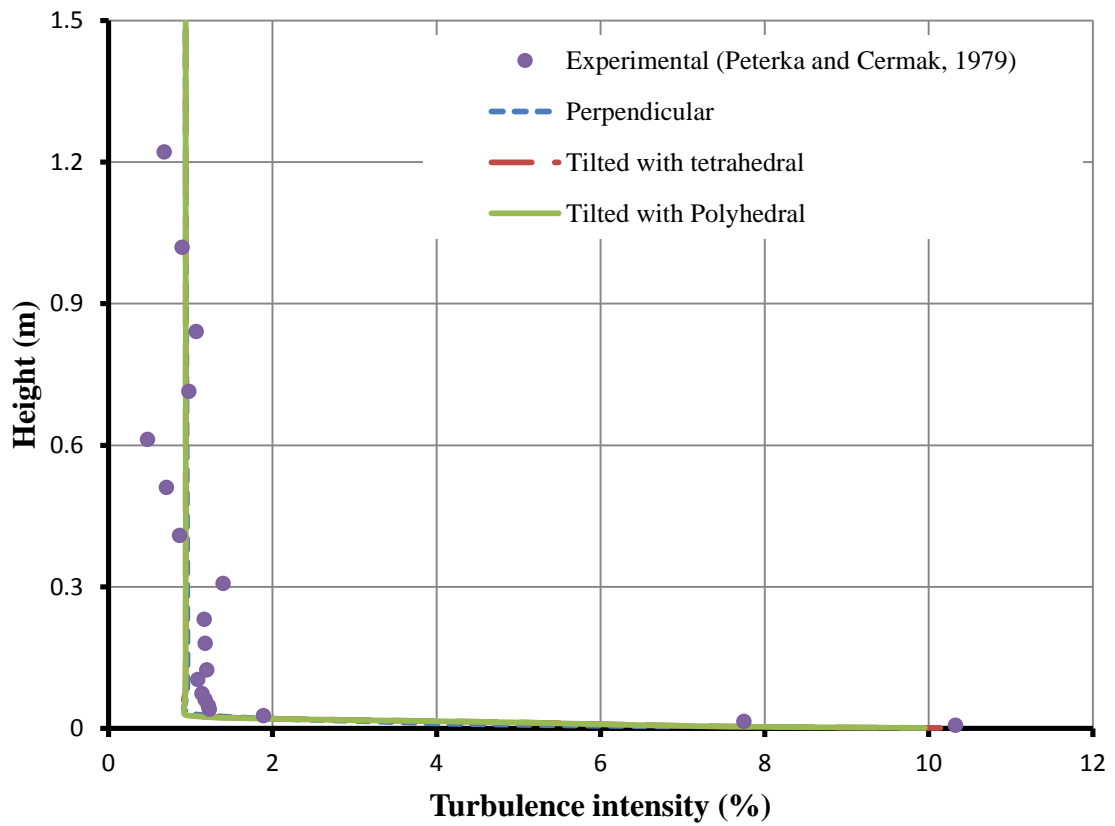
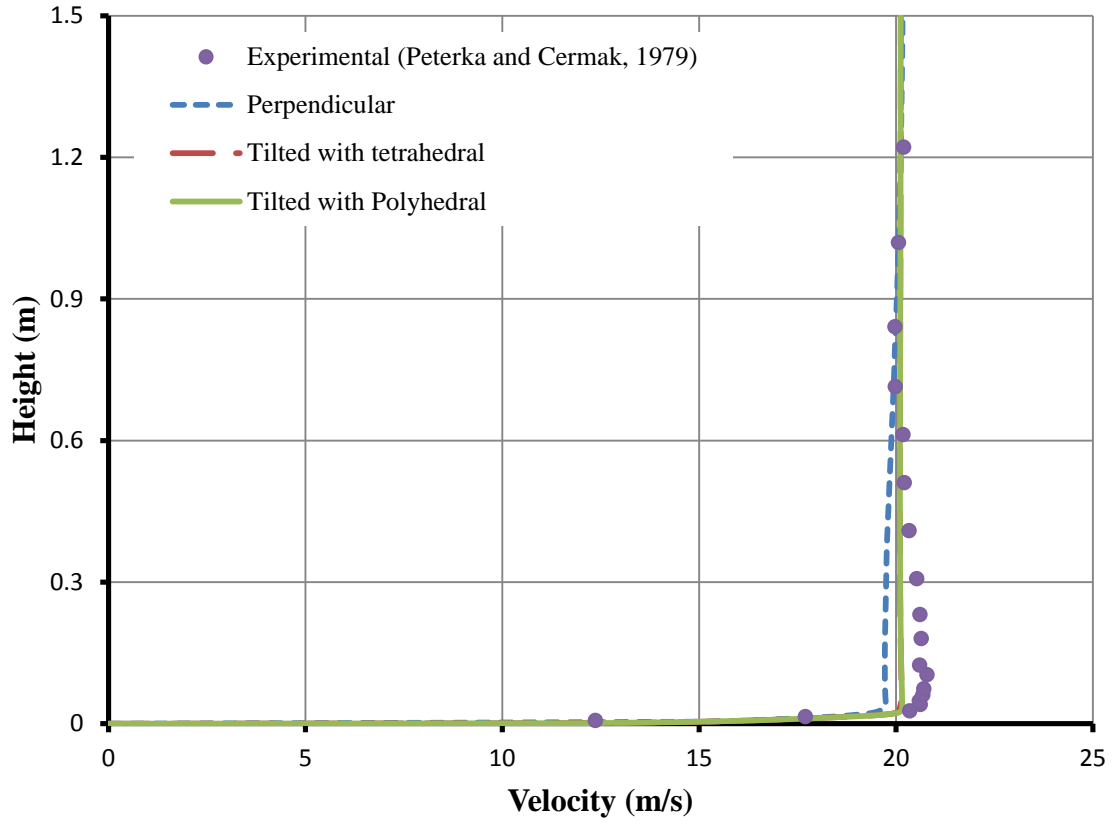


Figure 5-11: Comparison of flat velocity and turbulence profiles

Table 5-1: Load coefficients for flat inlet profiles

	Orientation	$C_{F_x}$ (Drag)	$C_{F_z}$ (Lift)	$C_{m_{y_{base}}}$ (Overturning moment about base)
CFD		1.265	-	-0.647
Experimental*	Perpendicular	1.171	-	-0.635
Error		7.98 %	-	1.82 %
CFD (tetrahedral)		0.549	-0.663	-0.205
CFD (polyhedral)		0.597	-0.731	-0.217
Experimental*	Tilted	0.724	-0.690	-0.387
Error (tetrahedral)		-24.11 %	-3.85 %	-47.06 %
Error (polyhedral)		-17.56 %	6.01 %	-43.95 %

\*Cermak and Peterka (1979)

Investigating the reported coefficients, it can be seen that for the perpendicularly orientated heliostat both the drag and overturning moment coefficients are predicted with good accuracy. It can also be seen that both coefficients are over-predicted which is somewhat unexpected on account of the velocity deficit produced by CFD compared to Cermak and Peterka (1979). A velocity deficit would impart less momentum to the heliostat and thus predicted coefficients would expectedly be lower than that reported by Cermak and Peterka (1979).

When looking at the coefficients for the tilted orientation it can be seen that only the lift coefficient is predicted with good accuracy. It can also be seen that when using a tetrahedral mesh all the reported coefficients are under-predicted. Considering the over prediction of the load coefficients for the perpendicular case, this result is unexpected.

Lastly, when comparing the results of the polyhedral mesh to the tetrahedral mesh, it can be seen that in predicting the drag and overturning moment coefficients the polyhedral mesh is slightly more accurate. The lift coefficient is also found to be over-predicted when compared to both literature (Cermak and Peterka, 1979) and the result from the tetrahedral mesh. Lastly, it can be seen that the polyhedral mesh produces larger magnitude of load coefficients than the tetrahedral mesh for all reported coefficients.

#### 5.4.2 Boundary layer inlet profile

As with the simulations done with flat inlet profiles, again, the first result of concern was how well the upstream velocity and turbulence profiles produced using CFD matched those reported in Cermak and Peterka (1979). The profiles produced by CFD 0.7 m upstream of the heliostat for both orientations have again been plotted against the experimentally produced profiles reported by Cermak and Peterka (1979) and the results can be seen in Figure 5-12.

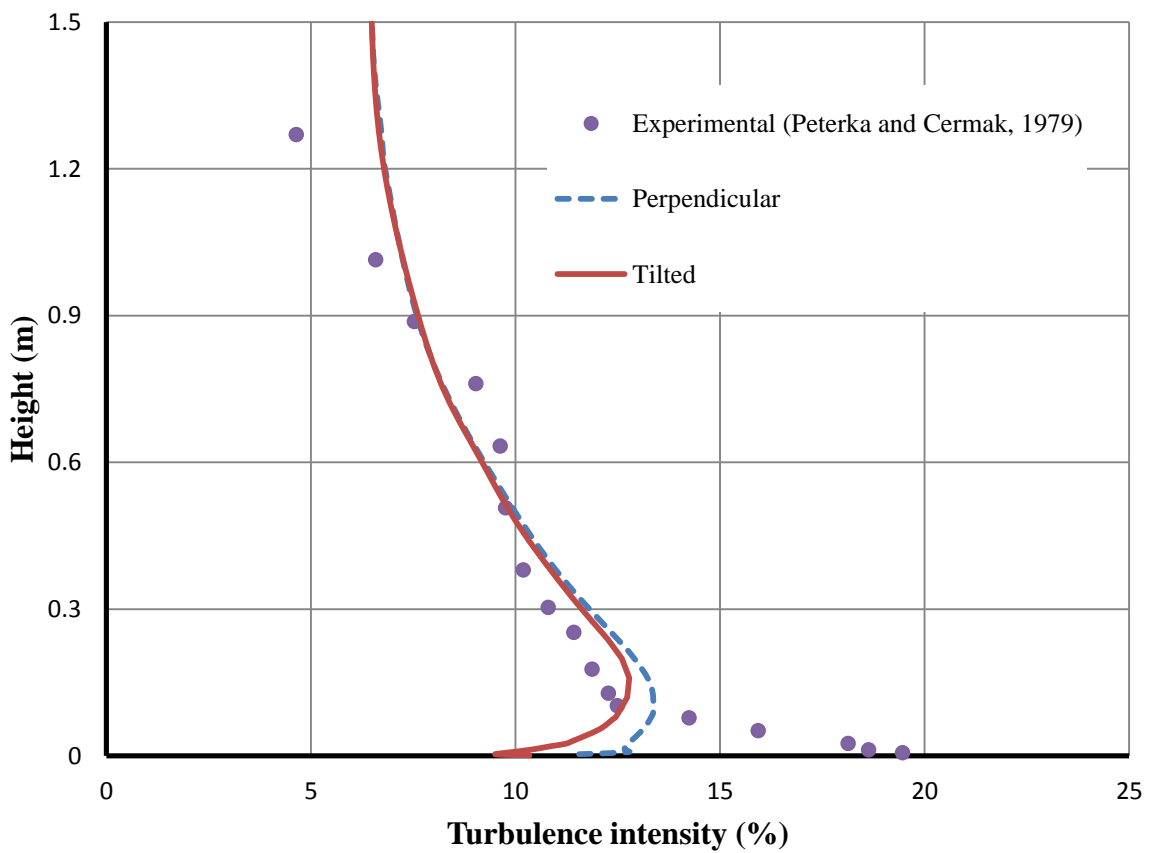
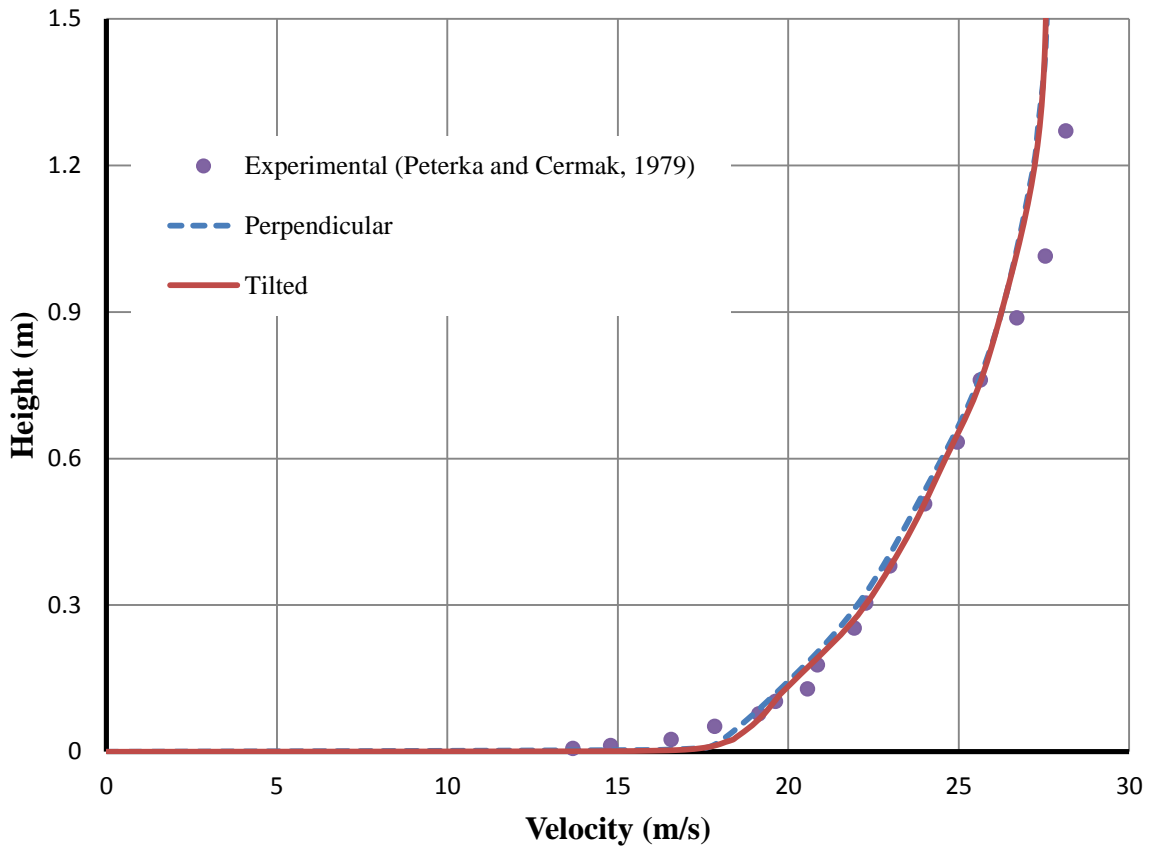


Figure 5-12: Comparison of boundary layer velocity and turbulence profiles

From Figure 5-12 it can be seen that for both orientations the velocity profiles match each other almost identically even with the perpendicular case having a cutcell mesh and the tilted case having an embedded tetrahedral mesh. These simulated velocity profiles in turn match well with the experimentally produced profile of Cermak and Peterka (1979). Slight differences are seen near the ground and further into the free stream which show a velocity excess and deficit, and only a velocity deficit respectively.

Regardless, both cases show decreased turbulence intensity up to around 0.1 m vertically into the domain and slightly increased turbulence intensity between around 0.1 m and 0.5 m vertically into the domain when compared to the results of Cermak and Peterka (1979). Considering the heliostat extends approximately 0.3 m vertically into the domain, the difference between the experimental and simulated velocity and turbulence profiles would be expected to produce errors in the coefficients predicted as for turbulences intensities above 10 % Perterka and Derickson (1992) found significant increases in the loads on a heliostat. However, in a study by Verma *et al.* (2010) the increase in load was only found to be a factor of 1.069 for an increase in turbulence intensity from 10 % to 25 % within the simulation environment. This would point to the incorrect turbulence profiles possibly not having as significant an effect on the loads as would be expected.

As with the previous section the primary focus of the simulations was obtaining the predicted load coefficients. These have been reported in Table 5-2 and, for reasons previously mentioned, only the drag, lift and overturning moment about base coefficients have been reported.

Table 5-2: Load coefficients for boundary layer profiles

	Orientation	$C_{F_x}$ (Drag)	$C_{F_z}$ (Lift)	$C_{m_{y_{base}}}$ (Overturning moment about base)
CFD		1.761	-	-0.967
Experimental*	Perpendicular	1.094	-	-0.653
Error		60.98 %	-	48.09 %
CFD		0.725	-0.874	-0.272
Experimental*	Tilted	0.646	-0.602	-0.335
Error		12.28 %	45.26 %	-18.69 %

\*Cermak and Peterka (1979)

For the perpendicularly orientated heliostat it can be seen that both the drag and overturning moment coefficients are significantly over-predicted. This could be as a result of the velocity profile issues previously mentioned, in section 5.4.1, which results in more of the heliostat being exposed to a larger velocity than that of the experiments done by Cermak and Peterka (1979). This imparts a greater momentum onto the heliostat which results in a larger force and associated coefficient. Also, considering that the overturning moment about the base of the heliostat is strongly linked to the drag force on the heliostat in this orientation, the over prediction of the overturning moment coefficient is expected after investigating the drag coefficient.

Next, the tilted heliostat case is inspected and it can be seen from Table 5-2 that the reported coefficients for drag and overturning moment are more accurate than for the perpendicular orientation and are within 20 % of the coefficients reported by Cermak and Peterka (1979). The lift coefficient is, however, almost 50 % over-predicted and it can be seen that the drag coefficient is also over-predicted whilst the overturning moment is under-predicted. This is unexpected as the increase in horizontal and vertical force (drag and lift) on the heliostat should expectedly result in an increased overturning moment due to an increased net force on the heliostat. This, however, is not the case with the overturning moment being under-predicted by around 20 %.

## 5.5 Discussion and conclusion

From the results presented for the load coefficients on a heliostat in two orientations it can be said that the CFD method utilised may not appear to be adequate at this point in predicting exact heliostat loads at all orientations. This comes about due, mainly, to the poor performance of the CFD method utilised in predicting accurate load coefficients when exposed to a boundary layer flow profile. The differences which arise between simulated and experimental profiles when the simulation is exposed to no obstacles in the flow would appear to be a possible issue for this flow case. If more focus is placed on producing highly accurate velocity and turbulence profiles in closer upstream vicinity of the heliostat, then improvements on the load predictions for a heliostat could possibly be achieved. This is further supported by the better prediction of load coefficients when using flat velocity and turbulence profiles which appear more accurate in close upstream vicinity of the heliostat.

One thing to note when investigating the results is the fact that for the case of the tilted heliostat exposed to a boundary layer flow the accuracy of the prediction of loading coefficients was highly improved compared to the same heliostat orientated perpendicular to the flow. This could suggest that for heliostats which are located further off the ground the CFD method used could predict their loadings with good accuracy due to the main errors with the boundary layer profiles being in the region close to the ground.

Another possibility for the poor performance of the CFD method utilised for this case may be that the limits of the two equation Realisable  $k-\epsilon$  model may be reached with such geometry. Bluff body geometries are associated with extremely complex flow features, such as recirculation, separation and vortex shedding as well as a complex distribution of the strain rate, as shown in Figure 3-4. With these considerations the best way forward would be to use more powerful methods of flow modelling. It can, however, be concluded that this particular approach may be useful in determining the differences between various different heliostat designs early in the process by using flat inlet profiles.

## 6. Particle Image Velocimetry (PIV)

During the course of this thesis the opportunity arose to get involved with experimental work involving an investigation into the flow pattern surrounding an isolated by means of PIV. All of the experimental work, apart from setup and post-processing of the heliostat orientations presented in this chapter, was undertaken by final year student Danica Bezuidenhout, (2014) as this work was her final year project. The experimental work served the purpose of further validating numerical simulations conducted on the same geometry as that experimented on.

### 6.1 Simulation conditions

As with the previous sections the geometry will be presented first. For the experimental work conducted the geometry used was based on the heliostat design for HELIO 40, which was a project undertaken by the Solar Thermal Energy Research Group (STERG) at Stellenbosch University. Some aspects were left out when developing the scale model, the most significant of which were the mirror rear support structure and the drive mechanism. The final geometry used was similar to flat plate presented in section 4.1 with the main differences being the dimensions of the plate and support pole. The geometries used in the simulations and experimentation for this section is shown in Figure 6-1 with the major dimensions for the simulation heliostat being shown in Appendix F: Dimensioned Geometry. Not that due to the manner in which the heliostat was mounted in the wind tunnel (with the ribbed section below the wind tunnel floor) the only significant difference between the geometries shown is the hinge section, which was changed due to it creating some meshing issues.

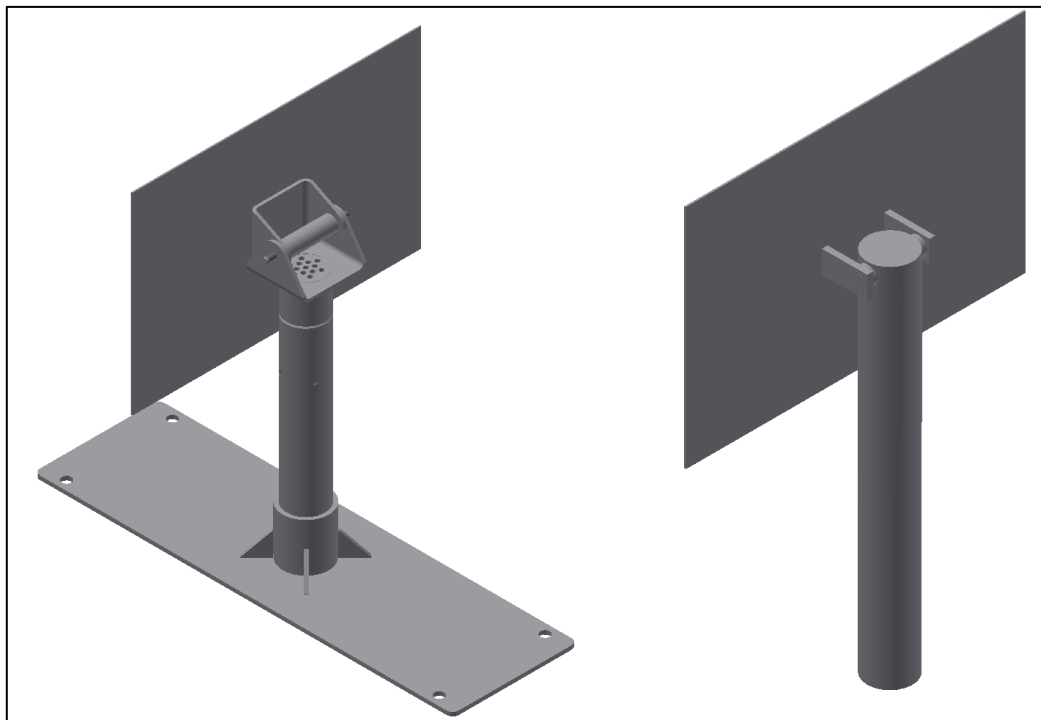


Figure 6-1: Wind tunnel (left) and simulation (right) geometry

As with the simulations in section 5 only two orientations were of concern when running the simulations and again these were chosen to be a heliostat oriented perpendicular to the flow and a second orientation with an azimuthal and inclination angle of  $45^\circ$ . This can be visualised by inspecting Figure 5-3 but replacing the existing heliostat with the geometry shown in Figure 6-1.

Once the geometry was created and imported into ANSYS the same steps were taken as with the previous sections in creating the flow domain. In this case, the domain extents measured 3.1 m upstream of the heliostat and 6.5 m downstream of the heliostat with a total height of 1.5 m and total width of 3 m. Due to meshing issues occurring for both orientations tested that were similar to those described in section 5.2 for the tilted heliostat, the domain was again split into four sections with the final domain and location of the heliostat shown in Figure 6-2.

Once the geometry was created the domain was meshed in the same manner as the process described for the tilted heliostat orientation in section 5.2. For both orientations tested, at least four meshes of increasing density were created in order to check for mesh independence by comparing heliostat load coefficients. The final meshes used for both orientations can be seen in Figure 6-3.

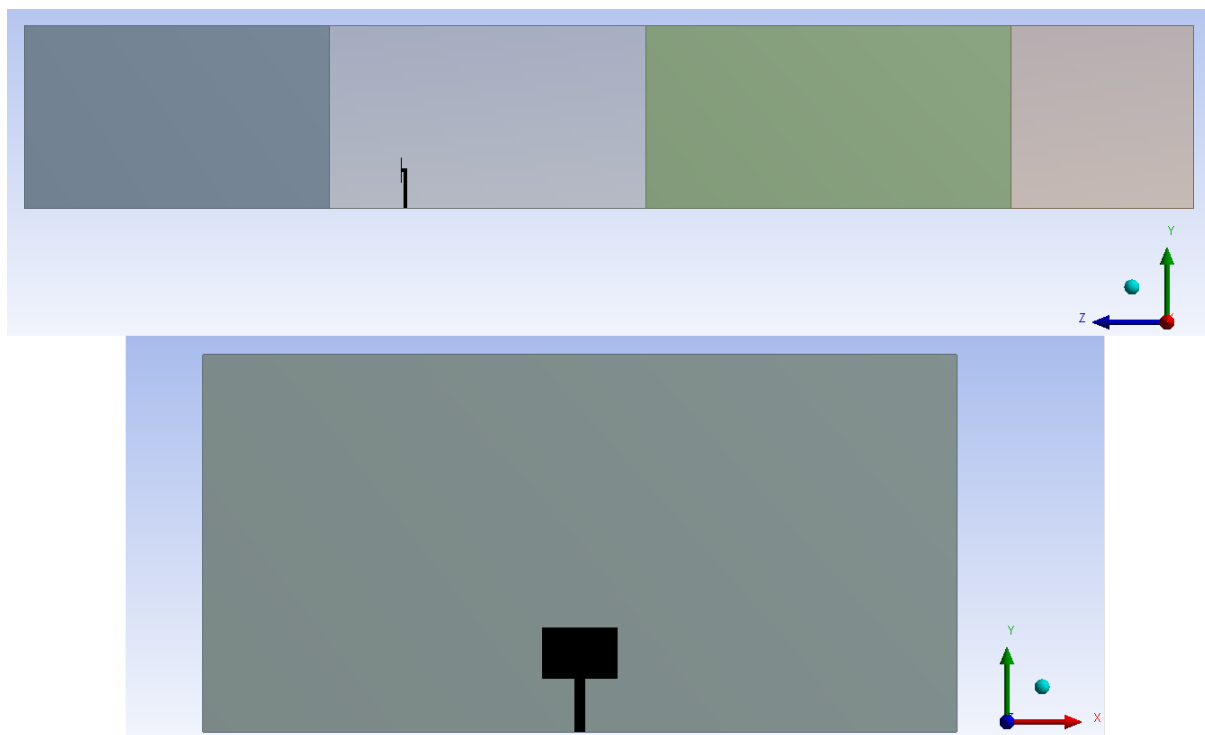


Figure 6-2: Side view (top) and front view (bottom) of heliostat within domain

Once the domain was meshed the simulation was setup much in the same way as that in section 5.3 for the flat velocity and turbulence profiles. For this case, however, fewer monitors were put in place as the PIV would not produce results pertaining to loadings on heliostat, rather, it would provide information about the flow field about the heliostat in a given plane. As such; monitors were only in place to ensure that once again the selection of a

steady state simulation was valid. Another change was specifying all the external surfaces of the domain as non-slip walls in order to reproduce conditions closer to the experiment, namely, that the walls of the wind tunnel are in fact non-slip walls.

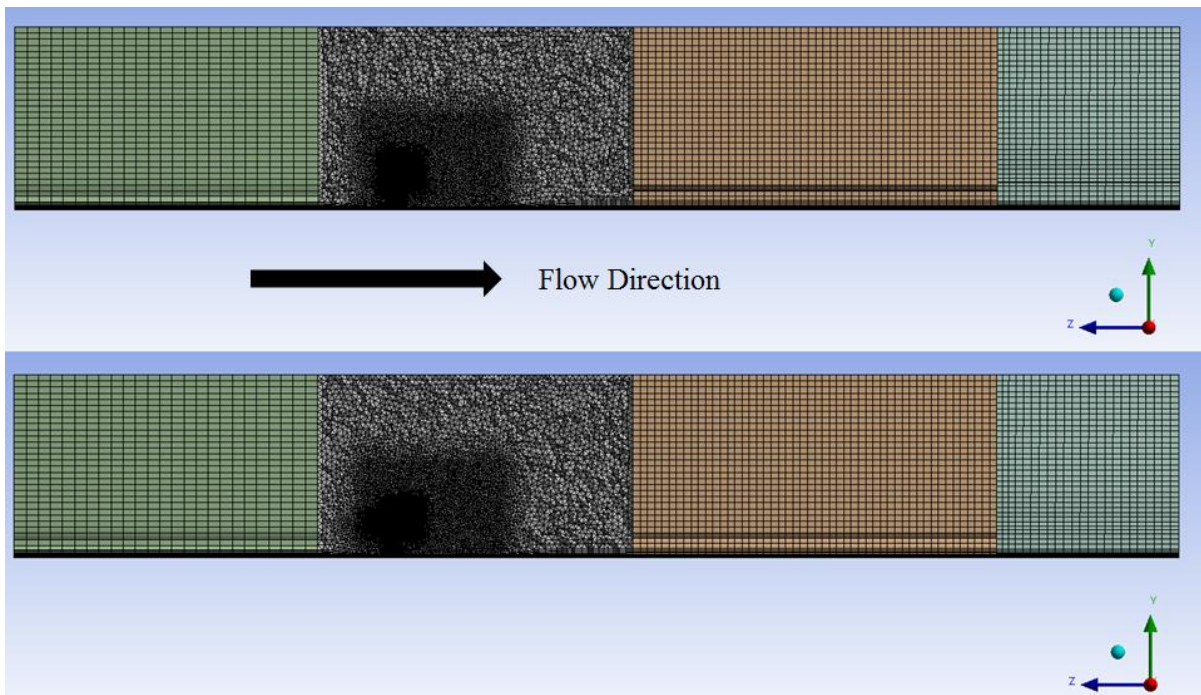


Figure 6-3: Finest mesh for perpendicular (top) and tilted (bottom) heliostats

## 6.2 Brief PIV description

PIV is a non-intrusive method used to measure and visualise velocity, and other related properties, for a variety of fluid flows. It achieves this by using a laser to illuminate particles that are seeded into a flow and capturing an image of the illuminated particles using high speed cameras. Image and data processing software is then used in the post-processing stage to track individual particles between two consecutive images and by using the time between images combined with the change in a particle's position a velocity vector can be generated between the particle's two positions. By doing this for a number of particles within a flow, information about the entire illuminated and seeded flow field can be extracted. A schematic of the PIV process can be seen in Figure 6-4.

There are some issues associated with PIV such as image glare and shading which results in flow information in these areas being incorrect. The way overcome these issues is to effectively omit these areas from being processed by the software by 'masking' them in the post-processing stage of PIV analysis. An example of an image which contains both glare and shading can be seen in Figure 6-5.

Other issues occur at the edges of the zone being processed as the particles appear to software as disappearing which can result in large and unrealistic velocities. This issue is overcome using certain validation features within the software to ensure the final data obtained is

sound. When using the PIV equipment there also various health and safety issues which have been addressed in the safety report found in Appendix D: PIV Safety Report.

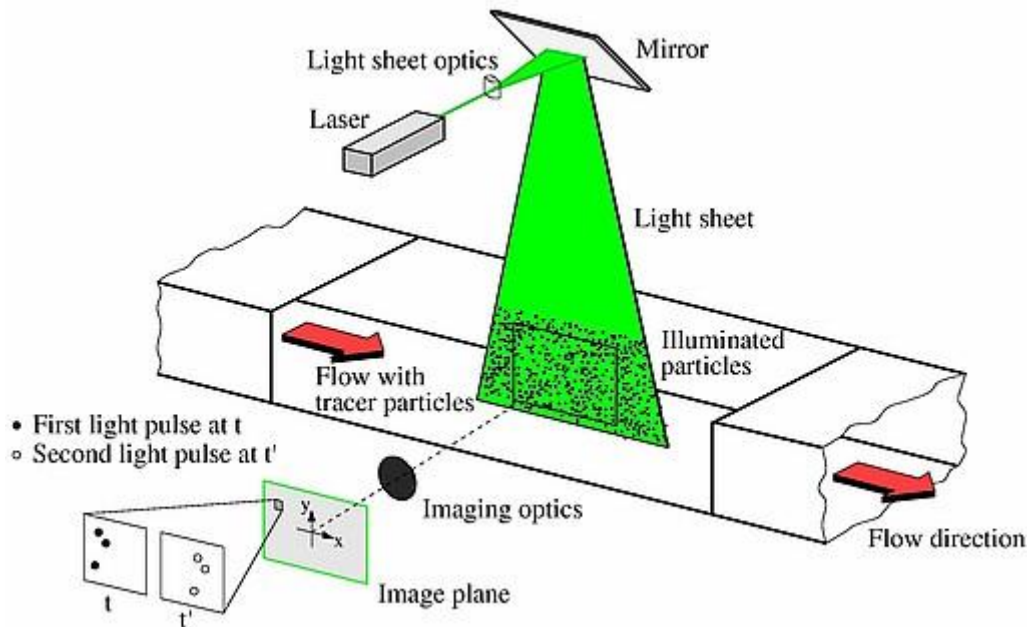


Figure 6-4: Schematic of PIV process (AIM<sup>2</sup>, 2014)

### 6.3 Experimental setup and procedure

The first stages of experimentation involved design and manufacturing of the heliostat, and this was done by Bezuidenhout (2014) as this was part of her final year project. Also, before experimentation could be conducted, calibration of the equipment had to be done, for which the calculations were largely conducted by Bezuidenhout (2014) as her project was entirely based around experimentation whereas this thesis is primarily focused on simulation work.

With regards to the calibration; this was done to ensure that the correct velocities were used during testing by checking the voltage output of the pressure gauges in the wind tunnel. The process of calibration involved using a manometer to obtain a range of pressure head readings along with their associated voltage readings from the wind tunnel pressure gauges. This allowed the pressure gauges to be checked to ensure the correct pressure reading from the manometer. This also allowed the velocity associated with these pressure readings to be calculated thus leading to the test velocity of 30 m/s to have a voltage associated with it. The relationship used to calculate the associated velocities was:

$$p = \frac{1}{2} \rho v^2 \quad (6-1)$$

which is the expression for dynamic pressure.

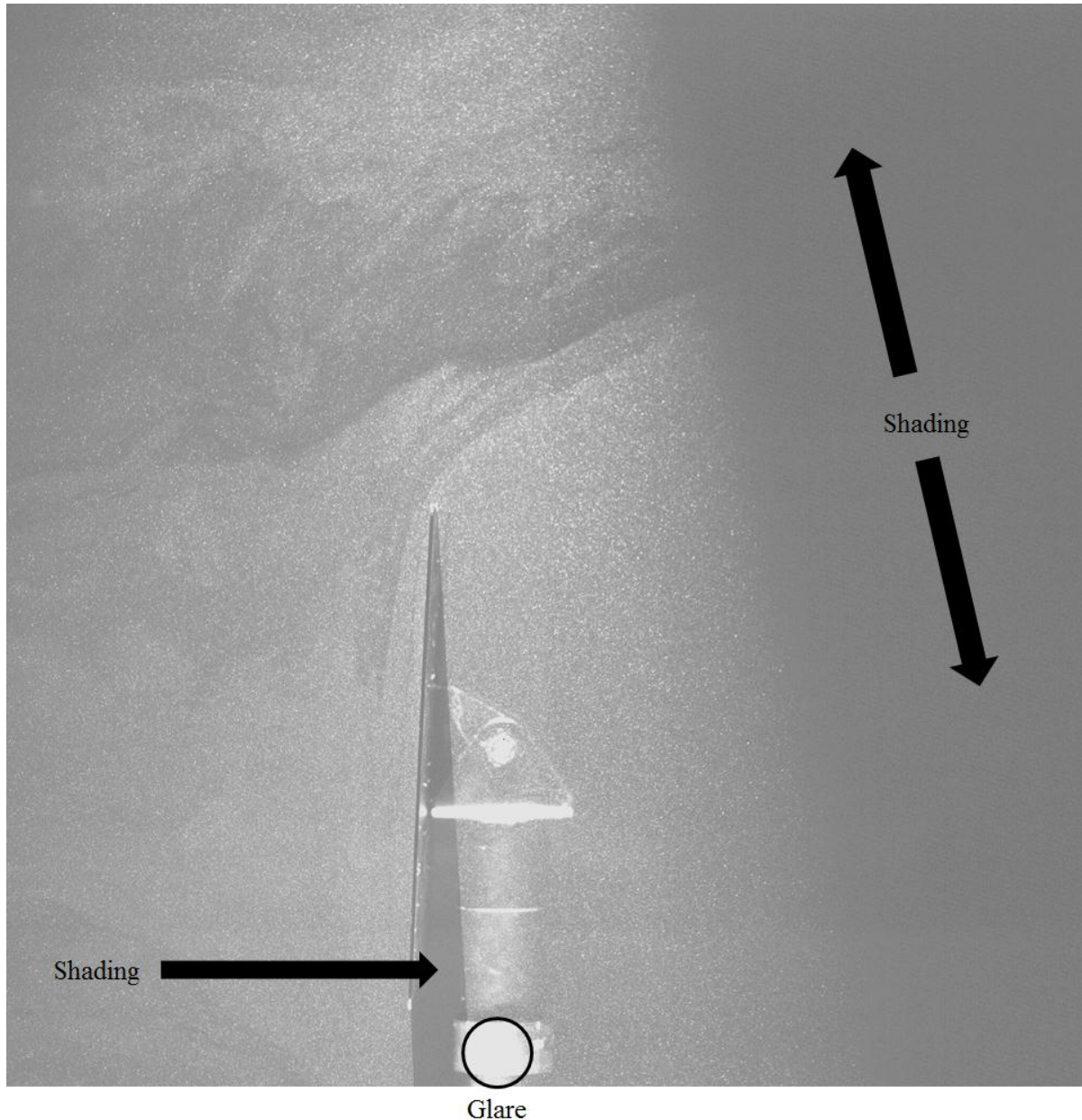


Figure 6-5: Known problems with PIV photograph capture (shading and glare)

Once the test equipment was calibrated the various safety risk issues were addressed, such as spray painting some of the bright areas within the test section of the wind tunnel to attenuate reflection of the laser light. For a more complete description of the safety procedures that could be taken refer to the safety report in Appendix D: PIV Safety Report. The heliostat was then setup within the wind tunnel and the PIV equipment was put into place.

The software was then calibrated by placing a calibration plate similar to that shown in Figure 6-6 in the position of the plane of the laser sheet and using the calibration option within the software. This would ensure that the correct velocities would be calculated in the post-processing stage as the software would accurately know the distance a seeded particle would have moved in the time between photographs. Note that this process had to be repeated for each plane tested.

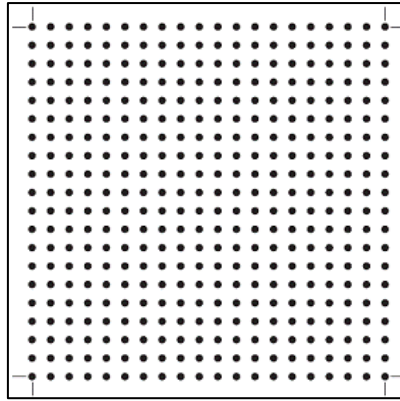


Figure 6-6: PIV calibration plate example (National Instruments, 2013)

Once the software was calibrated, the tests were conducted and the results evaluated. For the total experimental set two vertical and one horizontal plane was tested, however, for this thesis only information in the two vertical planes was of interest. This was primarily due to the exact location of the horizontal plane being unknown and that the tilted orientation was not tested for this plane due to time constraints. Note that for the tilted orientation data was obtained for two vertical planes, however, for the perpendicular heliostat data was only collected for a single vertical plane. Photographs showcasing the experimental setup can be found in Appendix E: Photographs of Experimental Setup.

#### 6.4 Experimental and simulation results

When comparing the results obtained from experimental PIV to simulations there are two types of information that can be extracted and compared. First are the quantitative velocity profiles which can be extracted along sampling lines and second is the qualitative planar streamlines. The combination of these types of information would provide a good idea of the capability of CFD to predict flow fields about a heliostat.

##### 6.4.1 Velocity profiles

The comparison of experimental and simulated velocity profiles provides the most important information regarding how well the simulation can predict the flow field about a heliostat. Thus it is important that the information about the experimental velocity field be extracted only from regions in which the quality of the data is good. An example of such a region is shown in, Figure 6-7, in which the velocity profile is extracted along the black, vertical line. Note that sampling from the enclosed regions would provide bad data as these regions are near the edge of the illuminated plane and it can be seen that the vectors generated are bad quality.

Note that the profiles presented in Figure 6-8 to Figure 6-13 are indexed in increasing distance downstream of the heliostat apart from the line '01' in Figure 6-8 and Figure 6-9 as these are upstream of the heliostat. For details regarding the locations of the velocity profiles presented please see Appendix G: Details of Velocity Profile Locations.

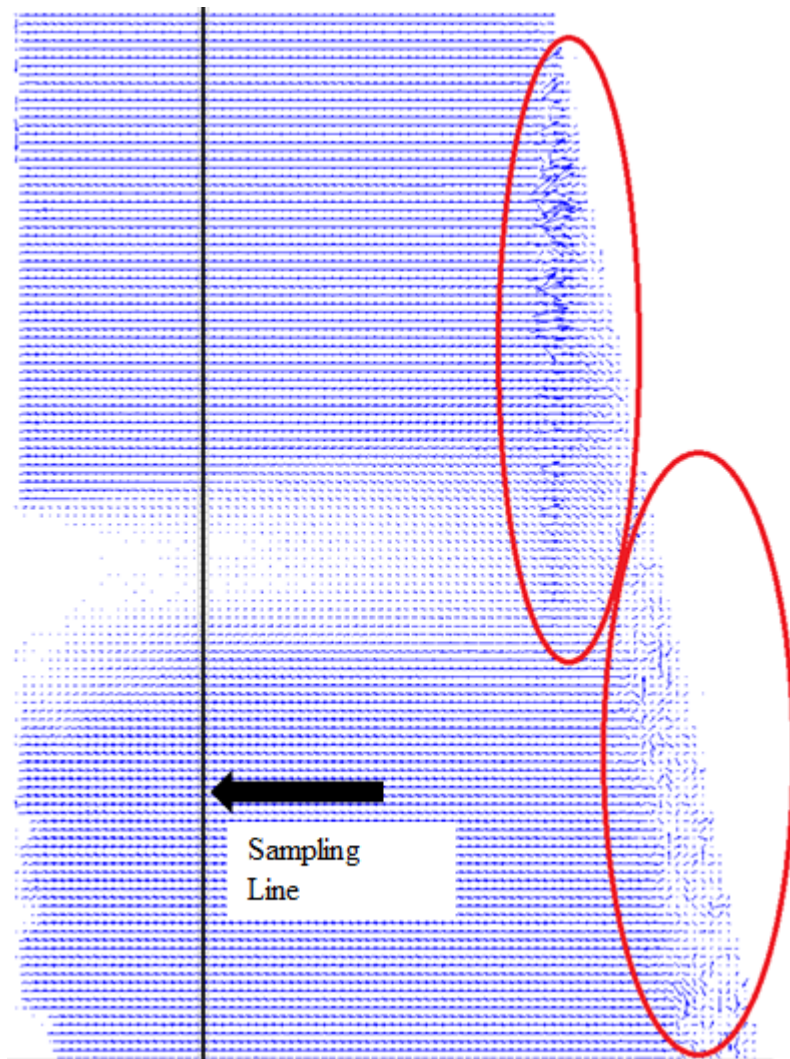


Figure 6-7: Example of good (black line) and bad (enclosed) sampling areas

When investigating the comparison of velocity profiles produced through experimentation and simulations, from visual inspection it can be seen that for the perpendicularly oriented heliostat the profiles match fairly well in shape and location. There can however be seen to be some discrepancies in the magnitude of the streamwise and vertical velocities in the wake of the heliostat. By comparing the average velocities across these plots a difference was found of around 77 % and 28 % for the streamwise and vertical velocities respectively. An example of the region in which there is a large difference is, for example, around 0.35 m up in Figure 6-8 where the difference between simulation and experimentation, for the line indexed '03', is around 60 % which is quite significant. With regards to the vertical velocity profiles, in the region of around 0.52 m in Figure 6-9, the difference is found to be around 40 % for the line indexed '05'. Thus, whilst the profiles appear to look fairly accurate from a visual inspection there are actually some major differences between the simulated and experimental profiles for the heliostat orientated perpendicular to the flow.

The next set of profiles is for the tilted orientation taken along a vertical plane across the middle of the heliostat. When analysing the profiles in this plane it was found that the difference between average velocities was around 2.7 % and 14.8 % for the streamwise and

vertical velocity profiles respectively. This would indicate fairly accurate prediction, however by visual inspection of Figure 6-10 and Figure 6-11 it can be seen that there are large discrepancies between simulated and experimental profiles. An example of such is in Figure 6-10 where at a height of approximately 0.35 m the difference between the lines indexed as '03' is around 74 % which is significantly incorrect. At the same height for the same sampling line an error of around 27 % is found in Figure 6-11, which is not as severe, however, by visual investigation of the lines indexed '02' and '01' it can be seen that this error increases closer the heliostat as these lines are sampled closer to the heliostat.

The last set of velocity profiles to be investigated are for the tilted heliostat but taken from an offset plane, 60 mm inwards from the outer side edge of the heliostat with the profiles shown in Figure 6-12 and Figure 6-13. Analysis of the average velocities across these profiles showed that the difference between simulated and experimental profiles was around 28.5 % and 163.1 % for the streamwise and vertical velocity profiles respectively. When investigating the streamwise profiles in Figure 6-12 it can be seen that the simulated and experimental profiles have a similar shape however it appears as if the simulated profiles are much wider than the experimentally produced ones. An example of the inaccuracy which results from such a different profile can be seen in the region of 0.3 m for the profile indexed '03' where the difference between simulation and experimentation is around 117 % which is severely inaccurate. Referring to Figure 6-13 for the profiles indexed '04', '05' and '06'; major differences between simulation and experimentation can be found visually with the simulated profiles having an inverted shape in comparison to the experimental profiles. This is found to produce an inaccuracy of around 236 % for the line indexed '04' at a height of around 0.4 m which is quite severe.

The collection of results for the tilted heliostat may point to some vortex formation in the wake that is being predicted by the simulation. This can be said due both negative and positive velocities found in the profiles which would point to reversed flow and circulation occurring in the wake of the heliostat. However, the location of said vortex appears to be incorrectly predicted with one of the causes possibly being that the location of the sampling lines relative to the heliostat could only be placed with an accuracy of around 1 mm.

#### 6.4.2 *Streamlines*

Beyond the comparison of velocity profiles found through PIV, the experimental and simulated streamlines in the vicinity of the heliostat can be used to qualitatively determine how well the CFD method used can predict the flow field in the region around a heliostat. The streamlines for both simulation and experimentation have been plotted and compared in Figure 6-14, Figure 6-15 and Figure 6-16.

From Figure 6-14 it can be seen that the streamlines predicted by simulation do in fact match quite well with the experimental result. Considering the major issue with the velocity profiles predicted for this case was the magnitude of the velocities in some areas; matching of the general shape of the streamlines is expected as the streamlines are not indicative of the magnitude of the velocity of the flow in a specific region. It can be seen that the recirculation zone (A) is well represented for the simulation with both the upper and lower recirculation

zones being predicted. For the tilted case, however, there are some definite differences between the simulated and experimental streamlines.

Concerning the tilted orientation, for the streamlines along the mid plane, it can be seen that in the immediate wake of the heliostat the simulation predicts streamlines that are more vertical than the simulation (B). There is also a small recirculation zone (C) just below the top edge of the heliostat which is predicted by the simulation but does not appear in the experimental results. When moving to the streamlines along the offset plane; from Figure 6-16 it can be seen that the streamlines are less vertical in close downstream proximity of the heliostat when predicted by the simulation. Apart from these noticeable differences the simulated streamlines appear to visually be in fairly good agreement with those found experimentally. This illustrates the need to examine the velocity profiles from both simulation and experimentation in order to get a true representation of the performance of the CFD method used.

## 6.5 Discussion and conclusion

When examining the results, it is important to note that the PIV process essentially produces time averaged results for a case which is highly likely transient. Thus, comparing the simulated results to the PIV results will only provide insight as to whether or not the Realisable k- $\epsilon$  model is producing a time averaged image of the transient flow field result for this case. The fact that it produces a steady state result does not directly point to it producing a time averaged result for this case.

By considering how well CFD predicted the streamlines for a the perpendicular heliostat contrasted by its poor performance for the tilted orientation, the first conclusion that can be drawn is that; for the perpendicularly orientated case, the result is in fact steady state at the velocity tested. This conclusion is reached by first considering that the CFD produces a steady state result and that the PIV produces a time averaged result. Considering how well the streamlines produced from a steady state simulation agree with time averaged experimental results; it is likely that the experiment is in fact steady state itself.

Looking at the performance of CFD in predicting results for the tilted case, it can then be said that this modelling approach is inappropriate if information about the flow field about a heliostat is required. For this case the time averaged PIV results vary from the simulated results which may lead to two conclusions. One being that the experiment is indeed transient and that the steady state CFD produces the incorrect picture of the average flow field. A second conclusion could be that: even if the experiment is steady state, at this orientation the CFD method presented simply cannot cope with some of the more complex flow features associated with this type of flow which results in poor performance.

In terms of attaining accurate velocity profiles or qualitative flow information for a heliostat in either of the orientations tested, it can be said that the CFD method presented would be insufficient for attaining such data based on the inaccuracies presented for the various velocity profiles. Differences between simulated and experimental values of up to 236 % for

the tilted case and up to 77 % for the perpendicular case would point to this method not being suitable for determining qualitative data about the flow around a heliostat. It is clear that for modelling the flow field around a heliostat the Realisable k- $\epsilon$  model would not be appropriate except for the one known case of the heliostat orientated perpendicularly to the flow in which case only an idea of the streamlines about the heliostat could be attained with some confidence.

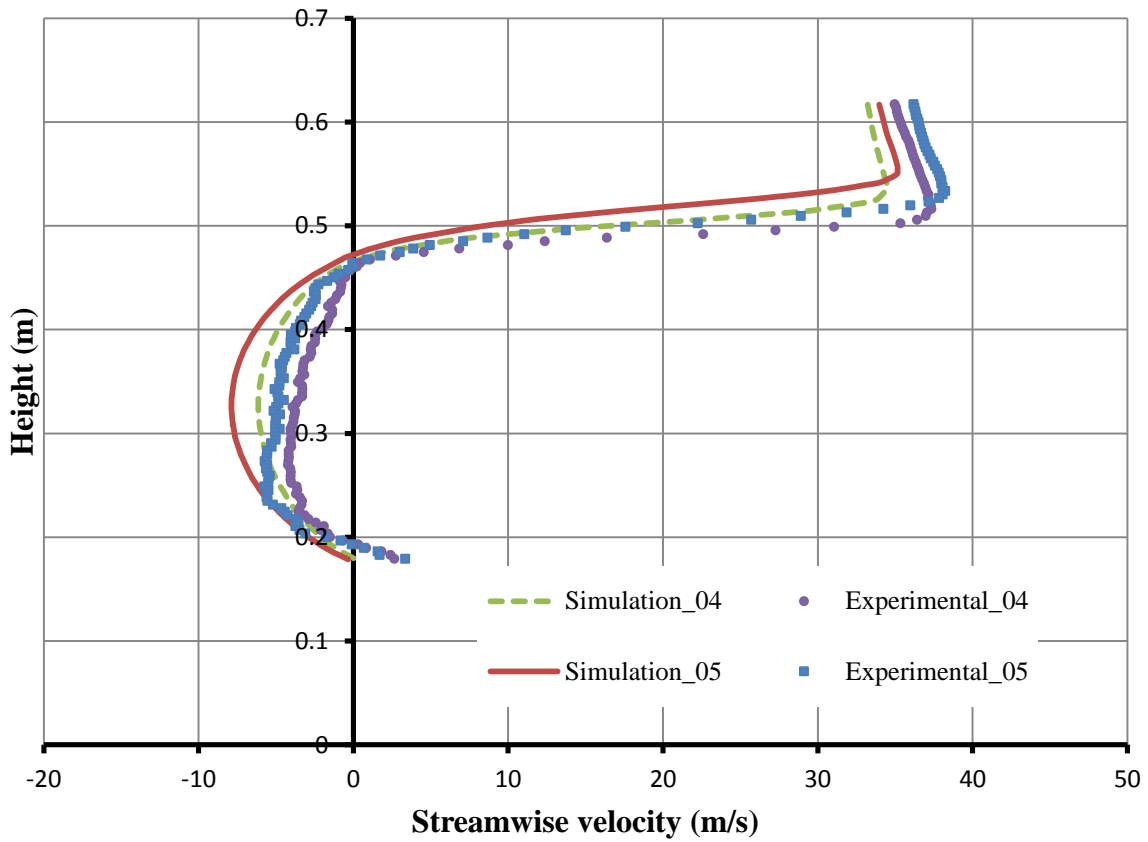
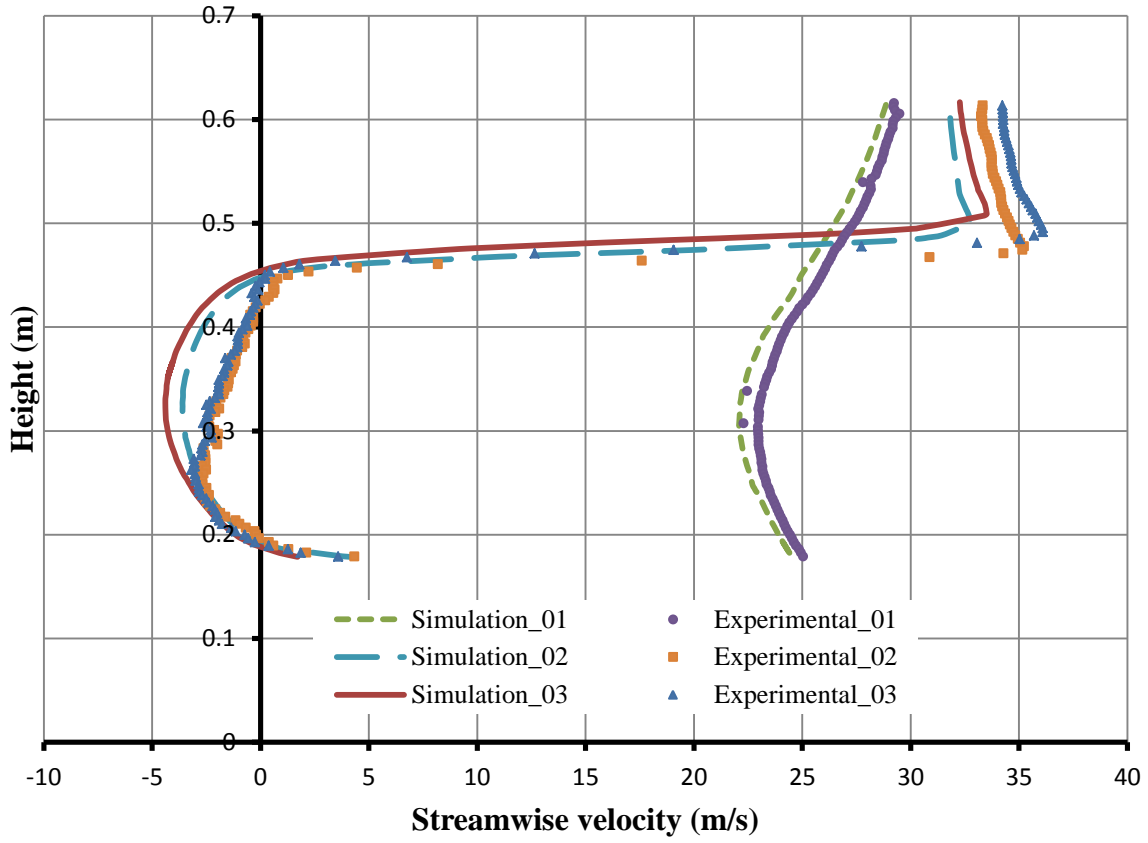


Figure 6-8: Perpendicular heliostat streamwise ( $u$ ) velocity profiles in offset plane

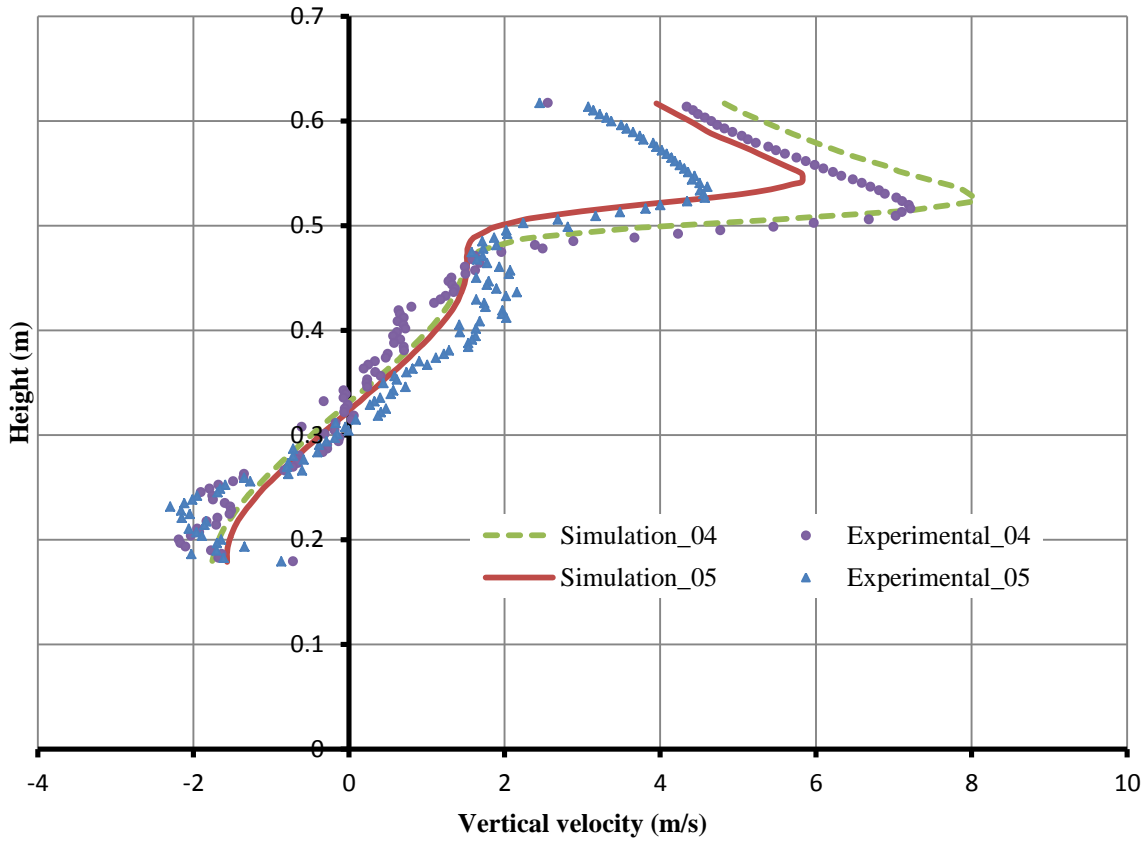
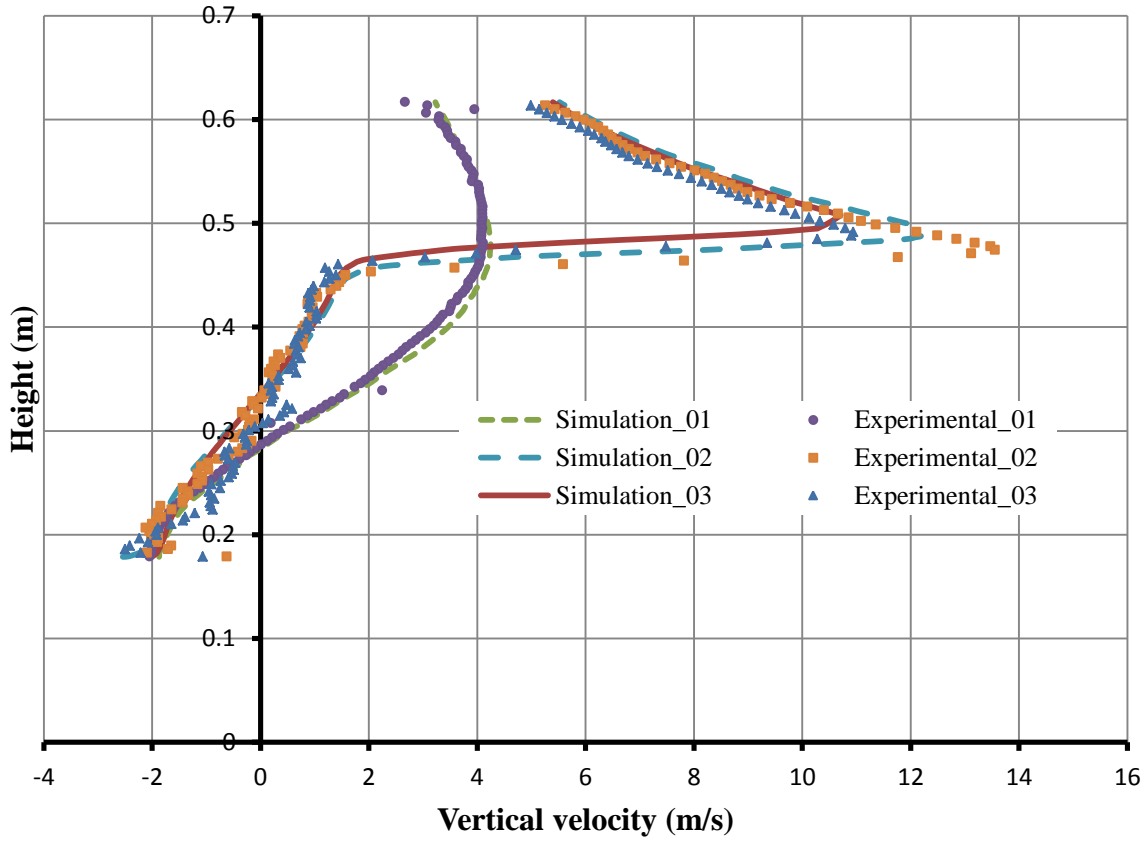


Figure 6-9: Perpendicular heliostat vertical ( $v$ ) velocity profiles in offset plane

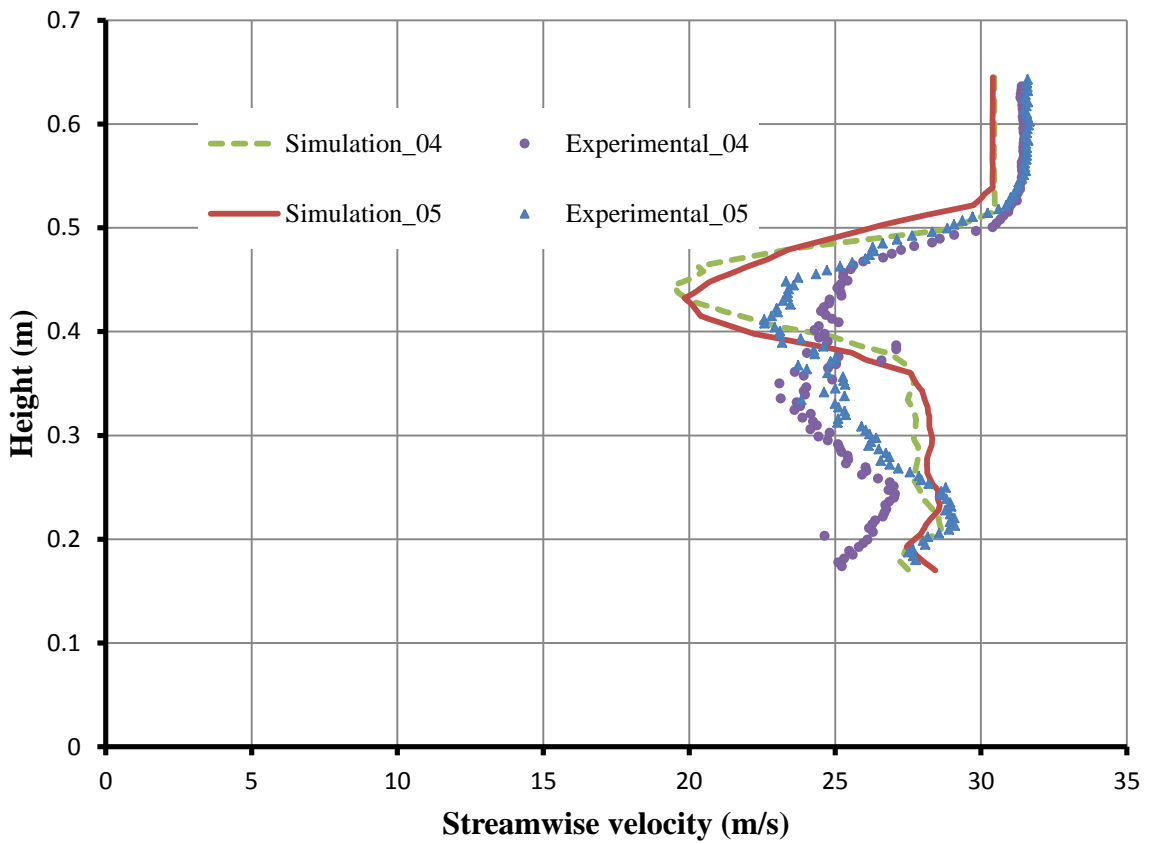
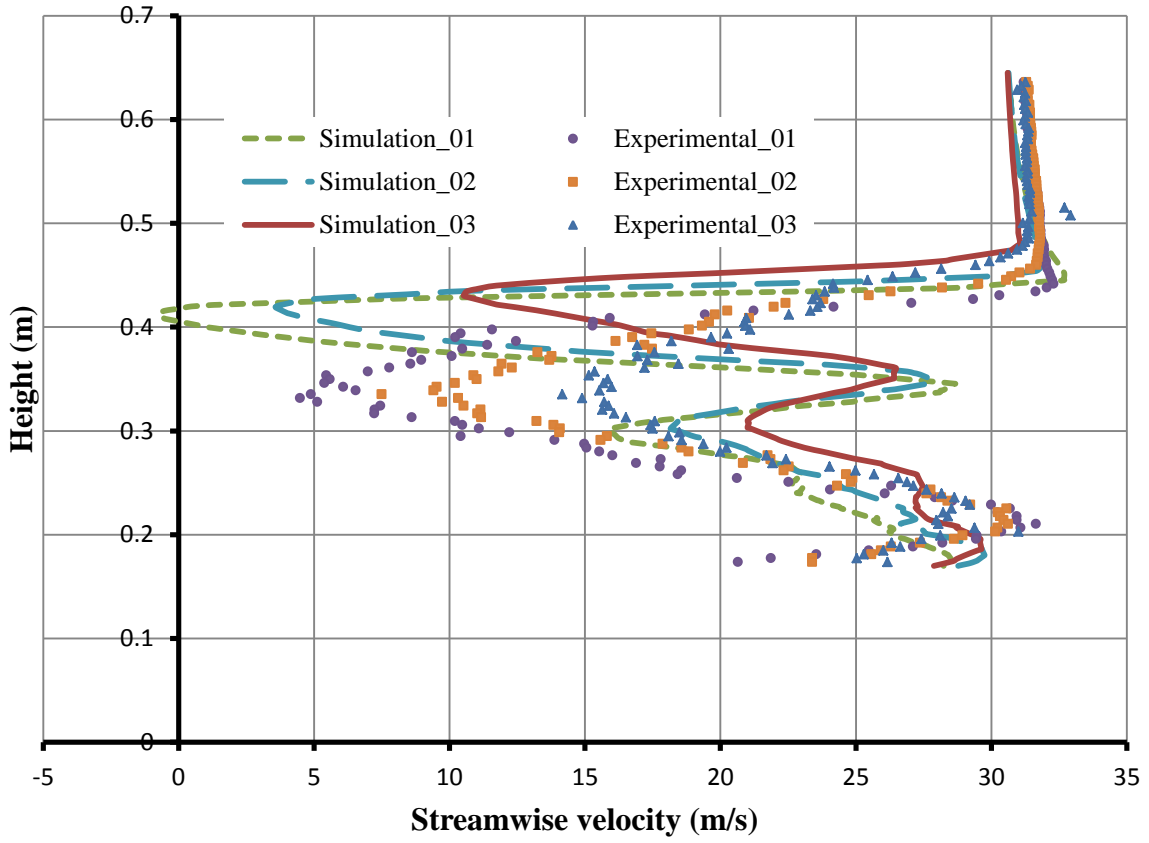


Figure 6-10: Tilted heliostat streamwise ( $u$ ) velocity profiles in mid vertical plane

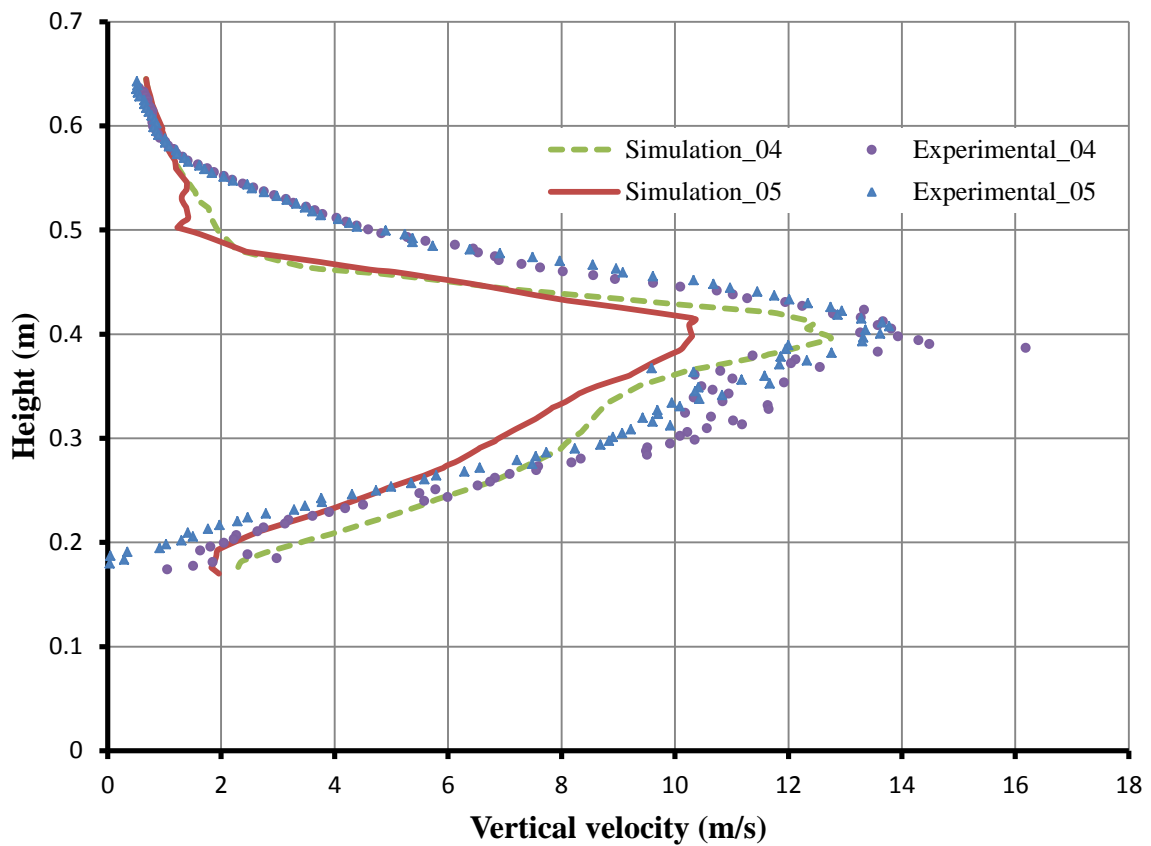
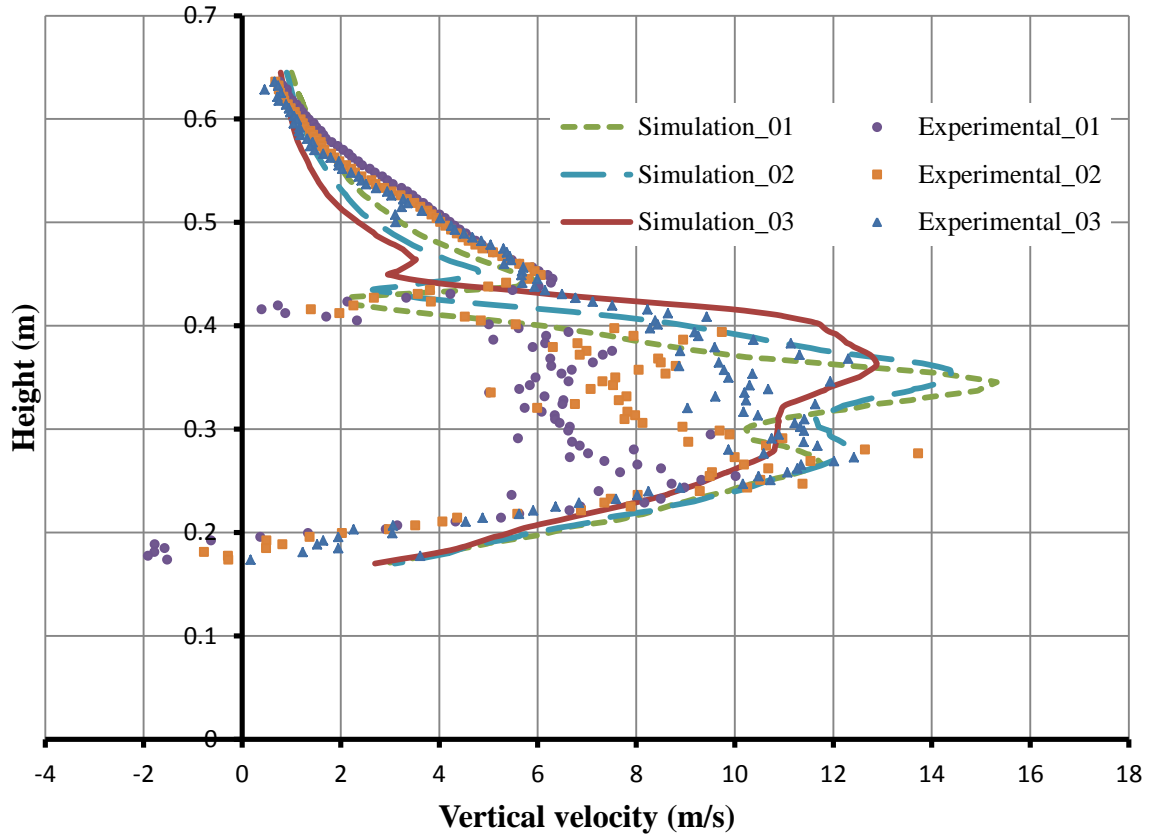


Figure 6-11: Tilted heliostat vertical ( $v$ ) velocity profiles in mid vertical plane

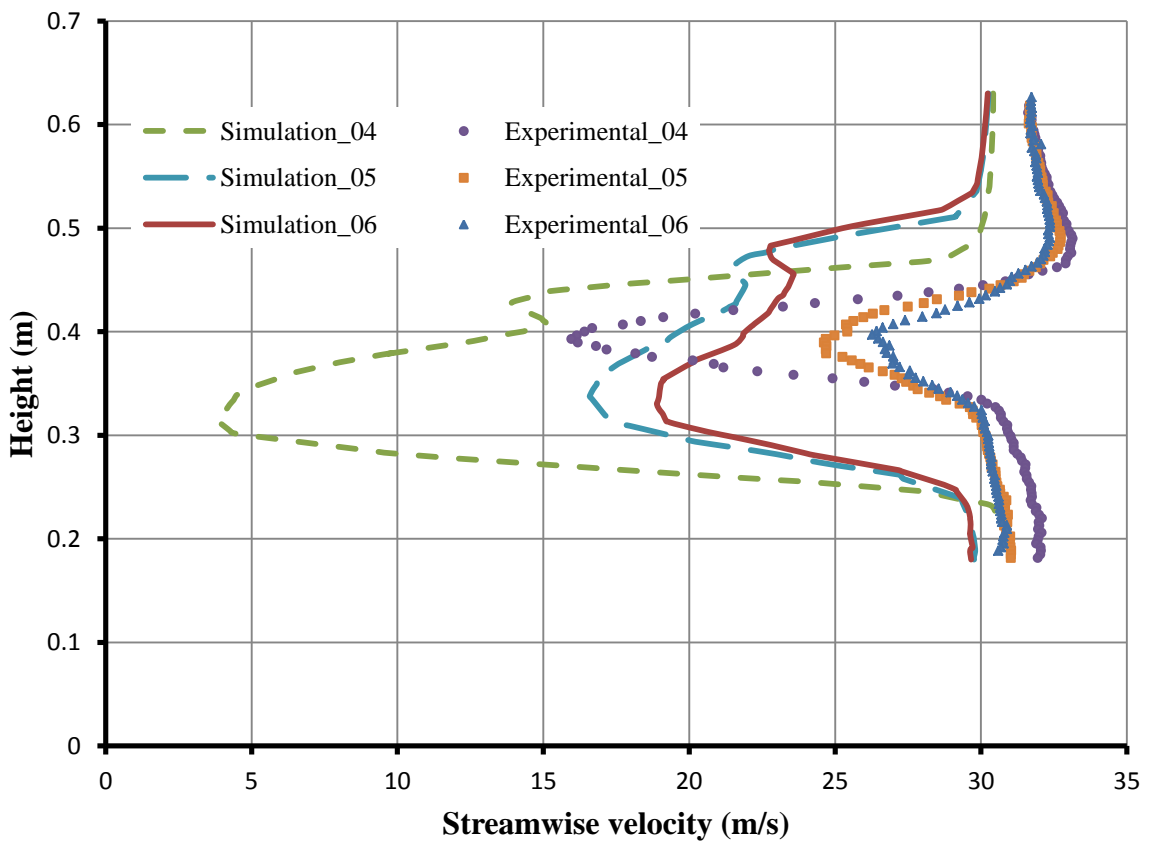
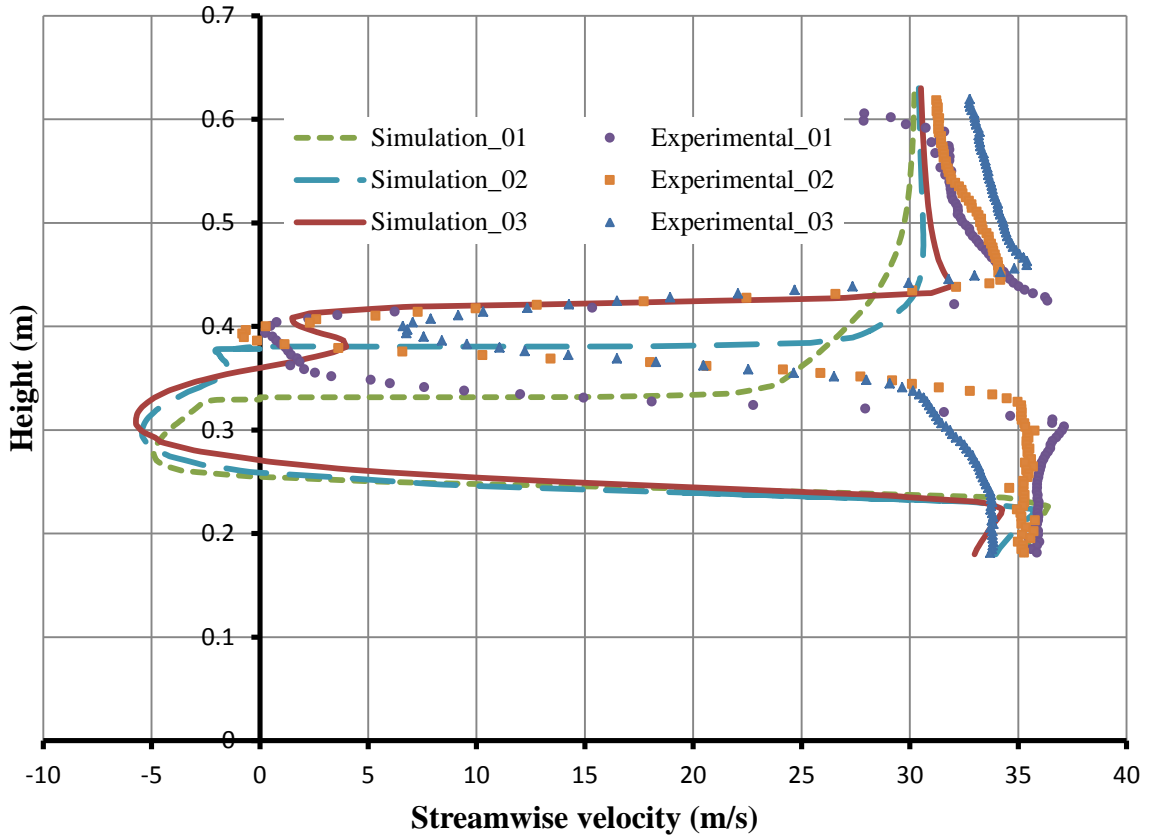


Figure 6-12: Tilted heliostat streamwise ( $u$ ) velocity profiles in offset vertical plane

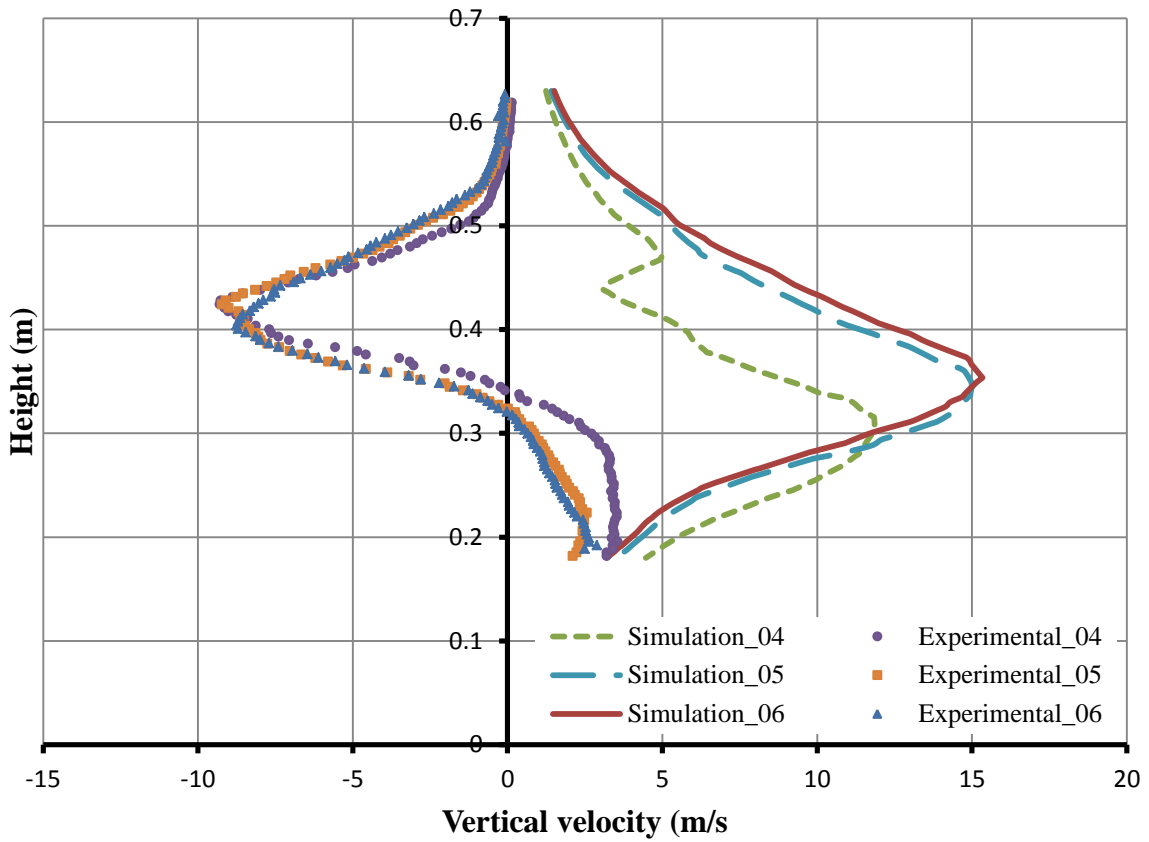
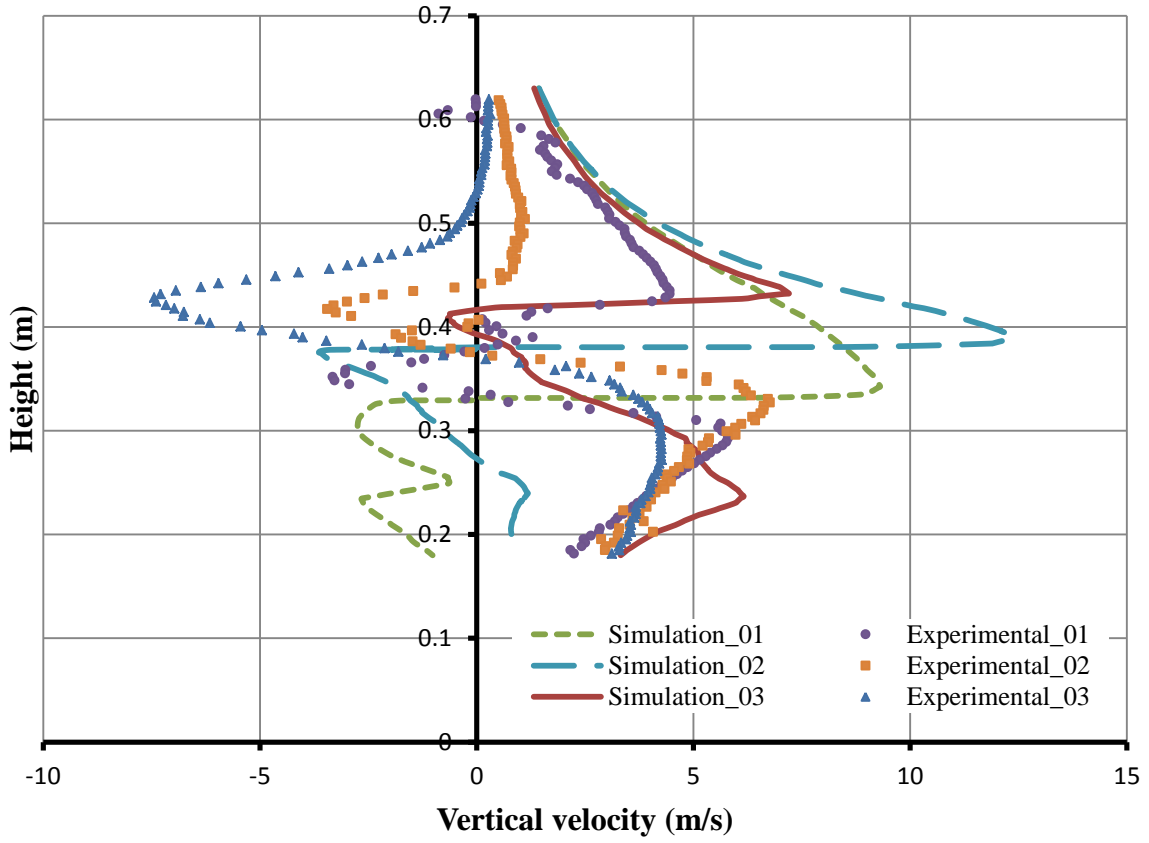


Figure 6-13: Tilted heliostat vertical ( $v$ ) velocity profiles in offset vertical plane

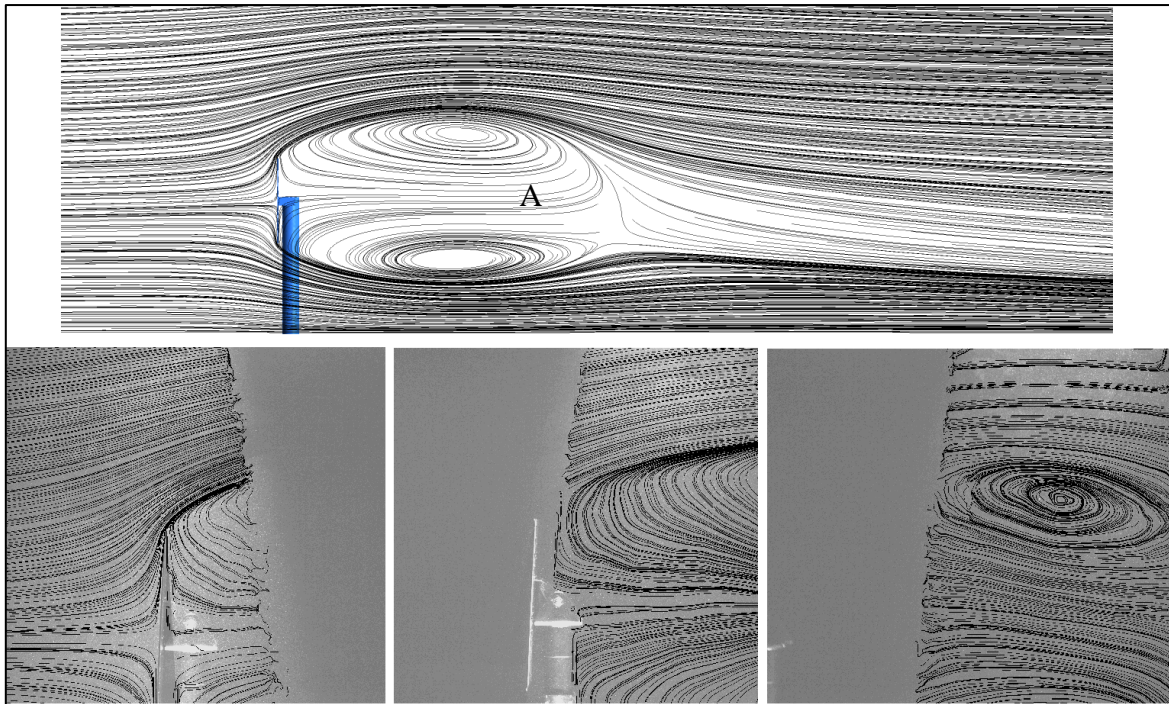


Figure 6-14: Streamlines for perpendicular heliostat in offset plane for simulation (top) and PIV (bottom)

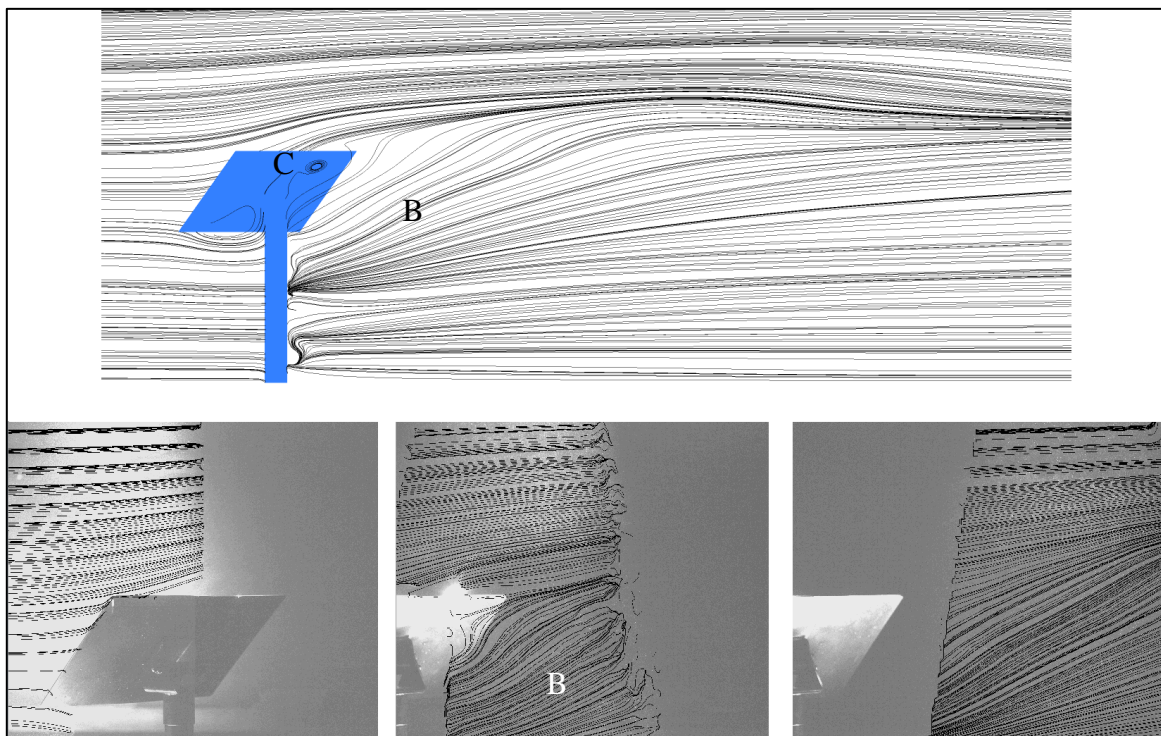


Figure 6-15: Streamlines for tilted heliostat in mid plane simulation (top) and PIV (bottom)

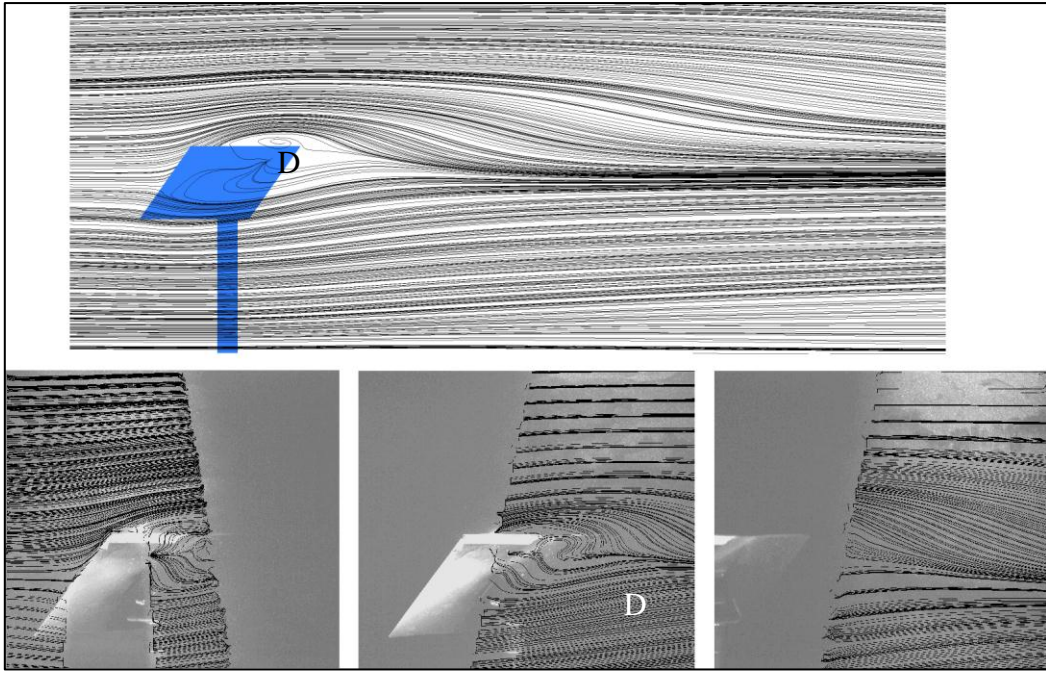


Figure 6-16: Streamlines for tilted heliostat in offset plane simulation (top) and PIV (bottom)

## 7. Summary and Conclusions

With the work conducted within this thesis, one of the objectives was to evaluate a number of RANS turbulence models with which heliostat wind loadings could be determined. This was initially done using simulations of flow over a flat plate with various turbulence models, of which the Realisable  $k-\epsilon$  was found to be the most suitable model moving forward. This was due to its good prediction of drag whilst producing a steady state result which meant reduced simulation time and computational resources. At this stage it was also concluded that from the two equation RANS models tested, the SST  $k-\omega$  would prove to be the best choice for transient simulations for heliostat like geometries due its prediction of transient data for both flat plate orientations tested as opposed to the RNG  $k-\epsilon$  which only produced transient data for a single case.

At the next stage the performance of the Realisable  $k-\epsilon$  model was tested for a heliostat geometry used for experimentation by Cermak and Peterka (1979). The performance was tested for two heliostat orientations and for both flat and boundary layer velocity and turbulence profiles. Varying meshing methods were also introduced and it was found that for the flat profile simulation, a polyhedral mesh performs better than a tetrahedral mesh, however, due to the lack of control over a polyhedral mesh it was not used any further in this thesis.

The mesh aside, it was found that for a perpendicularly orientated heliostat exposed to flat flow profiles the Realisable  $k-\epsilon$  model produced the reported coefficients with good accuracy. For the tilted orientation the accuracy of the CFD results did deteriorate, however, the lift coefficient was found to be reported with good accuracy. When further investigating the coefficients found with a boundary layer flow profile, the Realisable  $k-\epsilon$  model was almost 50 % off reported coefficients for the perpendicularly orientated heliostat, showing a significant change between flat and boundary layer profiles. For the tilted orientation tested it was found that the drag and moment coefficients reported were surprisingly accurate, with only the lift being significantly inaccurate in this case. It was concluded that one source of error in predicting the heliostat loadings originated in the errors found between the experimental and simulated upstream velocity and turbulence profiles in Figure 5-12.

It was also concluded that the issues regarding accurate prediction of the reported coefficients could be as a result of being at the limit of the capabilities of the Realisable  $k-\epsilon$  model for such a type of flow. As covered in section 3.5, the use of two equation RANS turbulence models utilising the eddy viscosity assumption have fell short in terms of bluff body CFD in the past and this may just be another case of that. To overcome this, the use of more powerful modelling techniques would be required, such as detached eddy simulation (DES) or LES.

Whilst the main outcome of this thesis was met by reaching the conclusion that use of the Realisable  $k-\epsilon$  model with a steady state approach would not suffice in predicting wind loads for a heliostat in all orientations, it was concluded that this approach could be useful in the early prototyping stages of heliostat design. By using a flat velocity and turbulence profile

differences between early prototyped designs could be determined which would reduce the time dedicated to wind tunnel testing and the associated costs of prototyping and testing. This is especially true as this method was accurate in the drag and overturning moment prediction for the heliostat in its maximum load orientation.

Beyond the prediction of heliostat loads the opportunity to get involved with PIV analysis arose which then allowed further investigation into how well the Realisable  $k$ - $\epsilon$  model could predict the flow field around a heliostat. Simulations were again run for two heliostat orientations, and it was found that the Realisable  $k$ - $\epsilon$  model could predict the streamlines around a perpendicularly orientated heliostat with good accuracy. It was, however, found that predictions for a tilted heliostat were not accurate and prediction of the velocity profiles for both orientations was also found to be inaccurate. Thus it was concluded that overall, the Realisable  $k$ - $\epsilon$  model should not be used to determine the flow field around a heliostat.

Overall the main objective of this thesis was to determine how well the method presented would cope in determining wind loads on heliostats and ultimately it was found that at the very least the Realisable  $k$ - $\epsilon$  model is insufficient to determine accurate wind loads for a heliostat in all orientations. It can, however, be used early in the process for determining the best design from a range of designs after which experimental testing will be needed to accurately determine design loads.

## 8. Possible Future Work

Considering the ground work laid in this thesis, future work should include the use of other turbulence models in determining the wind loads on heliostats. The aforementioned SST  $k-\omega$  and RNG  $k-\epsilon$  model could be looked at, however, ideally more computationally expensive modelling techniques should be applied. These could include RSM modelling, DES or if the computing power is available, LES.

Further investigation should also be done with the current method in ensuring accurate sustain of the modelled boundary layer longer into the domain. Errors between the applied inlet and upstream (of heliostat) velocity and turbulence profiles may have led to bad load predictions and thus if focus is put on this area the accuracy of load prediction for the simple method used here may increase.

Lastly, a larger set of data could be generated using the method utilised in this thesis, that is; obtain load coefficients for a much large range of orientations such as those contained within Cermak and Peterka (1979). This should be done in order to get a better understanding of the orientations at which certain coefficients are accurately predicted. This could provide insight as to what specifically this method has issues with such as, for example, orientations which exhibit vortex formation along the heliostat edge.

## References

- AIM<sup>2</sup>. (2014). *Particle Image Velocimetry (PIV)*. Retrieved 11 05, 2014, from <http://aim2.dlr.de/measurement-techniques/particle-image-velocimetry-piv/index.html>
- Bezuidenhout, D. (2014). *Heliostat flow measurements, final year project*. Stellenbosch: Department of Mechanical and Mechatronic Engineering, Stellenbosch University.
- Cermak, J. E. and Peterka, J. A. (1979). *Single heliostat wind-tunnel load verification test*. California: McDonnell Douglas Astronautics Company.
- Environment, UM School of Natural Resources & Environment. (2010). *Renewable Energy in the California Desert*. Retrieved 11 02, 2014, from <http://webservices.itcs.umich.edu/drupal/recd/?q=node/155>
- Fage, A. and Johansen, F. C. (1927). On the flow of air behind an inclined flat plate. *Proceedings of the Royal Society, London, Series A, 116*, 170-197.
- Fail, R., Lawford, J. A. and Eyre, R. C. (1959). *Low-speed experiments on the wake characteristics of flat plates normal to an air stream*. London: Ministry of supply.
- FLUENT™. (2013). ANSYS FLUENT™ Theory guide. Pennsylvania: ANSYS Inc.
- FLUENT™. (2013). ANSYS FLUENT™ User guide. Pennsylvania: ANSYS inc.
- Franke, J., Hirsch, C., Jensen, A. G., Krüs, H. W., Schatzmann, M., Westbury, P. S., Miles, S., Wisse, J. A. and Wright, N. G. (2004). Recommendations on the use of CFD in wind engineering. *COST, 14*, C1.
- IRENA. (2012). *Renewable Energy Cost Analysis - Concentrating Solar Power*. Retrieved 10 06, 2013, from IRENA: <http://www.irena.org/menu/index.aspx?mnu=Subcat&PriMenuID=36&CatID=141&SubcatID=233>
- Irwin, J. (1967). A theoretical variation of the wind profile power-law exponent as a function of surface roughness and stability. *Atmospheric Environment, 13*(1), 191-194.
- Kim, S.-E. and Boysan, F. (1999). Application of CFD to environmental flows. *Journal of Wind Engineering and Industrial Aerodynamics, 81*, 145-158.
- Kolb, G., Jones, S., Donnelly, M., Gorman, D., Thomas, R., Davenport, R., Lumia, R. (2007). *Heliostat cost reduction study*. Albuquerque: Sandia National Laboratories.
- Lee, S. (1997). Unsteady aerodynamic force prediction on a square cylinder using k-ε turbulence models. *Journal of Wind Engineering and Industrial Aerodynamics, 67 & 68*, 79-90.

- Matty, R. (1979). *Vortex shedding from square plates near a ground plane, masters thesis*. Texas: Texas Tech University.
- Menter, F. R. (1992). *Improved two-equation k- $\omega$  turbulence models for aerodynamic flows*. California: NASA.
- Mentor Graphics. (2010). Retrieved 05 06, 2014, from [http://s3.mentor.com/public\\_documents/whitepaper/resources/mentorpaper\\_57791.pdf](http://s3.mentor.com/public_documents/whitepaper/resources/mentorpaper_57791.pdf)
- Murakami, S. (1993). Comparison of various turbulence models applied to a bluff body. *Journal of Wind engineering and Industrial Aerodynamics*, 46 & 47, 21-36.
- Murakami, S. (1998). Overview of turbulence models applied in CWE-1997. *Journal of Wind Engineering and Industrial Aerodynamics*, 74-76, 1-24.
- Naeeni, N. and Yaghoubi, M. (2007). Analysis of wind flow around a parabolic collector (1) fluid flow. *Renewable Energy*, 32(11), 1898-1916.
- National Instruments. (2013). *3D Imaging with NI LabVIEW*. Retrieved 11 09, 2014, from <http://www.ni.com/white-paper/14103/en/>
- Peterka, J. A., Tan, Z., Bienkiewicz, B. and Cermak, J. E. (1987). *Mean and peak wind load reduction on heliostats*. Colorado: Solar Energy Research Institute.
- Peterka, J. A., Tan, Z., Bienkiewicz, B. and Cermak, J. E. (1988). *Wind loads on heliostats and parabolic dish collectors*. Colorado: Solar Energy Research Institute.
- Peterka, J. and Derickson, R. (1992). *Wind load design methods for ground-based heliostats and parabolic dishes*. Colorado: Sandia National Laboratories.
- Peterka, J., Hosoya, N., Bienkiewicz, B. and Cermak, J. (1986). *Wind load reduction for heliostats*. Colorado: Solar Energy Research Institute.
- Pfahl, A. and Uhlemann, H. (2011). Wind loads on heliostats and photovoltaic trackers at various Reynolds numbers. *Journal of Wind Engineering and Industrial Aerodynamics*, 99(9), 964-968.
- Piomelli, U. (2006). *Q-criterion for flow visualization of turbulence*. Retrieved 29 05, 2014, from <http://www.terpconnect.umd.edu/~lbravo/docs/Q-criterion.pdf>
- Richards, P. and Hoxey, R. (1993). Appropriate boundary conditions for computational wind engineering models using the k- $\epsilon$  turbulence model. *Journal of Wind Engineering and Industrial Aerodynamics*, 46-47, 145-153.
- Rodi, W. and Bosch, G. (1998). Simulation of vortex shedding past a square cylinder with different turbulence models. *International Journal for Numerical Methods in Fluids*, 28, 601-616.

- Rodi, W. and Lakehal, D. (1997). Calculation of flow past a surface-mounted cube with two-layer turbulence models. *Journal of Wind Engineering and Industrial Aerodynamics*, 67 & 68, 65-78.
- Sagaut, P. (2004). *Large eddy simulation for incompressible flows* (Second ed.). Berlin: Springer.
- Sment, J. and Ho, C. K. (2012). *Characterization of wind velocity distributions within a full-scale heliostat field*. Albuquerque: Sandia National Laboratories.
- Symscape. (2013). *Polyhedral, tetrahedral, and hexahedral mesh comparison*. Retrieved 10 29, 2014, from <http://www.symscape.com/polyhedral-tetrahedral-hexahedral-mesh-comparison>
- Verma, V., Singh, R. K. and Gosh, A. K. (2010). Evaluation of wind load on heliostat, *Proceedings of the 37<sup>th</sup> National and 4<sup>th</sup> International conference on Fluid Mechanics*
- Versteeg, H. K. and Malasekera, W. (2007). What is CFD? In *An Introduction to Computational Fluid Dynamics* (p. 2). Essex: Pearson Education Limited.
- Wilcox, D. C. (1994). 4.3 Two-equation models. In *Turbulence Modelling for CFD* (p. 84). California: DCW Industries.
- Wu, Z. and Wang, Z. (2008). Numerical study of wind load on heliostat. *Progress in Computational Fluid Dynamics*, 8(7/8), 503-509.
- Wu, Z., Gong, B., Wang, Z., Li, Z. and Zang, C. (2010). An experimental and numerical study of the gap effect on wind load on heliostat. *Renewable Energy*, 35(4), 797-806.
- Yakhot, V., Orszag, S. A., Thangam, S., Gatski, T. B. and Speziale, C. G. (1992). Development of turbulence models for shear flows by a double expansion technique. *Physics of Fluids*, 7(7), 1510-1520.
- Yin, M., Shi, F. and Xu, Z. (1996). Renormalization group based k- $\epsilon$  turbulence model for flows in a duct with strong curvature. *International Journal of Engineering Science*, 34(2), 243-248.

## Appendix A: Domain Width and Height

In order to ensure that the selection of the domain size was correct for the simulations conducted with the flat plate and heliostat, in sections 4 and 5 respectively, the streamlines were checked in a vertical and horizontal plane containing the heliostat. This was to check that there was no interference at the side and top wall boundaries. In the case that the streamlines are not squeezed near the wall boundaries, it would be evident that there is no interference between the flow and the boundary, thus showing that the domain size was valid. Below are some examples of the streamlines for the flat plate flow, as well as the heliostat simulation and a picture from Cermak and Peterka (1979) on which the heliostat domain size was selected.

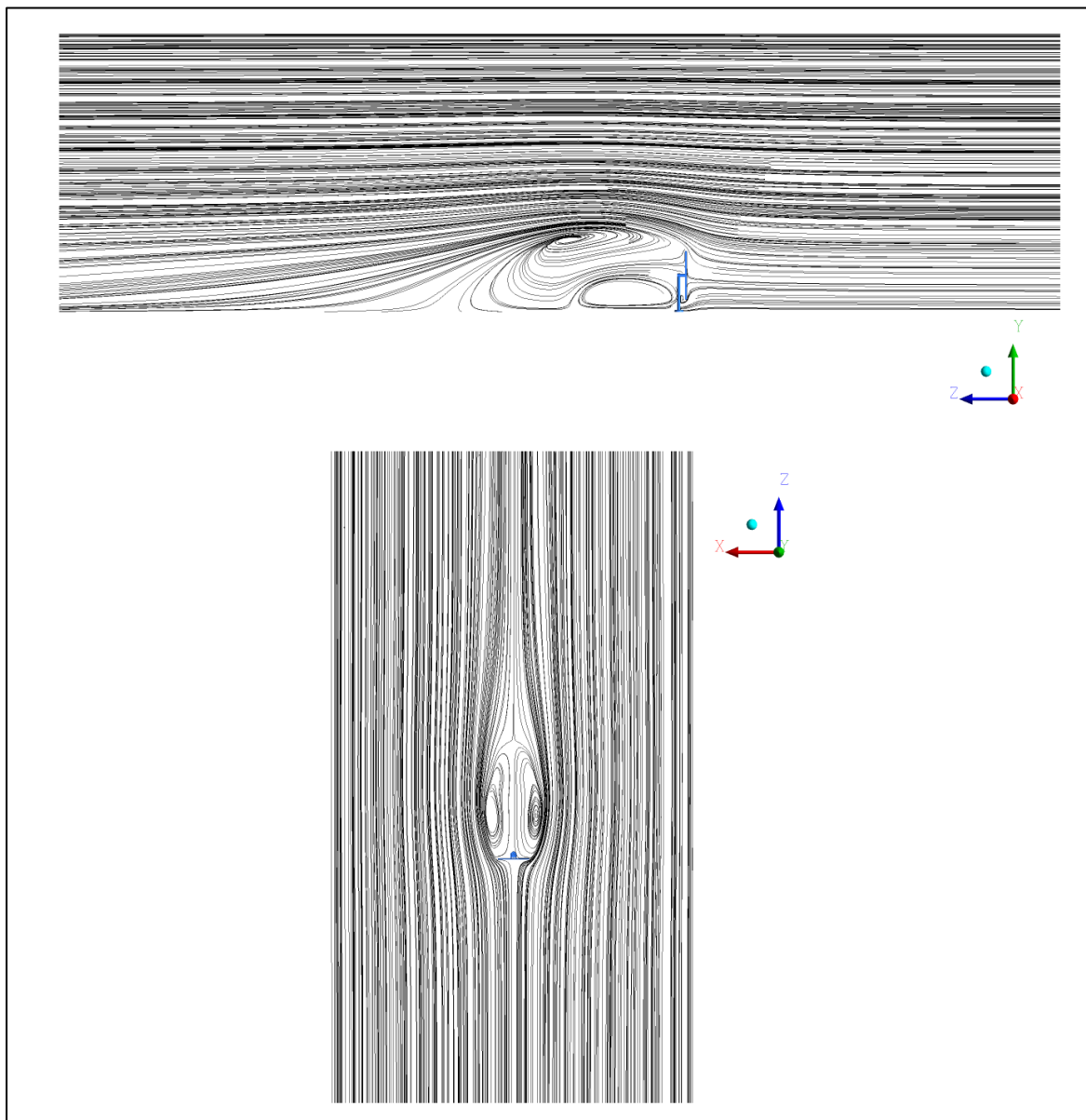


Figure A-1: Streamlines for flat plate simulation in vertical (top) and horizontal (bottom) planes

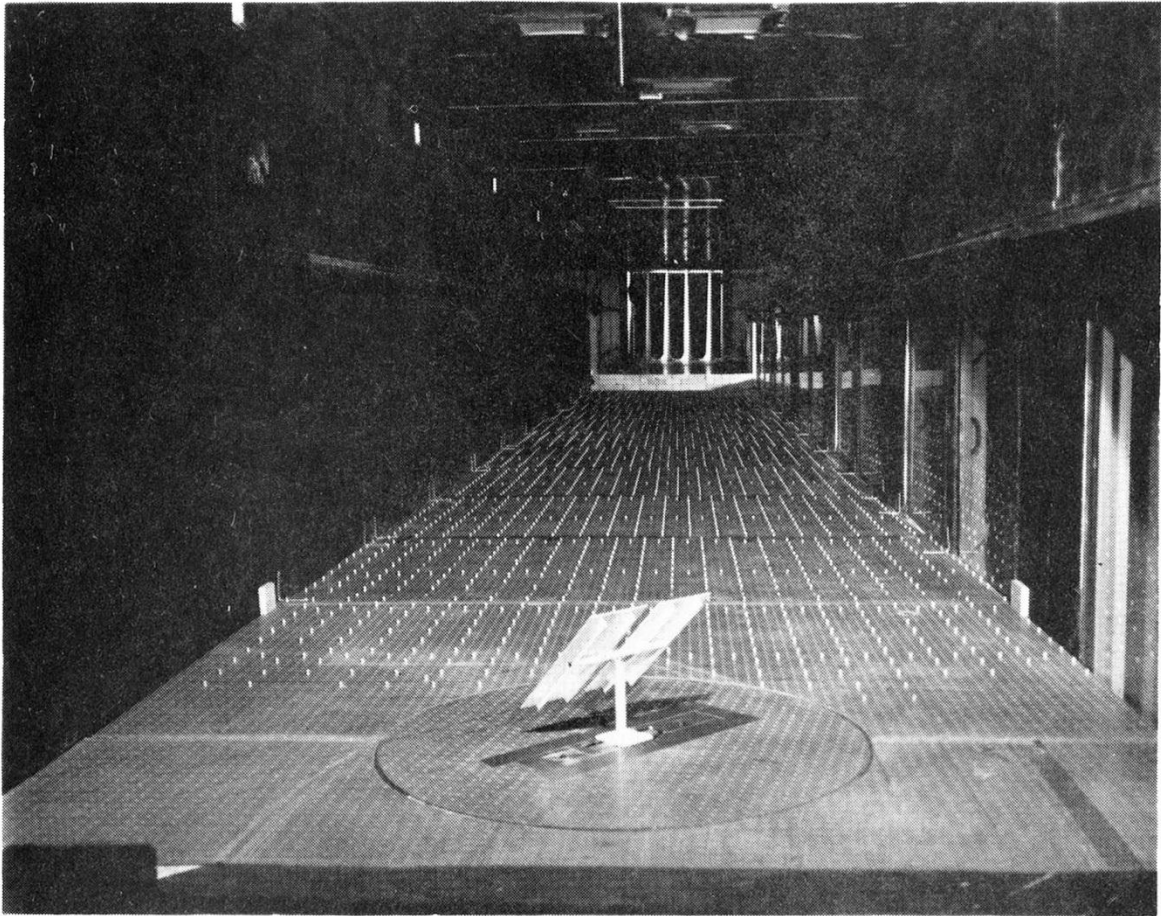


Figure A-2: Picture of heliostat from Cermak and Peterka (1979) within wind tunnel

Further to this, a contour plot of the pressure along the side, top and rear faces was checked in order to ensure that the flow about the heliostat had little or no interaction with these faces. The contour plot generated for the perpendicular and tilted heliostats can be seen in Figure A-5 and Figure A-6 respectively.

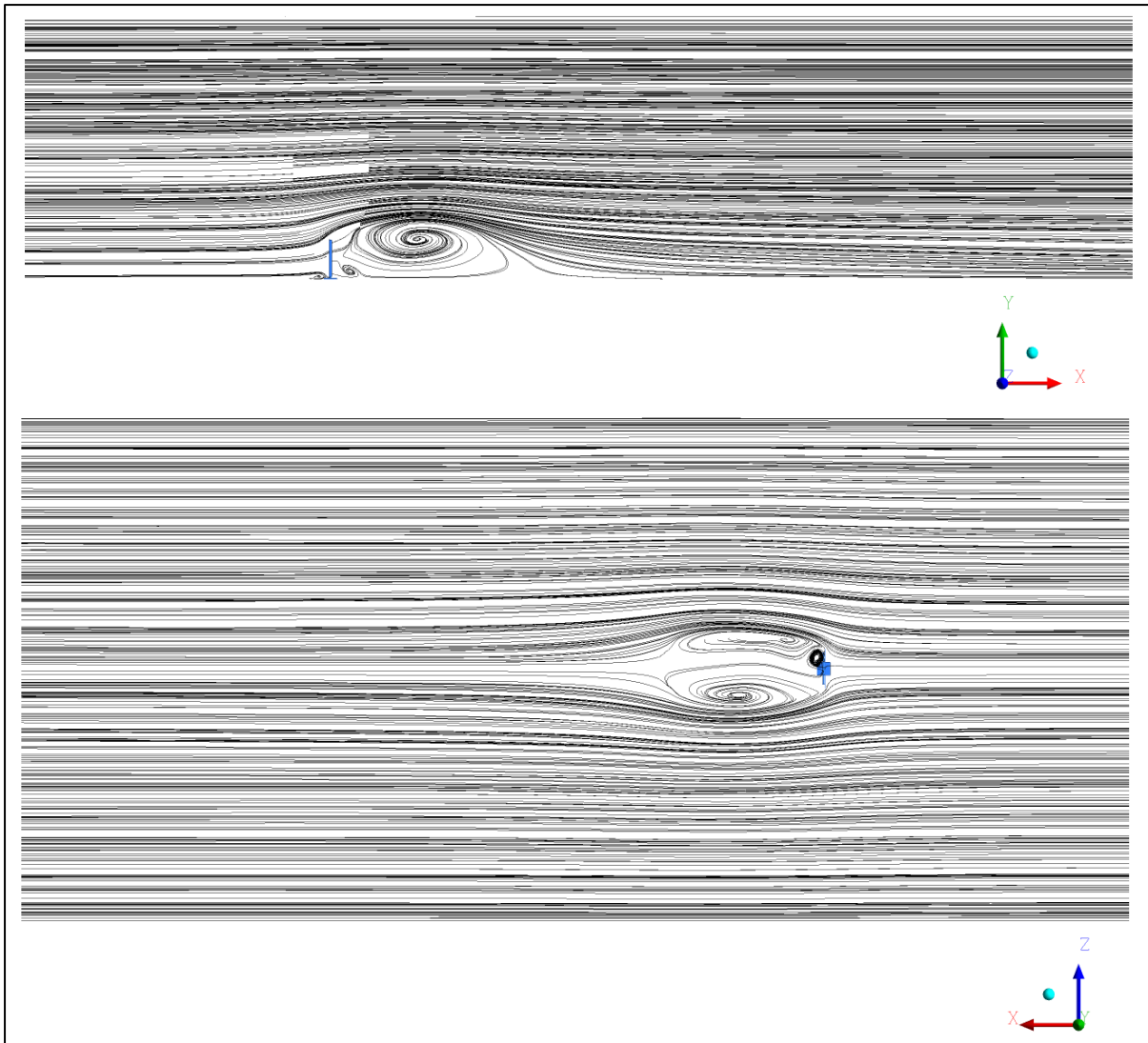


Figure A-3: Streamlines for perpendicularly orientated heliostat in vertical (top) and horizontal (bottom) planes

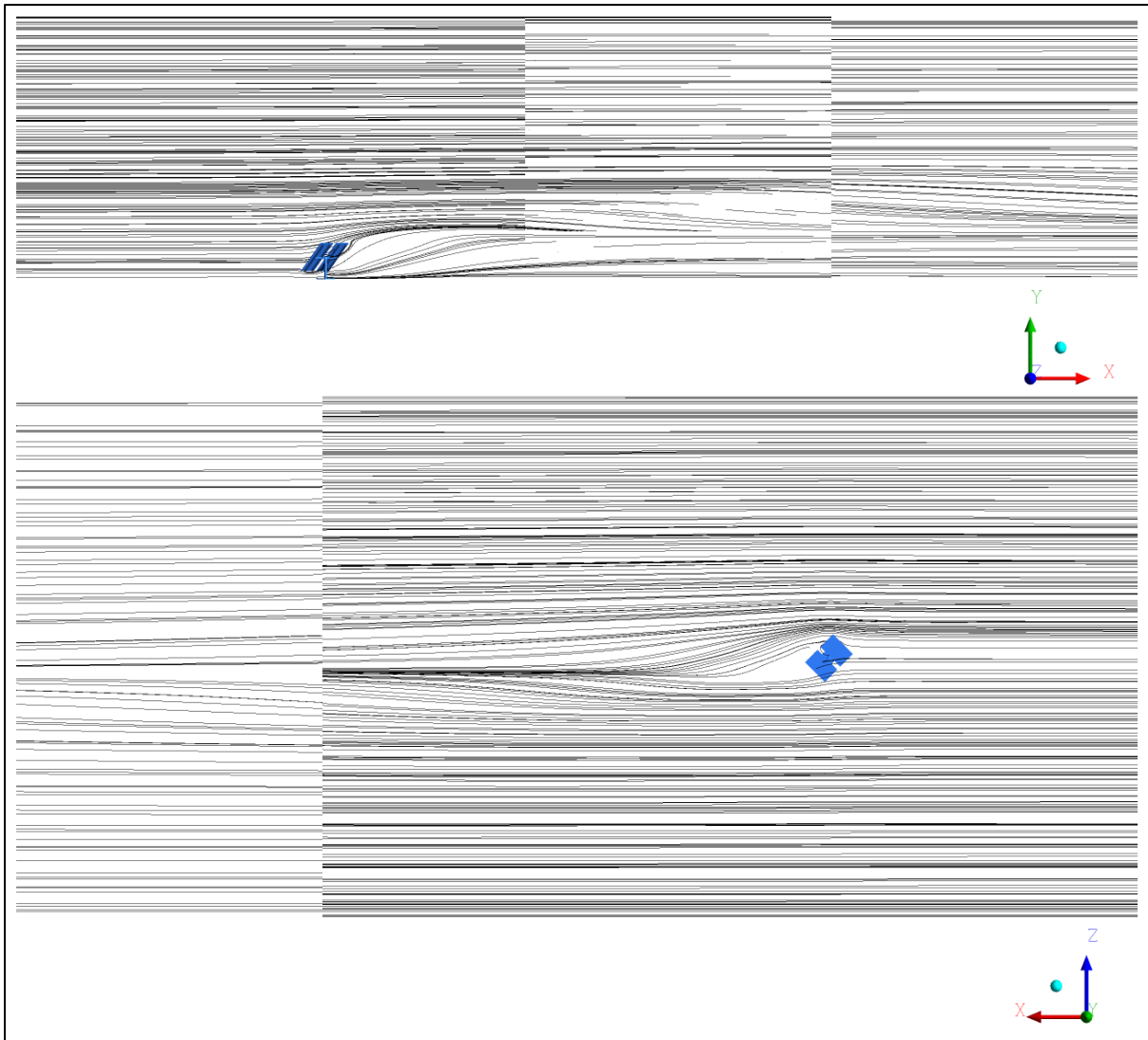


Figure A-4: Streamlines for tilted heliostat in vertical (top) and horizontal (bottom) planes

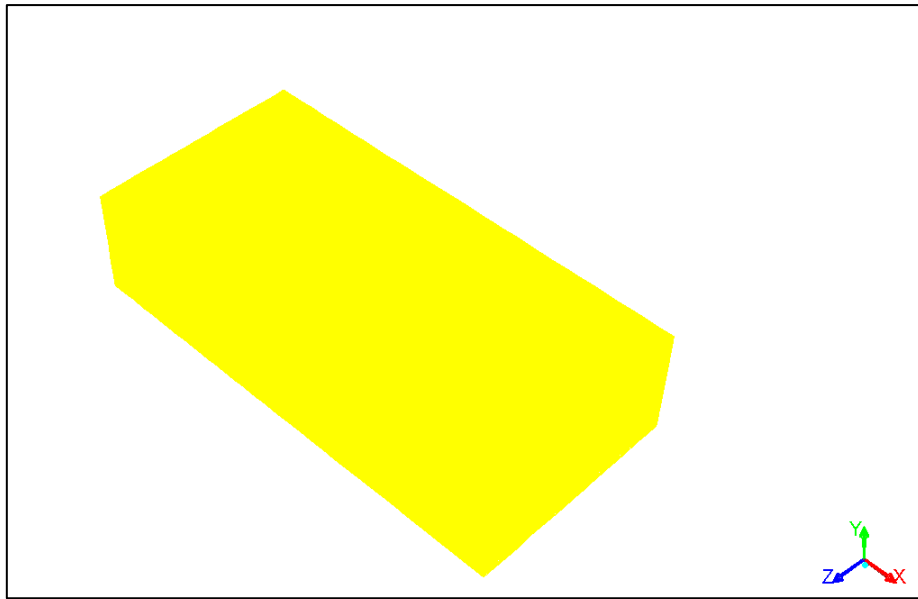


Figure A-5: Pressure contour along the side, top and rear domain walls perpendicular heliostat

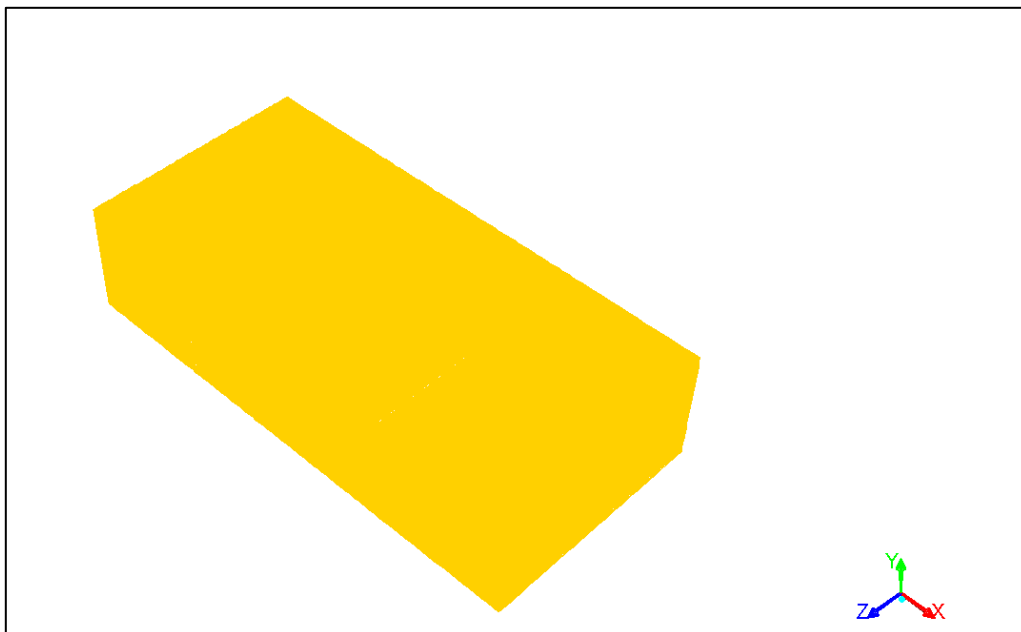


Figure A-6: Pressure contour along the side, top and rear domain walls tilted heliostat

## Appendix B: Iso-surfaces at Different Time Steps

Considering the transient nature of the simulation of flow past a perpendicular flat plate, the iso-surface of the  $q$ -criterion has been plotted for various time steps for this simulation. The actual time of the simulations at the point when the images are taken has been omitted as the purpose of this section is purely to illustrate that the flow is indeed transient. This is seen by the large differences in the plotted iso-surface at different times in the flow.

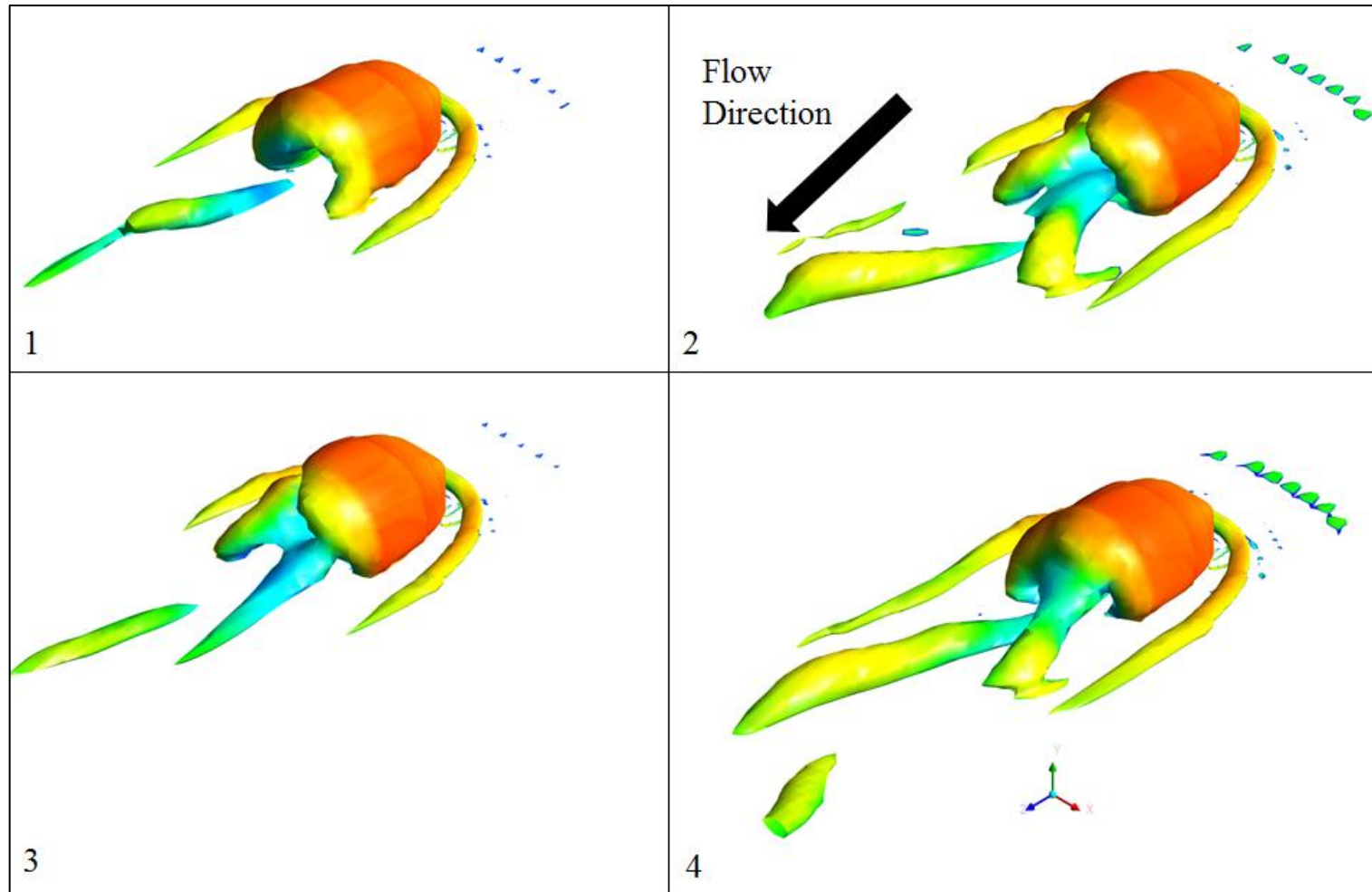


Figure B-1: Iso-surface of q-criterion for various time steps with the RNG k- $\epsilon$  model

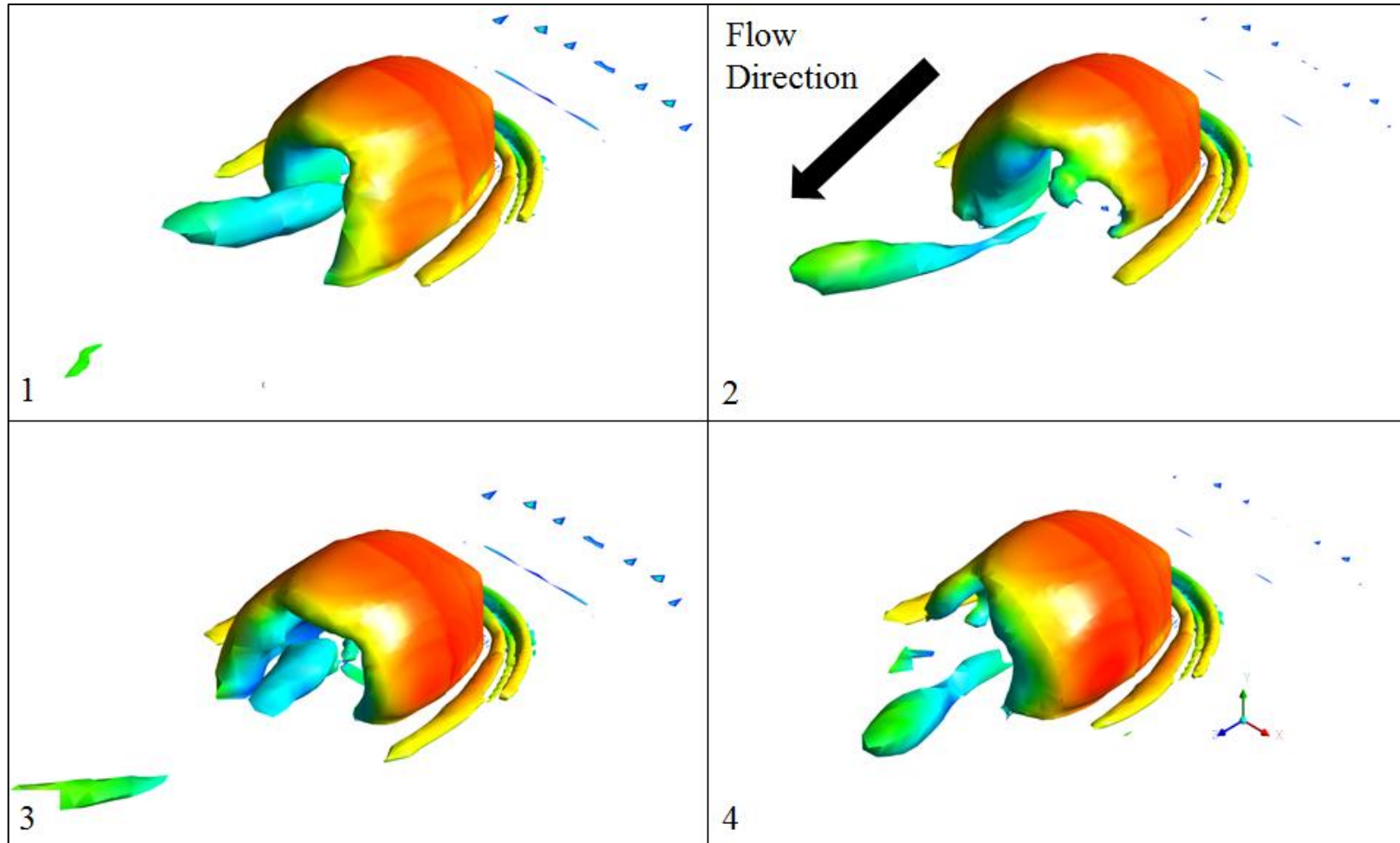


Figure B-2: Iso-surface of q-criterion for various time steps with the SST  $k-\omega$  model

## Appendix C: Mesh Independency Study for Heliostats

The following appendix contains the details and results obtained with consecutively finer meshes for a heliostat orientated at 45° in both the azimuth and elevation angles. The cell counts and load coefficients for each consecutive mesh can be seen in Table C-1: Cell count and load coefficient for different mesh densities. For a visualisation of each mesh please see Figure 5-7.

Table C-1: Cell count and load coefficient for different mesh densities

Mesh density	Cell count	Drag	Lift	Overturning moment
Coarse	1 503 203	0.567	-0.672	-0.208
Medium	1 926 275	0.572	-0.674	-0.208
Fine	2 185 853	0.556	-0.673	-0.208
Finest	3 643 819	0.549	-0.663	-0.205

From Table C-1 it can be seen that the results for the overturning moment and lift do not change significantly across all the meshes tested. The percentage change in the results from the fine to the finest mesh is around 1.2 % for drag, 1.5 % for lift and 1.4 % for the overturning moment. This small change in the results at this point would point to the results essentially being mesh independent at this point considering a change of less than 2 % for the significant variables. Whilst the changes between these variables at earlier meshes may have been smaller in some cases; by having the computational capacity available and considering the simulation run time of less than a day, it was decided that testing at the finest mesh could be done with no detrimental effect. Testing at the finest mesh, however, did push the simulation run time over a day at which point it was decided that for the end result of simple load coefficients for a steady state case any longer would not be desirable. Thus, considering the extended simulation run time and small change in result from the previous mesh, this was the point at which the results were considered mesh independent.

## Appendix D: PIV Safety Report

The following example of a safety report had to be completed and signed before access to the wind tunnel during PIV operation was allowed.

### Responsible academic staff

The responsible personnel for Particle Image Velocimetry (PIV) experiments are the following:

Laser safety officer	D. Roux
Academic staff member	Prof. H.C.R Reuter Pro. T.M. Harms
Laboratory supervisor	C. Zietsman
Authorised laser and PIV operators	E.C. Joubert Dr. J.van der Spuy D. Roux

### Experimental description

An investigation into the flow around a heliostat is to be conducted in which the use of (PIV) will be utilised in order to evaluate the velocity distribution in a plane in the wake of the heliostat. The flow field will be evaluated for the heliostat a few orientations, the most prominent of which are; perpendicular to the flow and at 45 degrees to the ground and oncoming flow. Other tests include an upright heliostat at varying angles to the oncoming flow as well other tilt angles for which the time available for tests as well as shading issues will be the limiting factors in the number of orientations tested. The flow field aligned with a plane parallel to the side walls of the wind tunnel is of interest as well as plane parallel to the ground plane aligned, depending on the heliostat orientation and the associated shading issues. A Reynolds number in the region of  $10^5$  based on the chord length of the heliostat hopes to be achieved in order to achieve Reynolds number independence to full scale, real world conditions. This would translate to a test speed of around 60 m/s. The tests conducted will also be used to validate CFD simulations conducted which means that that not achieving a Reynolds number of  $10^5$  is not a major issue as the wind speed used in CFD simulations can be easily changed.

The experimental setup will consist of a heliostat model developed by Danica Bezuidenhout as part of her final year project which will be designed to be mounted in the wind tunnel and also allows for load testing at a later stage. Other components which make up the PIV system include the laser, traverse system, computer, cameras and particle seeder. The laser will be mounted atop the wind tunnel with the cameras mounted on the side and the particle seeded being upstream of the heliostat model. The experiments are planned to be conducted over the

period of 26<sup>th</sup> of June to the 4<sup>th</sup> of July for the PIV testing. An example of a single orientation with the PIV plane being parallel to the side walls of the heliostat is shown in figure 1.

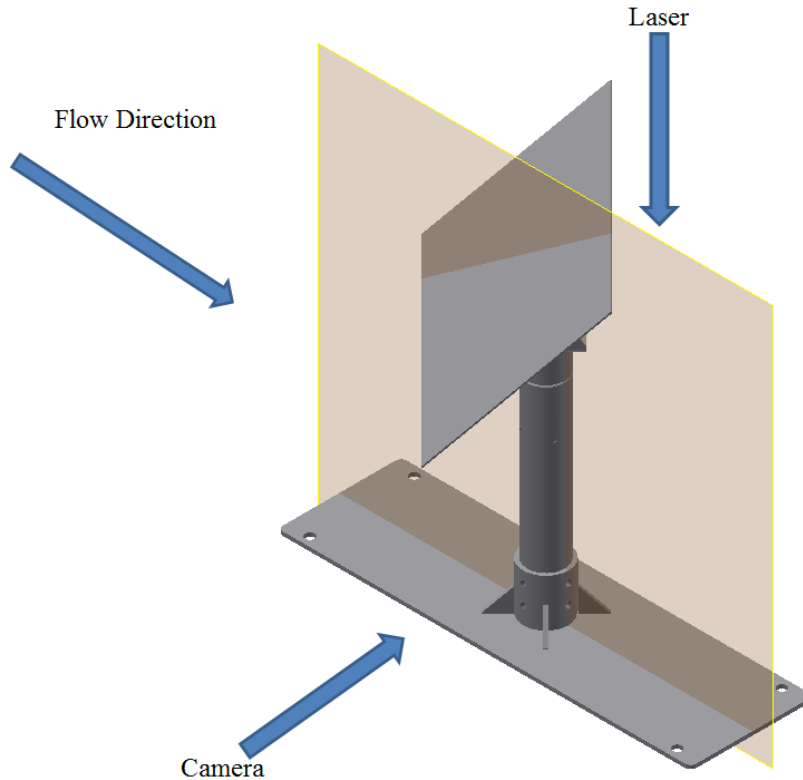


Figure C-1: Sketch of test orientation

### Risk assessment

When working with the PIV equipment there are various risks involved both to equipment as well as to the personnel involved in the testing. These risks as well as precautions to be taken against them are summarised in the following tables. First, the personnel hazards will be addressed:

Table D-1: Personnel risks

<b>Risk</b>	<b>Precaution</b>
Laser specific risks <ul style="list-style-type: none"> <li>• Direct laser light</li> <li>• Reflected laser light</li> <li>• Dispersed laser light</li> </ul>	<ul style="list-style-type: none"> <li>• Ensure beam is oriented at least perpendicular to personnel</li> <li>• Ensure use of safety goggles at all times</li> <li>• Use of screens to prevent direct or reflected laser light from harming personnel</li> <li>• Where possible, paint surfaces matte black to ensure absorption of laser light</li> <li>• Ensure restricted access when the laser is active through the use of warning tape</li> <li>• Ensure that the beam is not at eye level</li> <li>• Further; follow the operating and safety conditions</li> </ul>

	<p>in the following section</p> <ul style="list-style-type: none"> <li>• Ensure the materials and surfaces are non-toxic and no flammable</li> <li>• Always use the laser at the minimum required power to reduce risk of damages</li> </ul>
<p>Equipment specific risks</p> <ul style="list-style-type: none"> <li>• Traverse movement</li> <li>• Power cables</li> <li>• Tripping hazards</li> </ul>	<ul style="list-style-type: none"> <li>• Ensure all personnel are clear of electrical cables and the cables are sufficiently long for traverse movement</li> <li>• Ensure traverse pathway is clear of objects</li> <li>• Ensure cables are out of the way, or if not possible, secured to the ground through tape</li> <li>• Ensure any un-needed objects are out of the way and the lab has only what is needed during experimentation</li> </ul>
<p>Unauthorised personnel</p>	<ul style="list-style-type: none"> <li>• Restrict lab access through locking the doors during experimentation</li> <li>• Ensure all relevant parties are notified of the tests</li> <li>• Use safety tape or signs to indicate laser operation</li> </ul>

Now the equipment hazards need to be addressed:

Table D-2: Equipment risks

<p>Laser specific risks</p> <ul style="list-style-type: none"> <li>• Direct laser light</li> <li>• Reflected laser light</li> <li>• Dispersed laser light</li> </ul>	<ul style="list-style-type: none"> <li>• Ensure surfaces and materials used are non-reactive to the laser light</li> <li>• Conduct a full beam path analysis to ensure correct placement of screens to reduce the fire hazard of the class 4 laser</li> <li>• Again ensure surfaces are painted matte black to reduce the laser's effect on other equipment</li> </ul>
<p>Equipment specific risks</p> <ul style="list-style-type: none"> <li>• Traverse movement</li> <li>• Model stability</li> </ul>	<ul style="list-style-type: none"> <li>• Ensure the traverse path is unobstructed</li> <li>• Ensure cables are sufficiently long and are not in the way of the path</li> <li>• Ensure the heliostat model is properly secured to prevent damage to the tunnel walls</li> <li>• Ensure all moving parts of the heliostat are fully locked in position</li> <li>• Ensure laser and other moving parts are fully secure</li> </ul>
<p>Unauthorised personnel</p>	<ul style="list-style-type: none"> <li>• Restrict lab access to authorised and oriented personnel only</li> <li>• Remove laser key and dongle to avoid unauthorised use</li> <li>• Lock doors to prevent unauthorised personnel from entering</li> <li>• Ensure all equipment is turned off when leaving the lab</li> </ul>

## Operating and safety conditions

The following list is essentially a checklist of procedures which must be followed before the experiment can be considered safe to proceed.

1. Ensure only authorised personnel are present in the lab before starting experimentation.
2. Ensure the doors are locked to prevent unauthorised personnel from entering the laboratory.
3. Ensure that the all components of the PIV system are securely mounted and that the traverse system is under its weight and moment limits and that the traverse path is unobstructed.
4. Inform all personnel in the lab that the laser is about to go live and that everyone has access to safety goggles and that everyone present is wearing them before the laser goes live.
5. Ensure all screens are correctly positioned to avoid contact with the laser beam.
6. Ensure that no personnel are in line with either the direct or reflected laser beam before switching it on by carefully considering the beam path before testing.
7. Keep the emergency switch close at hand in the event of an incident.
8. Never work alone in the lab.
9. Remove some key operational component, such as the key, from the PIV system when not in use to prevent accidentally powering on the system.
10. Use minimum required laser power, especially at start up and during path analysis.

## Authorised personnel during testing

The following are the allowed personnel during the PIV testing of a heliostat, with the presence of at least D. Roux or E.C. Joubert being required before any experimentation can be done:

- D. Roux (laser safety officer)
- E.C. Joubert (supervisor for D. Bezuidenhout)
- D. Bezuidenhout (final year student)
- A.V. Hariram (masters student under T. Harms)

## Declaration

I, A.V. Hariram, the undersigned student, hereby declare that I have read the “Particle Image Velocimetry System Safety” document and fully understand the risks involved in using the PIV system which includes a very dangerous Class 4 laser. I understand that I am responsible for my own safety. I declare that the information given in this report is correct and that the risk assessment regarding personnel as well as equipment safety was done to the best of my knowledge. I agree to follow the safety measures and checklist mentioned in this report at all times. I agree to use the equipment in a safe and responsible manner as was outlined in the “Particle Image Velocimetry Safety” document.

.....

Student signature

## Approval

Supervisor	T.M. Harms	.....
Laboratory supervisor	C. Zietsman	.....
Academic staff member	H.C.R. Reuter	.....
Academic staff member	T.M. Harms	.....
Laser Safety Officer	D. Roux	.....

## Appendix E: Photographs of Experimental Setup

Some photographs of the experimental setup have been included here to provide some insight into the experimental setup.

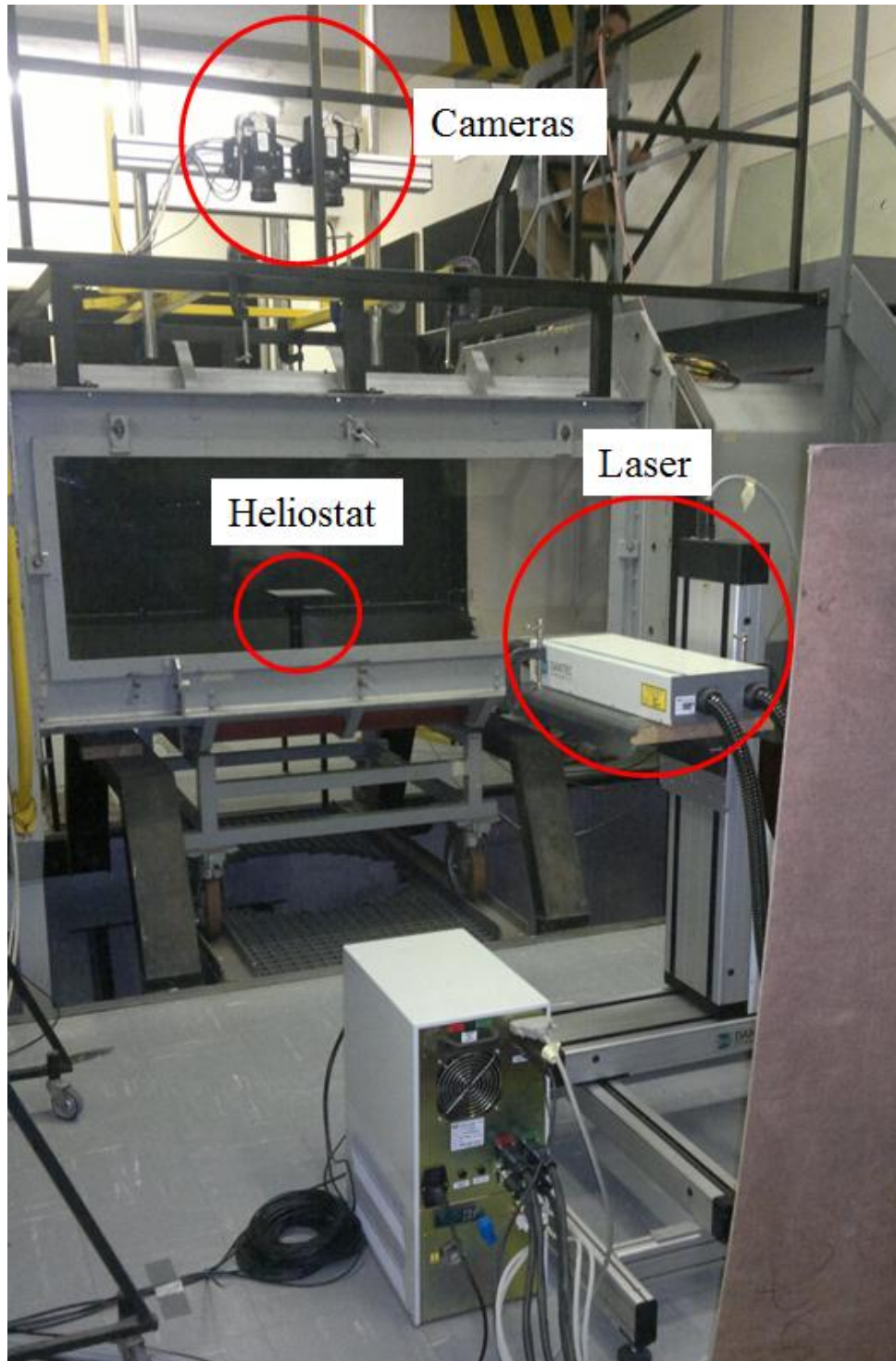


Figure E-1: Location of components for horizontal plane testing for Bezuidenhout (2014)

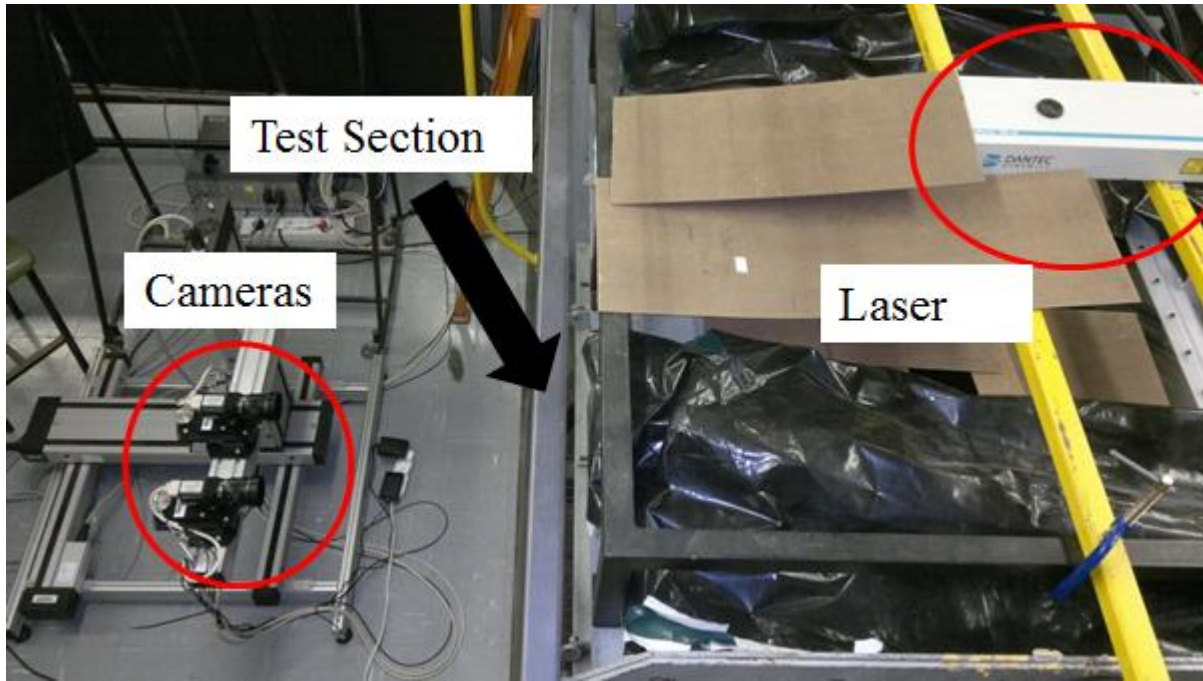


Figure E-2: Location of components for vertical plane used in thesis



Figure E-3: Picture of tilted heliostat within wind tunnel

Appendix F: Dimensioned Geometry

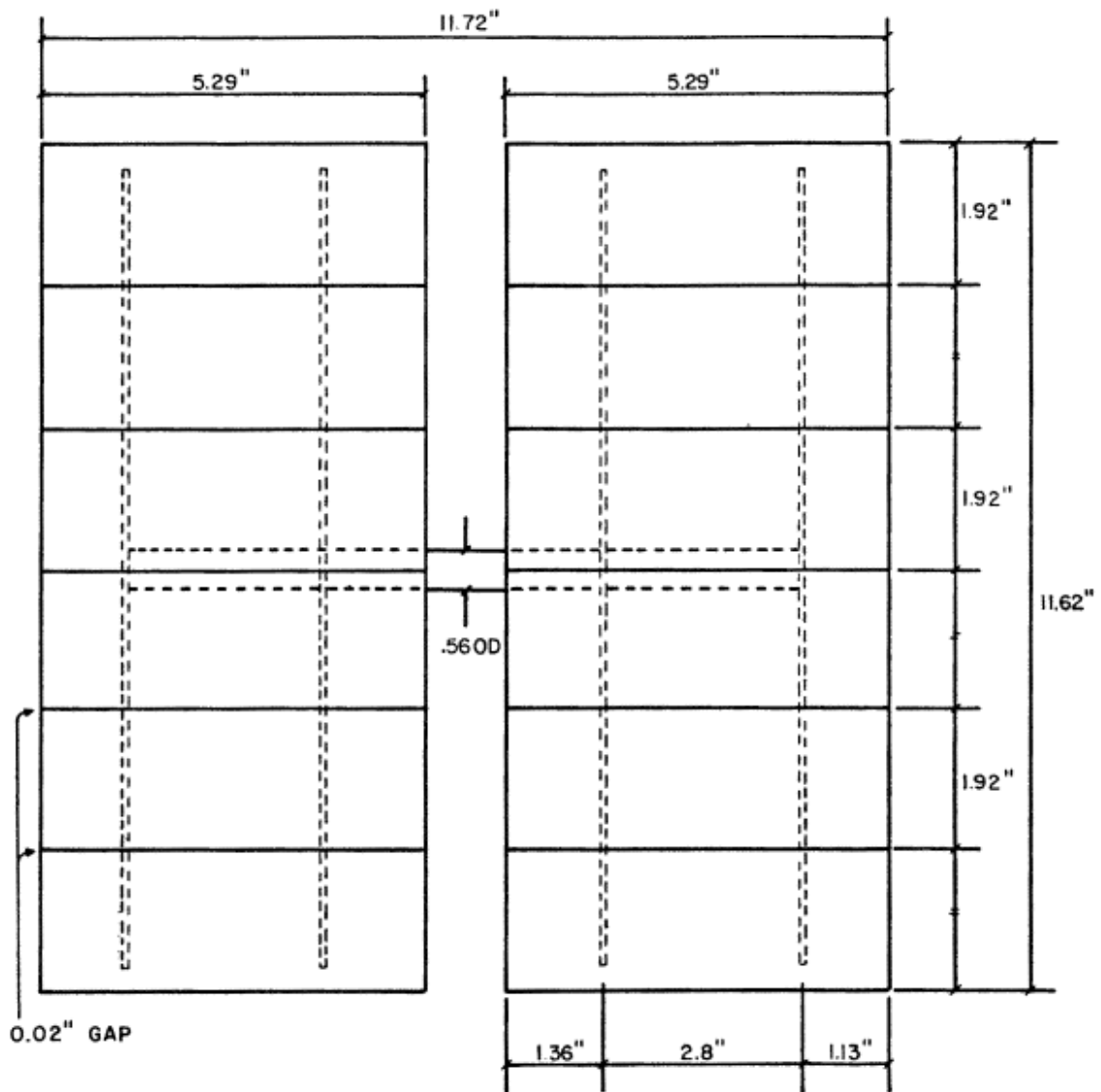


Figure F-1: Heliostat surface dimensions (Cermak and Peterka, 1979)

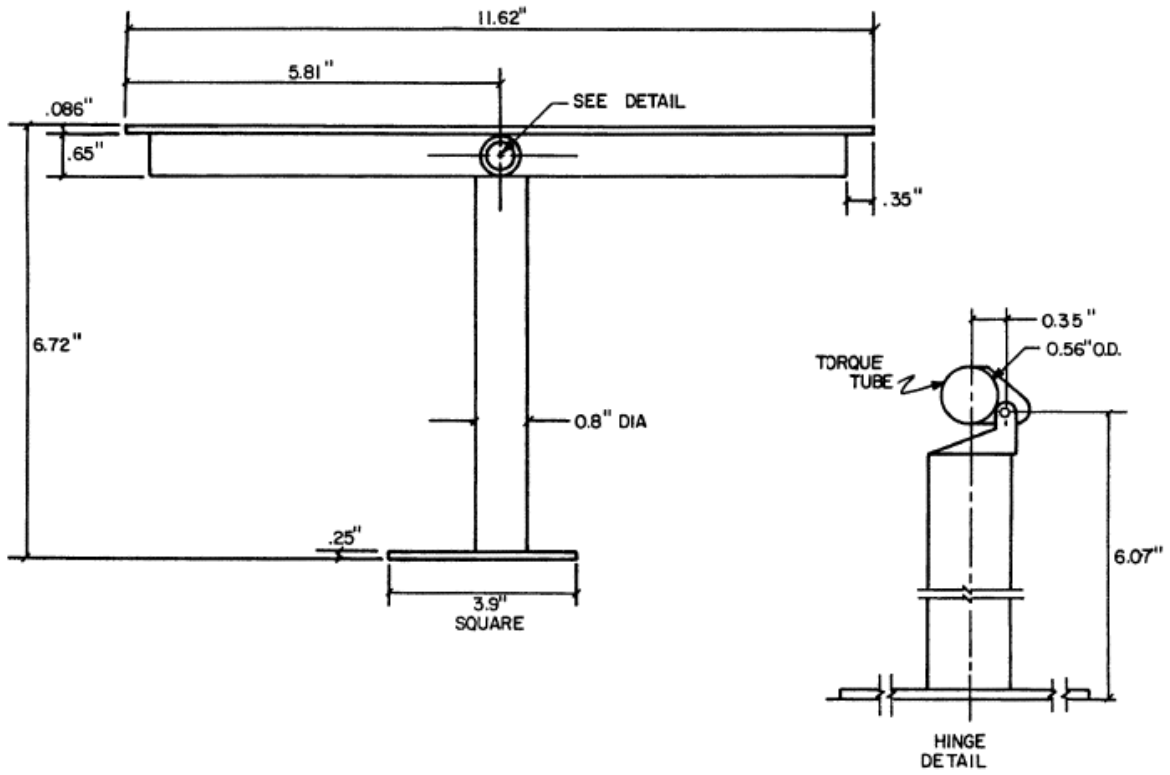


Figure F-2: Heliostat structure dimensions (Cermak and Peterka, 1979)

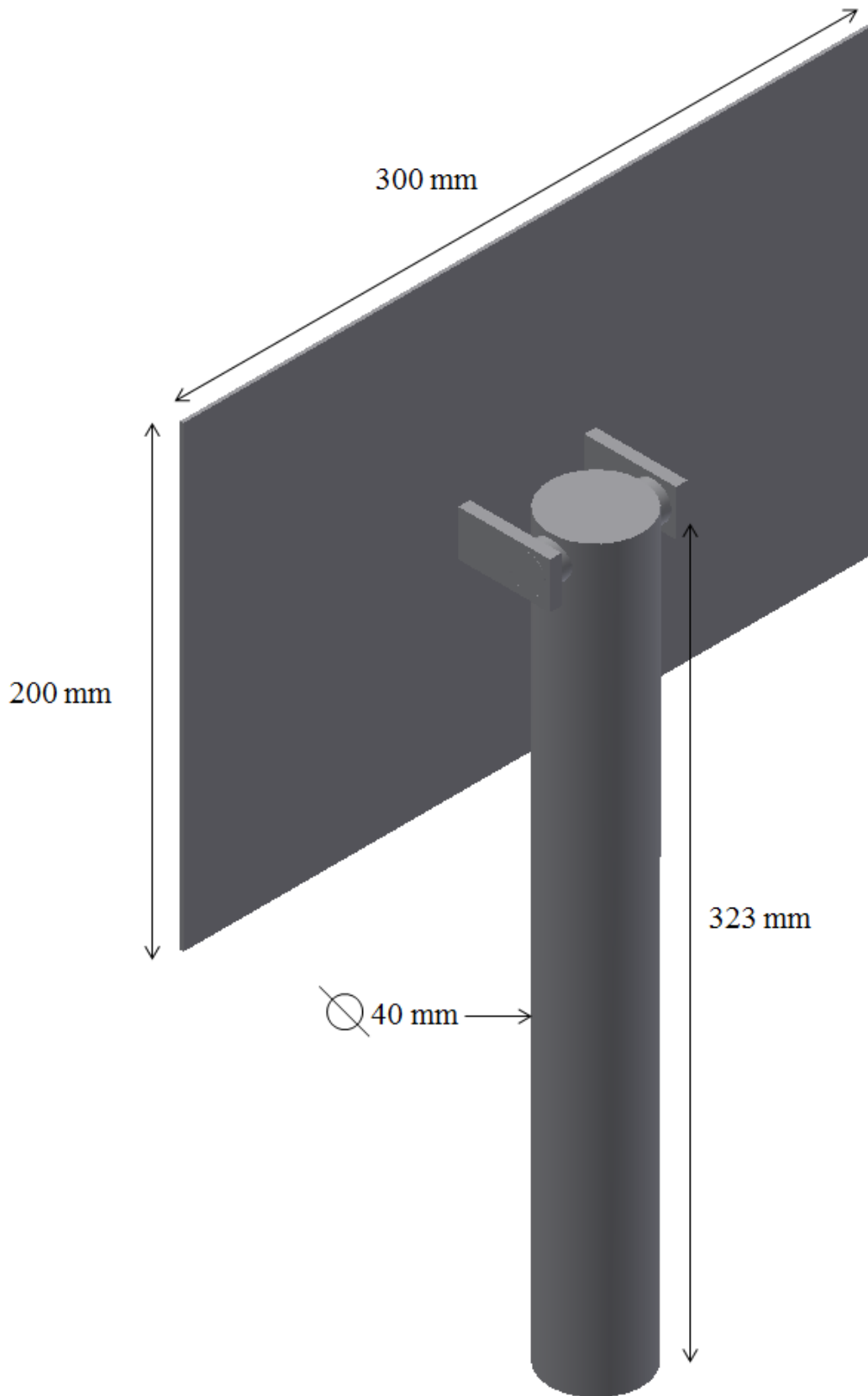


Figure F-3: Major PIV heliostat dimensions

## Appendix G: Details of Velocity Profile Locations

The location of the profiles mentioned in section 6.4.1 had been referenced to various locations of the experimental heliostat in their respective PIV photos. This had been done as the profiles had to be sampled from areas containing good data and one way to compare them to the simulation results was to determine their location relative to the heliostat and to then sample the equivalent location from the simulation. The reference points for each of these locations are shown in Figure G-1 and Figure G-2. The location of the sampling lines relative to these reference points is given in Table G-1.

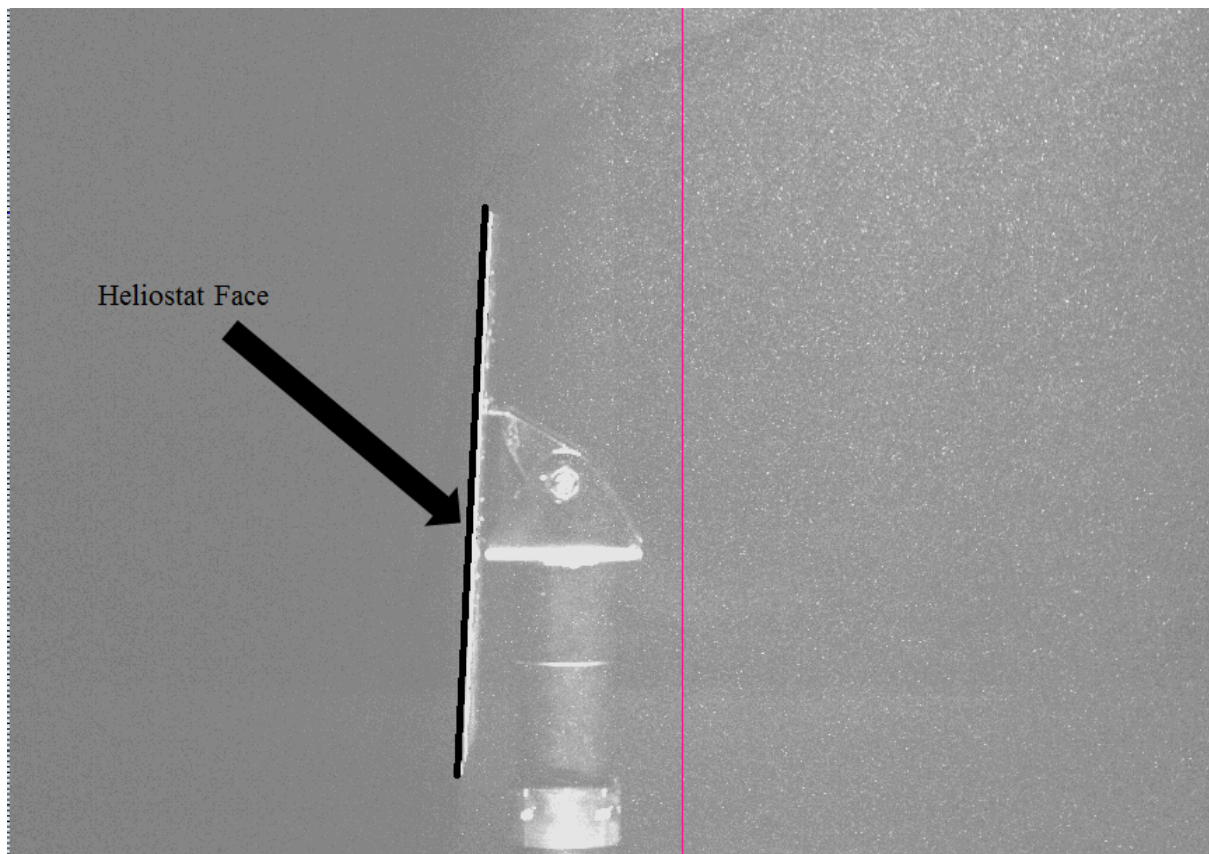


Figure G-1: Reference points for perpendicular heliostat in offset plane

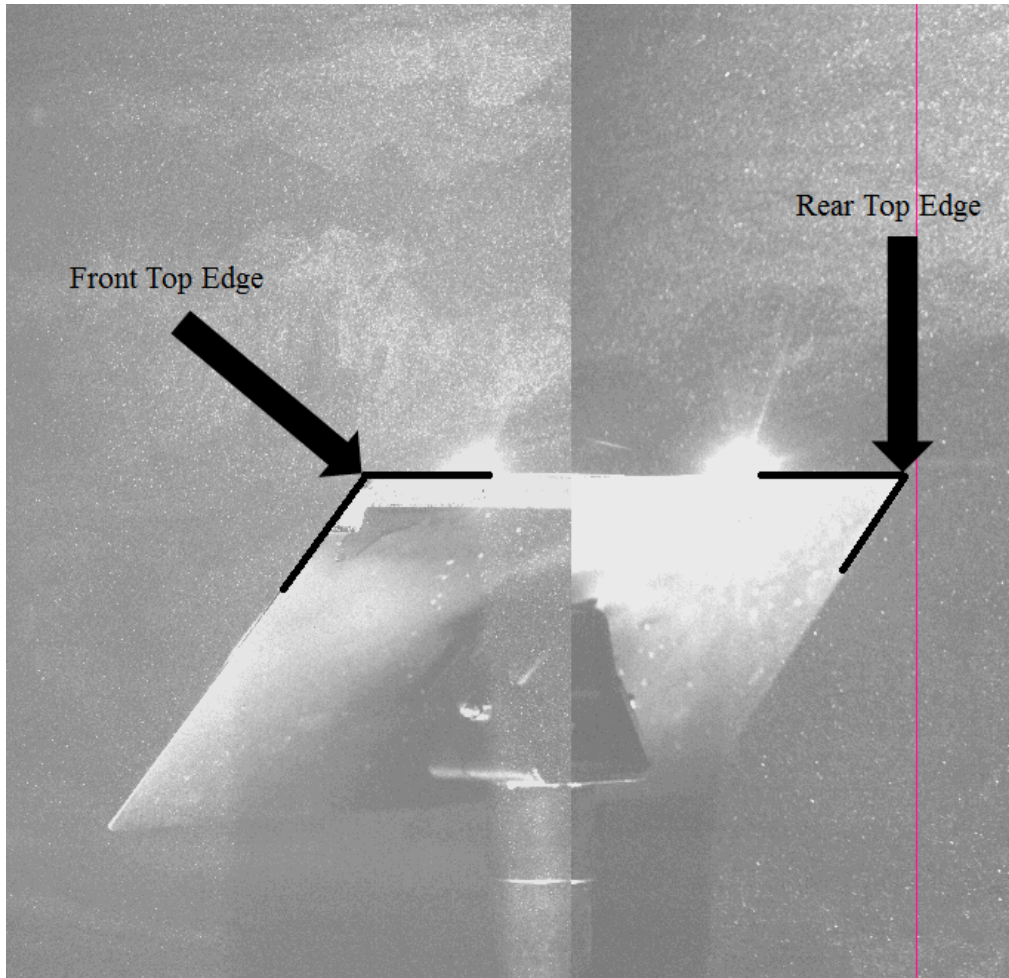


Figure G-2: Reference points for tilted heliostat in mid and offset plane

Table G-1: Location of lines relative to heliostat

Figure Set	Line Reference	Reference Point	Location
6-8 and 6-9	01	Heliostat face	157 mm upstream
	02	Heliostat face	82 mm downstream
	03	Heliostat face	108 mm downstream
	04	Heliostat face	157 mm downstream
	05	Heliostat face	231.4 mm downstream
6-10 and 6-11	01	Rear top edge	5 mm downstream
	02	Rear top edge	44 mm downstream
	03	Rear top edge	104.5 mm downstream
	04	Rear top edge	240 mm downstream
	05	Rear top edge	331.5 mm downstream
6-12 and 6-13	01	Front top edge	100 mm downstream
	02	Rear top edge	43 mm upstream
	03	Top front edge	250 mm downstream
	04	Rear top edge	140 mm downstream
	05	Rear top edge	277 mm downstream
	06	Rear top edge	320 mm downstream